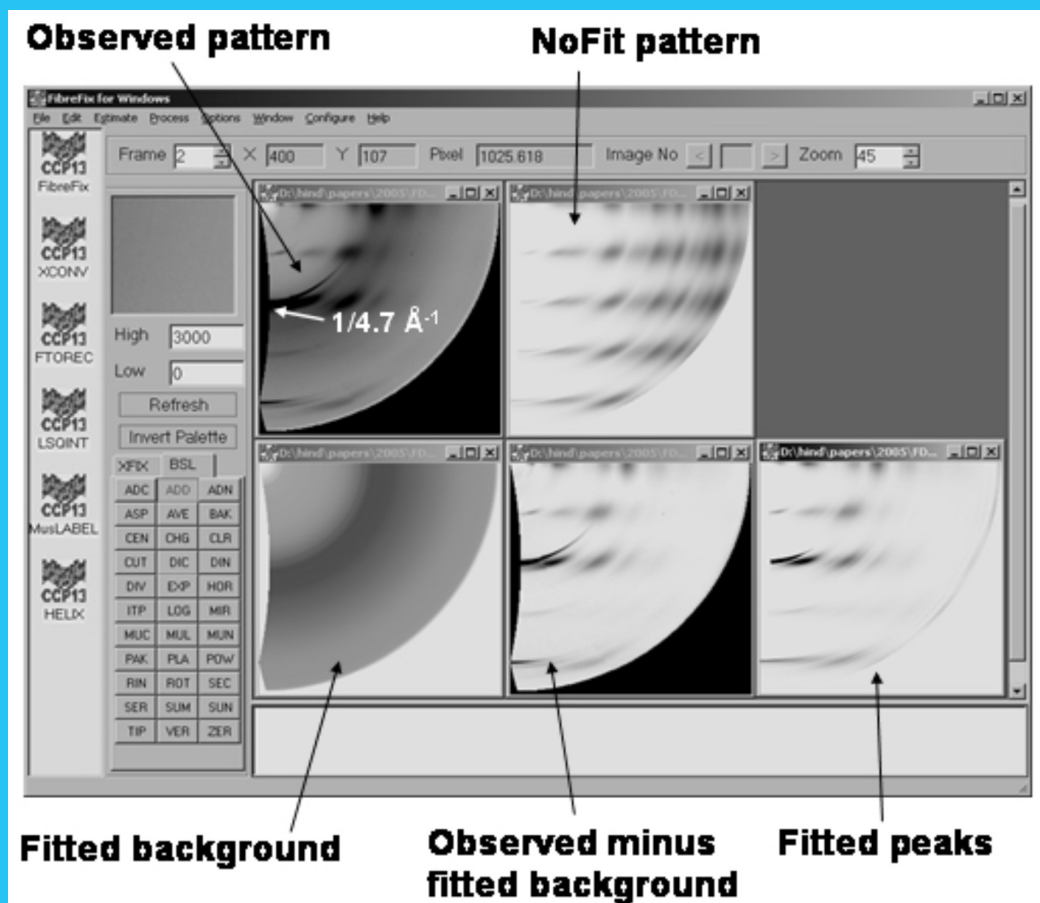


FIBRE DIFFRACTION REVIEW

*Reports on Progress in Fibre Diffraction
and Solution Scattering*

A CCP13 / NCD Publication



The new FibreFix Program applied to Amyloid



CCP13

**14th Annual Fibre Diffraction and Non-Crystalline Diffraction
Workshop
22-24 June 2005
CARDIFF UNIVERSITY**

Clair Baldock (Manchester)

John Squire (Imperial)

Craig Boote (Cardiff)

Rudolph Winter (Aberystwyth)

Steve Eichhorn (Manchester)

Oskar Paris (MPI Golm)

Julian Oberdisse (LCVN)

Tom Irving (APS)

Sam Shaw (Oxford)

Gerald Stubbs(Vanderbilt)

Nick Terrill (Diamond)

Tony Ryan (Sheffield)

Naoto Yagi (Spring 8)

Manfred Roessle (HASYLAB)

Manfred Burghammer (ESRF)

John Seddon (Imperial)

David Cairns (Stirling)

Tim Wess (Cardiff)



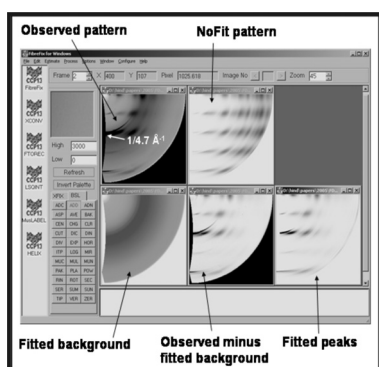
Sponsored by JJ X-Ray and Bruker-AXS

JJ X-Ray
Danish Science Design



For further information and registration, see the web pages at <http://www.ccp13.ac.uk/>

CONTENTS.....	1
CHAIRMAN'S MESSAGE.....	2
MEETING REPORTS	
The canSAS-IV Meeting at DIAMOND. Stephen King.....	3
The 2004 CCP13/NCD Workshop - Grenoble. Trevor Forsyth.....	7
First FiberNet Workshop: Argonne - 2004. Gerald Stubbs and Thomas C. Irving.....	9
TECHNICAL REPORTS	
The New CCP13 Package FibreFix. Ganeshalingam Rajkumar, Hind AL-Khayat, Felicity Eakins & John Squire.....	11
New Functionality in Corfunc. Stephen King and Damian Flannery.....	19
PRELIMINARY REPORT	
Intensity Analysis of Myosin-based X-ray Meridional Reflections from Live Skeletal Muscles in Relaxed and Contracting States. Kanji Oshima, Yasunori Takezawa, Yasunobu Sugimoto, Thomas C. Irving & Katsuzo Wakabayashi.....	23
ORIGINAL ARTICLES	
The Interpretation of Simultaneous Small- and Wide-angle X-ray Scattering Data Collected During Quiescent Crystallisation. Simon Hanna.....	31
Flexible Filamentous Viruses from Fiber Diffraction. Gerald Stubbs, Lauren Parker, Justin Junn and Amy Kendall.....	38
EXPANDED ABSTRACTS FROM PRIZE-WINNING POSTERS	
Amyloid Fibrils Formed by Peptide Sequences from a Natural - Structured Fibrous Protein, the Fibre of Adenovirus. K. Papanikolopoulou, V. Forge, G. Schoehn, C. Riekel, J.F. Hernandez, R.W.H. Ruigrok, V.T. Forsyth and A. Mitraki.....	43
In-Situ WAXS Studies of Structural Changes in Wood Foils and in Individual Wood Cells During Microtensile Tests. J. Keckes, I. Burgert, M. Müller, K. Kölln, M. Hamilton, M. Burghammer, S.V. Roth, S.E. Stanzl-Tschegg and P.Fratzl.....	48
13th ANNUAL WORKSHOP ABSTRACTS.....	52
INSTRUCTIONS TO AUTHORS.....	76



Cover Image: The window of the new CCP13 FibreFix program. The diffraction pattern is from an amyloid sample (courtesy of Dr. Louise Serpell) and is shown after completing initial image processing under XFIX, transformation to reciprocal space using FTOREC, and intensity peak fitting under LSQINT, all within the FibreFix environment. For details of the FibreFix package see article by Rajkumar et al. in this Volume, pp 11 - 18.

Editorial Office:

Editor: Prof John Squire, Biological Structure and Function Section, Division of Biomedical Sciences, Imperial College London, SW7 2AZ.

Production: Ms Toun Baruwa, Biological Structure and Function Section, Division of Biomedical Sciences, Imperial College London, SW7 2AZ.

CHAIRMAN'S MESSAGE

Outgoing Chairman

John Squire

Dear Friends,

The year 2004 - 2005 was a period of ups and downs for CCP13. On the up side was another superb production of *Fibre Diffraction Review* (volume 12), the largest ever Annual CCP13-NCD Workshop, this time in Grenoble and superbly organised locally by Trevor Forsyth (see pages AA-BB), and the first Workshop of the US Fiber Diffraction Network (FiberNet), closely associated with CCP13, which was a very enjoyable event at the APS, Chicago (see pages 9 - 10). On the down side were disappointed attempts to obtain further Research Council funding from BBSRC and EPSRC. For the first time in 14 years, our application was not renewed. This means that we have now had to lose the services of both Jane Crawshaw and Andrew He, and our thanks and good wishes for successful future careers go with them. Ganeshalingham Rajkumar is continuing with me at Imperial College and has been heavily involved not only in manning the CCP13 website single-handed, but also in developing the FibreFix software package which is described in detail on pages 11-18 of the present volume. We hope that this new package will make all the old and trusted CCP13 programs much more easy to use and we have incorporated many new features into it. Your feedback on this is essential to make the package as useful as it can be for the widest possible spectrum of users.

For the time being, *Fibre Diffraction Review* is continuing, but further production of this Journal will depend on support from the NCD community, from Research Councils and possibly from advertisers. At the very least I hope it will continue in electronic format on the CCP13 website, but I have always been very proud of our beautiful, full colour, hardcopies which have always been much admired over the years and have been wonderful publicity for CCP13. I hope that we will be able to find a way for the production of the paper version to continue.

Earlier this year, in view of the hiatus in our funding, and the need to bring in fresh blood to lead CCP13, I decided to step down as CCP13 Chairman and, after sounding out the views of the CCP13 Committee, Professor Tim Wess from Cardiff University was invited to take over as the new Chairman, a role which I am delighted to say he agreed to accept. I wish him every success in steering CCP13 in new and fruitful directions and I hope you will all give him your full support so that CCP13 remains strong and vigorous.

On a personal note, I could not have acted as Chairman over recent years without the very strong, vigorous and

erudite support of the then Deputy Chairman, Trevor Forsyth, and I acknowledge here my (and our) indebtedness to him for all his hard work and dedication.

John Squire

CHAIRMAN'S MESSAGE

Incoming Chairman

Tim Wess

Dear Friends,

As the new Chairman of CCP13 I would like to take this opportunity to thank John and Trevor for their skilled guidance over the last 14 years. I believe that John, Trevor and I are among a very small group of CCP13 members who have had the pleasure of attending every Annual Workshop. During this time I have had the opportunity to watch John steer CCP13 from its beginnings at the Daresbury laboratory to the internationally recognised organisation it now forms. The founding of FiberNet, the American counterpart of CCP13, shows that there is a pressing need for co-operation between like-minded researchers world wide.

Since the creation of CCP13 14 years ago, we have seen major changes in the way that and the rate at which scattering data are collected in non-crystalline systems at both X-ray and neutron sources. As an organisation we have to embrace this new progress and develop a forum for software development that will remain in the vanguard of data analysis and modelling for many years to come.

The way forward requires funding for a sustainable future, where we hope that more Research Councils will recognise the valuable input of CCP13 software development and the high quality science it engenders. Personally, I am committed to spreading the news of CCP13 developments as widely as possible. I envisage the strengthening of relationships with other CCPs where synergy can be built, the closer interaction with central facilities, and the development of more Workshops, site visits and consultancies that will educate the new and established user community and will provide user feedback to the CCP13 software creators.

Tim Wess

Meeting Reports

The canSAS-IV Meeting at Diamond / ISIS

The Fourth in the occasional series of *canSAS* meetings took place at the Rutherford Appleton Laboratory (RAL), UK, over May 12-14, 2004.

canSAS - Collective Action for Nomadic Small-Ange Scatterers - was conceived at the ILL/ESRF campus in 1998 as a means to try to alleviate some of the problems that beset visiting users of small-angle scattering (SAS) instruments at neutron and X-ray facilities due to differences in the data formats. It seemed that every facility, and in some cases almost every instrument, had its own format for essentially the same information! In addition this had given rise to a plethora of data analysis programs, often performing the same calculations. The inaugural *canSAS* meeting wanted to see if there might be ways to reduce the entropy of the situation, provide a "point of contact" where information might be deposited and shared, and foster interaction between the neutron and X-ray halves of the SAS Community around the world; see *Neutron News*, **9(3)**, 6, (1998).

In this role *canSAS* has actually been reasonably successful (if a little anonymous), although progress on the thorny issue of data formats has perhaps not been as swift as many would like.

One of the other factors affecting the SAS Community in recent years has been the rapid growth in what might be termed "added-value" experiments; for example, the coupling of DSC with SAXS/WAXS, rheometric measurements with SANS, and the in-situ use of stop-flow apparatus, stress rigs and extruders, to name but a few. Such experiments not only generate large multi-parameter datasets, but are increasingly also being done in real-time (even with today's relatively low flux neutron sources). All this naturally has serious implications for data acquisition and data handling, particularly on tomorrow's sources.

It was against this backdrop that 60 delegates, 33 of whom were from overseas (including Australia, Japan and the US), gathered for what turned out to be a very successful and lively meeting. Indeed, the organisers had to close registration early because the room capacity had been reached!

Crammed into a very busy two-day programme were 25 oral presentations, almost as many poster presentations, half a dozen software demonstrations, a tour of ISIS, and the opportunity to see the new Diamond Light Source under construction!

canSAS-IV formally commenced with an address by Andrew Taylor, Deputy Chief Executive of CCLRC and Director of ISIS, who spoke about the future opportunities for soft matter research that would present themselves on completion of the Diamond Synchrotron (2006) and the ISIS Second Target Station (2007). There were also expected to be significant enhancements of the campus infrastructure to go alongside these major investments in scientific facilities.

Meeting contributions then largely addressed three areas: new technical developments, software developments, and "cutting-edge" science embracing one or other (or perhaps both!) of the above.

Elliot Gilbert (Bragg Institute, ANSTO) gave a review of the recent meeting at Lucas Heights on "Data Visualisation, Reduction and Analysis at Australia's Replacement Research Reactor". This had emphasised the key role that well-written, intuitive, tested, software plays in turning experimental data into meaningful scientific results, and encouraged the establishment of a central repository of routines conforming to an established framework.

Jun-ichi Suzuki (JAERI, Tokai) then explained how polarised neutron beams could be focussed by magnetic "lenses". The significance of this approach for SANS is that there is only a 50% flux loss (assuming 100% polarisation) regardless of the Q-vector being targeted, whereas in a conventional (pinhole) SANS instrument the loss of flux at small Q is quite severe because of the need for highly-collimated beams and long sample-detector distances. The magnetic lens approach is also applicable to time-of-flight (TOF) SANS. A drawback, of course, is the cost of the magnets!

Michael Drakopoulos (Diamond, Didcot) followed a similar theme and discussed the use of compound refractive lenses with X-rays. This talk illustrated how such optical

elements have opened up fields such as SAXS Microscopy and X-ray Imaging.

Wim Bras (DUBBLE, Grenoble) highlighted how software performing even relatively unsophisticated data treatments has largely failed to keep pace with the growth in data volume due to time-resolved SAXS. Quite simply, only a few percent of the time-resolved data collected at synchrotrons around the world is ever "analysed". Whilst considerable resources are directed into beam line and detector developments, far fewer resources seem to be directed at making more efficient use of the data that can be collected right now. Though the problem is more acute in SAXS, it also affects SANS.

Thomas Weiss (ESRF, Grenoble) demonstrated how putting a Daresbury SRS RAPID detector on the high-brilliance ID2 beam line at the ESRF, together with stop-flow apparatus, had enabled them to elucidate the kinetics of the micelle-to-vesicle transition in an anionic/zwitterionic surfactant mixture. Data was recorded with millisecond time resolution.

Charles Dewhurst (ILL, Grenoble) gave an overview of his MatLab script GUI GRAS_{ans}P for SANS multidetector data, illustrating its graphical capabilities on some early data from the recently installed D22 linear multidetector array of 8 mm diameter, 1 m long gas tubes. Count rates of up to 3 MHz have already been realised. It is necessary to both geometrically calibrate and correct for non-linearity at the ends of the tubes in software. This has led to much discussion about what constitutes the "raw" data, and how it should be stored.

Stepping in to fill a vacant slot at very short notice, *Rob Dalgliesh (ISIS, Didcot)* talked about the opportunities presented by the emerging field of Spin-Echo SANS (SESANS). In a presentation that Rob duly acknowledged as primarily the work of others, he explained how SESANS was an alternative means for accessing larger length scales (*cf.* the double-crystal/Bonse-Hart or magnetic lens approaches) but in *real space*, not Q space. A purpose-built instrument already exists at IRI in The Netherlands and ISIS is looking into the feasibility of adapting the technique to a pulsed source.

Theyencheri Narayanan (ESRF, Grenoble) gave an elegant overview of Ultra-SAXS (USAXS), including how the partially coherent nature of synchrotron X-radiation may be exploited in the emerging technique of Dynamic-USAXS (*cf.* Photon Correlation Spectroscopy) for the study of colloidal systems.

Jan Šaroun (Nuclear Physics Institute, Prague) then presented details of his SASProFit software for the combined modelling of USANS and SANS data, illustrating its capabilities with a case study of cavity formation in a superplastic alloy.

Though not a "scatterer" in any sense of the word, *Elena Pourmal (NCSA, Urbana-Champaign)* has been a welcome visitor to more than one canSAS meeting in her capacity as a lead developer of HDF5, the Hierarchical Data Format, the "tool" that underlies the NeXus file format. In her talk Elena charted the challenges in data management that gave rise to HDF, an overview of its current usage (the NASA Earth Observation System archive alone currently stands at 4M Gb, dwarfing anything the neutron and X-ray communities are likely to achieve!), and looked to the future (e.g. client-server adaptations for GRID applications, the rise of bioinformatics and, worryingly, an uncertain funding model).

Ron Ghosh (ILL, Grenoble) is one of the canSAS "founding fathers". He was also the ideal person to take the audience back through time to show how some of the present problems in respect of data formats and the difficulties of sharing and visualising data across facilities have evolved. There were a number of insightful observations: the platform dependence of many current GUIs, libraries and executables; that, whilst platform independent, Python and Java have rather poor math libraries; that many of the commercial packages have different scripting languages; and that, increasingly, *Users do not, can not, or will not, program*. Ron also presented his vision for the future, a "data query language" for data files (*cf.* SQL for databases).

Rainer Wilcke (ESRF, Grenoble) returned to the problems facing time-resolved SAXS, reminding the audience, in particular, that the true data quality (statistics) could only be properly estimated after initial corrections. At the ESRF a program has been developed to automatically apply these corrections online within seconds of data acquisition, even for time-resolved data.

Rex Hjelm (LANSCE, Los Alamos) talked about some of the pitfalls and benefits they had experienced with new data acquisition, instrument control and data management systems on the LQD SANS instrument following its recent upgrade. This instrument is one of the very few to have actually implemented a NeXus raw file format (albeit a non-standard implementation) and it was encouraging to hear that it seems to have found favour.

Bill Pulford (Diamond, Didcot), the newly installed Head of the Data Acquisition (DAQ) Group, outlined the basic ideas that he was promoting for Diamond. Whilst control of the accelerator and the beam lines will be provided by EPICS (as at the APS), DAQ and experiment control will use Java with Jython as a scripting language. It is expected that raw data will be stored in the NeXus format, and there was a strong commitment towards the use of electronic logs and "beam line configuration databases". Bill also envisaged Terabyte disk arrays in each experimental station and having a scientific programmer "associated" with each scientific technique. The X-ray community sees this level of resource allocation as essential in the

future.

Kevin Knowles (ISIS, Didcot), Head of the ISIS Computing Group, gave the view "from the other side of the road" (literally!). ISIS has been steadily migrating from VMS/Q-Bus based DAQ systems, to OpenVMS/SCSI based systems, and latterly to PC/VME based systems, with scripting through the ISIS OpenGenie package. LabView® is gradually replacing CAMAC for control of beam line instrumentation and sample environment.

Dmitri Svergun (EMBL, Hamburg) presented details of the latest enhancements to the ATSAS program suite for the analysis and modelling of solution SAS data: a program (PRIMUS) for initial data treatment, and for the biological community a database (DARA) of SAS curves computed from the PDB.

Tracy Nixon (Pennsylvania State University) introduced himself as a cell biologist who is interested in how AAA+ ATPases couple ATP hydrolysis with mechanical work and, thus, conformational change. A speculative enquiry led to some casual beam time at the APS BioCAT beam line and an introduction to Dmitri Svergun's programs, and now he is a convert to SAXS/WAXS! This was an excellent and refreshing tale from someone who was now sold on the benefits of SAS.

Adrian Rennie (NFL, Studsvik) is another *canSAS* stalwart and, as both an ex-instrument scientist and ex-academic, is someone well-qualified to judge how both sides view SANS experiments. What makes an experiment difficult from the instrument responsible's perspective (often something about the sample) is usually completely different to the Users perspective (the problem is with the instrument)! To illustrate this Adrian showed two examples from his own work on optoelectronic materials: a cadmium chalcide borosilicate glass, and a spin-coated film of organic photoluminescent polymer 100 nm thick (corresponding to an illuminated sample mass of just 0.02 mg) - neither are instinctive samples for a SANS experiment.

Aymeric Robert (ESRF, Grenoble) talked about the TROIKA beam line at the ESRF and X-ray Photon Correlation Spectroscopy (XPCS). XPCS probes the same time domain as optical PCS but does so at higher Q values. Multiple scattering is also much less of a problem in XPCS and can, of course, be used to study "cloudy" or opaque samples. Unfortunately experience suggests that there is insufficient electron density contrast in typical protein solutions to make the technique attractive to the Life Sciences, whilst radiation damage to the sample is also something of a problem.

Xiangbing Zeng (University of Sheffield) described a real-time SANS study of isothermal crystallisation in a selectively-deuterated model alkane system, performed on

LOQ at ISIS. Using a Temperature-Jump apparatus (~1 s jump) that also triggered the data acquisition, good quality data was recorded in frames as short as 10 s on as little as 100 mg of sample. An exciting development for SANS.

John Ramsay (CNRS, University of Montpellier II) described work on organically-directed colloidal zeolite particles for use in separation membranes and sensors. The particles form under hydrothermal conditions and the structure evolution was followed *in-situ* by WAXS, SAXS and USAXS on ID2 at the ESRF. Parallel SANS studies on another zeolite system exploited selective deuteration and contrast variation to gain an insight into the role of the organic cation, nicely complementing the X-ray work.

Kerstin Kleese-van-Dam (CCLRC e-Science Centre, Daresbury) gave an overview of what e-Science was ("a holistic approach to integration from the experiment to the results"), how it was likely to affect large-facilities and their Users in the future (remote-control or remote-supervision of experiments, better number-crunching, and better data archiving to name but a few), and a walk through some of the current projects: (The) GRID (essentially the utilisation of spare computing resources around the world), AccessGRID (like video-conferencing but over the web), DataPortal (a "one-stop shop" to access data across many locations), Storage Resource Broker (a truly global distributed file system), and the Digital Curation Centre. However, the question of who "owns" the data that is collected appears to be a matter of some debate.

William Helsby (CCLRC, Daresbury) from the CCLRC Instrumentation Department talked about the development, construction and operating principles of multi-wire gas detectors for both neutron and X-ray use. Highly-parallel readout systems provide much-demanded improvements in count rate performance. The new Daresbury High-Overall Throughput WAXS (HOTWAXS) detector, for example, has a global count rate of 500 MHz. Looking to the future there are several potential benefits (e.g. cost, counting accuracy & spatial resolution) from the developing field of micro-pattern detectors.

Richard Heenan (ISIS, Didcot) described work he had been involved with on D22 using the ILL Stop-Flow apparatus to follow a vesicle-to-micelle transition in a mixed surfactant system at, typically, just 5 mM concentration. In contrast to Thomas Weiss' millisecond time resolution achieved with X-rays (see above), the SANS data was recorded in 2 second frames, repeated 4 or more times to aggregate the statistics. This was a firm reminder, if one were needed, of just how great the difference in count rates between synchrotron SAXS and SANS still are. But from the SANS perspective, given the low scattering cross-sections, this work represents a great step forward in what can be achieved.

Rounding off the oral presentations, *John Squire* (*Imperial College, London*), the current Chairman of CCP13, talked about the history of the project, its current status, and its possible future directions. Established to provide software for the analysis of (largely X-ray) fibre diffraction data, CCP13 has gradually broadened its remit to embrace polymers, oriented colloidal systems and the neutron community. Discussions are now underway to provide good model-fitting software for solution scattering.

There were two Discussion Sessions at *canSAS-IV*; one specifically on data file formats, the other on matters of more general interest to the SAS Community.

Freddie Akeroyd (*ISIS*) and *Ken Littrell* (*IPNS*) initiated the data file format discussion with two short presentations. Freddie - a member of the NeXus International Advisory Committee (NIAC) - gave an overview of the current status of NeXus. After a long (some might say overly long) gestation the formation of the NIAC in early 2003 seems to have given the project much-needed impetus. Agreement on NeXus "class" names, and on many of the item names within, should be completed by the end of June 2004 at which point the Instrument Definition "editors" (e.g. monochromatic neutron/X ray SAS and TOF neutron SAS) can start work. There was consensus amongst the audience for facilities to convert to NeXus as a raw data format.

Ken focussed more on issues to do with treated data, highlighting how almost every SAS instrument has an ASCII output format for its 1-dimensional (i.e. regrouped, azimuthally-averaged) data that consists of a header followed by some columns of numbers; yet every single one is different! It was proposed that *canSAS*

should solicit a convergence to a common format. A further issue that was identified was the general absence of Q-error bounds in these treated data files.

The general discussion session focussed on building Community participation in *canSAS* and on the posture between *canSAS* and the IUCr Commission on Small-Angle Scattering (CSAS). Some in the audience thought that *canSAS* was doing what CSAS ought to be doing or, at least, doing more visibly.

Finally, it was proposed that it would be appropriate for *canSAS-V* to take place alongside the IUCr-sponsored SAS conference in Japan in 2006.

The organisers would like to express their gratitude to Diamond and ISIS (CCLRC), the ILL, and the DUBBLE (NOW/FWO) beam line at the ESRF for financial support.

The *canSAS* website is hosted by the ILL at the URL: <http://www.ill.fr/lss/canSAS/>. Additional contributions from the Community are encouraged. The abstracts for *canSAS-IV* are available online, as are a number of presentations and software downloads.

STEVE KING
ISIS Neutron Source
NICK TERRILL
Diamond Light Source
Rutherford Appleton Laboratory, Didcot, UK
(*canSAS-IV* Local Organisers)



Delegates at *canSAS-IV*

CCP13: The 13th UK Annual Fibre Diffraction and Non-Crystalline Diffraction Conference

ILL/ESRF 2-5th June 2004

The 13th CCP13 conference - the UK Annual Fibre Diffraction and Non-Crystalline Diffraction meeting was held at the ILL/ESRF on 2-5th June 2004. One of the central themes was the combined use of X-ray and neutron scattering studies. The meeting turned out to be extremely popular - registration had to close when the number of delegates reached 105. There was wide representation from the UK fibre diffraction and solution scattering community, as well as from a large number of laboratories throughout Europe, and of course from the laboratories on the Grenoble site. Delegates were welcomed by the ILL and ESRF Directors, Colin Carlile and Bill Stirling, who described the range of facilities relevant to this community that are available on the site. They also emphasised that these facilities receive major funding from the UK and that the CCP13 user community should see them as available to them in the same way that other UK-funded facilities such as SRS and ISIS. Both Directors emphasised the importance of the new PSB (Partnership for Structural Biology) that is being built as part of a collaboration between ILL, ESRF, EMBL and IBS. The PSB building, which will also incorporate the new Institute of Molecular Virology, will be complete in about 12 months time, and will offer unparalleled facilities for interdisciplinary research in biology.

The conference presentations were excellent. Svergun (EMBL), Perkins (UCL London), Lawrence (KCL London), Hartlein (ILL), Timmins (ILL) and May (ILL) described the application of X-ray and neutron solution scattering as well as the potential available through deuteration methods. Callow (ILL/Keele) described his EPSRC-funded work in collaboration with Kneale (Portsmouth) on the application of these methods to the study of type I restriction-modification. Zaccai (IBS, Grenoble) gave an exciting presentation on a small angle scattering analysis of incoherent elastic neutron scattering to study dynamics. In the area of partially ordered systems there were also some excellent presentations on muscle from Irving (Illinois), Squire (Imperial), Irving (KCL), Ferenczi (Imperial), Wakabayashi (Japan), and Yagi (Japan). Stubbs from Vanderbilt described fibre diffraction work on flexible filamentous viruses and Kirschner (Boston) described recent advances in the study of amyloid fibrils using fibre diffraction. Riekel (ESRF) spoke about SAXS/WAXS and neutron studies of spider silk, and Mueller (Kiel) gave a talk on combined x-ray and neutron work on native cellulose. While many of

the presentations were biologically inclined, there were also presentations on carbon nanotubes from Crawshaw

(Cambridge), one on novel experiments at the ESRF for the study of smectic liquid crystals in an electric field (Bras, ESRF), and also two from Sheffield - one by Zeng about a SANS study of transient phases in polymer crystallization and another by Heeley about scattering studies of micropolymer processing. Nick Terrill described developments foreseen at Diamond and led a discussion of the priorities for future development at Diamond.

On the analytical/computational side there were presentations from Hammersley (ESRF) about likely future directions for software, from Ma (Baylor) about fibre diffraction refinement, and from Millane (Canterbury, New Zealand) who described methods for the analysis of myosin superlattice structure in striated muscles.

The quality of the posters was truly outstanding - congratulations to Katerina Papanikolopoulou (IBS) for her poster entitled *Amyloid fibril formation from sequences of a natural beta-structured fibrous protein: the adenovirus fibre* and to Jozef Keckes (Leoben) for his entitled *In situ WAXS studies of structural changes in wood foils and individual wood cells during microtensile tests*. Each won CCP13 poster prizes (£250) that were presented at the conference dinner at the Chateau de Sassenage.

Twenty six people stayed for the excursion to the spectacular *Grottes de Choranche* and (for the wine inclined) Tain L'Hermitage.

Trevor Forsyth
Institute Laue Langevin
Grenoble, France



Trevor Forsyth (right), the local organiser of the Grenoble Workshop, clarifying a point with Tom Irving at the pre-Dinner reception at the Chateau de Sassenage.



CCP13 / NCD Workshop (2004) - Grenoble

First FiberNet Workshop: Argonne, 2004

FiberNet, the new American fiber diffraction organization, held its first workshop from Thursday 21 October to Saturday 23 October 2004 at Argonne National Laboratory (ANL), about 25 miles south-west of Chicago. ANL was a particularly appropriate site for the workshop, since it is the location of the facilities of the Biophysics Collaborative Access Team (*BioCAT*) at the Advanced Photon Source synchrotron. *BioCAT* is a unique resource for biological fiber diffraction in America, and functions as a focal point for the activities of *FiberNet*.

FiberNet is a network of American fiber diffraction groups, established in 2003 with the support of the National Science Foundation. The goal of the network is to develop and disseminate fiber diffraction methods through a program of software development and a series of retreats and workshops. *FiberNet* is particularly interested in biological fiber diffraction, but fiber diffraction methods for biological and non-biological applications are generally similar, so the organization encompasses all approaches and applications. The establishment of

FiberNet was inspired by the example of CCP13, and the two organizations work closely together.

The workshop was attended by 28 participants, including four from Europe and one from Canada. *CCP13* was represented by John Squire and Trevor Forsyth. The program included a number of excellent research presentations, mostly focused on biological fiber diffraction, and included X-ray and neutron scattering, taking both experimental and theoretical approaches.

The relatively small size of the meeting lent itself particularly to a number of open forums, which were among the high points of the workshop. John Squire led a highly informative discussion of the software available from *CCP13*; the effectiveness of this discussion might be measured by the number of laptops to be seen busily running the *CCP13* programs during the breaks after that session! Gerald Stubbs and Wen Bian led a discussion of proposed *FiberNet* software, with particular interest shown in the molecular dynamics refinement program F-XPLOR. A panel consisting of R. Chandrasekaran from





Purdue, Amy Kendall from Vanderbilt, and Kenn Gardner from Dupont led us through a variety of specimen preparation methods, catalyzing exchanges of ideas that are still continuing.

Friday's program ended with a tour of the *BioCAT* beam line at the Advanced Photon Source, the Argonne third generation synchrotron. The tour included the orientation that is required for new users, in preparation for another very successful feature of the workshop, an opportunity on Saturday for participants to collect data from their own specimens. This was attended by 11 participants, who all took home data from their samples. Fiber diffraction workshops where groups of people share time to collect wide angle fiber data over a two to three day period are anticipated to become a regular feature of the BioCAT scientific program.

Although the scientific activity was intense, there were lighter moments. A poster session on Thursday provided opportunities for lively exchanges of ideas, and with most participants staying at the Argonne Guest House, dinners on Thursday and Friday were well attended. It has been some years since American fiber diffractionists had such an opportunity to get to know each other, so this meeting was a time to develop new collaborations and collegial relationships, as well as a showcase for the facilities of *BioCAT*.

The workshop is planned to be the first of a series. The network supports annual workshops; in odd-numbered years, these take the form of a sponsored session on fibre diffraction at the American Crystallographic Association annual meeting (neutron fiber diffraction at Disney World in 2005!). In even-numbered years, however, the workshop will be a free-standing meeting such as this one, rather like the annual CCP13 meeting. The meeting planned for 2006 will be a continuation of the informal fiber diffraction meetings held in American State Parks: in 1989 at Fall Creek Falls, Tennessee, in 1993 at McCormick's Creek, Indiana, and in 1997 at Jenny Wiley State Park, Kentucky. Watch for announcements!

FiberNet is supported by the National Science Foundation's Division of Molecular and Cellular Bioscience, through grant MCB-0234001. *Fibernet's* web site is at www.fiberdiffraction.org.

Gerald Stubbs
Vanderbilt University
and
Tom Irving, BioCAT
and Illinois Institute of Technology
November 2004

FibreFix - A New Integrated CCP13 Software Package

by

Ganeshalingam Rajkumar, Hind AL-Khayat, Felicity Eakins,

Andrew He, Carlo Knupp* and John Squire

Biological Structure and Function Section, Biomedical Sciences
Division, Imperial College London, London SW7 2AZ, UK
and

*Biophysics Group, Dept of Optometry and Vision Sciences,
Redwood Building, Cardiff University, Cardiff CF10 3NB

Abstract

The tried and tested CCP13 programs, XCONV, XFIX, FTOREC and LSQINT have been incorporated into a single user friendly package known as FibreFix. This has the advantage that parameters determined in one part of the data processing are carried forward automatically to the next step in the process. The new package also incorporates many new analysis features, it incorporates BSL functionality and also provides direct access to the helical diffraction simulation programs HELIX and MusLABEL. The new package is accompanied by a series of tutorials on different kinds of fibre specimen to illustrate the kinds of values that different fitting parameters might have. All programs can be accessed through the CCP13 website <http://www.ccp13.ac.uk>.

Introduction

Almost 14 years ago, when CCP13 was created, the first priority was to establish basic programs with which to analyse fibre diffraction and other data arising with ever-increasing speed and resolution from synchrotron X-ray sources and from neutron beam-lines. For this purpose we were fortunate to be able to recruit Dr. Richard Denny, a very able mathematician with experience in X-ray crystallography, who wrote the programs that are central to CCP13 analysis. These include XCONV, XFIX, FTOREC and LSQINT which will be familiar to many CCP13 users and which were developed by Denny (1993; 1996) based on the fibre diffraction formulations of Fraser *et al.* (1976; and see Fraser, 1994). These programs in turn built on the foundation of the programs OTOKO and BSL which had been implemented at the Daresbury Laboratory as a means of preliminary data processing (J. Bordas, G. Mant) and which specified the data format that is still commonly used (BSL format). The general strategy behind the CCP13 approach was outlined in Squire *et al.* (2003).

However, despite the tremendous advances made by Richard Denny (Denny, 1993; 1996) and later by his successor in CCP13 Mark Shotton (Shotton and Denny, 1999), there remained a considerable energy barrier for newcomers to fibre diffraction trying to apply the CCP13 software for the first time to their own particular problem. For this reason the last few years have seen the development by CCP13 staff of more integrated and user-friendly data analysis packages. The first approach towards implementation of this was a package called ICE

(Integrated CCP13 Environment; He *et al.*, 2004), but this has now been refined, developed and consolidated into the current form of the program known simply as FibreFix.

The FibreFix Program

In the FibreFix program, currently implemented in Windows but intended in the long run to become a JAVA program for use on any platform, the user clicks on the FibreFix desktop icon to open the single package, FibreFix. This contains an outer frame carrying instructions and drop-down menus with various operations, together with a large window into which the data image can be dropped (opened; Figure 1). Within this environment all the previous CCP13 operations involved in fibre diffraction data analysis can be carried out. In previous procedures, the program XCONV was used to convert the raw data from detector format to the common BSL format. The new FibreFix program automatically includes XCONV functionality and will display images immediately if the file extension is recognised, or may come up with a simple query window if unknowns such as the image dimensions need to be input. The new program also includes much of the functionality of BSL, but now GUI-driven, so that users with particular processing preferences in BSL can continue to use their chosen routines. Some new BSL routines have also been added (see below). Note that if there are image (detector) formats which are not yet incorporated into the XCONV or FibreFix programs, please provide the details and these will be incorporated as soon as possible; the plan is to be able to deal with all new detector formats as they come on

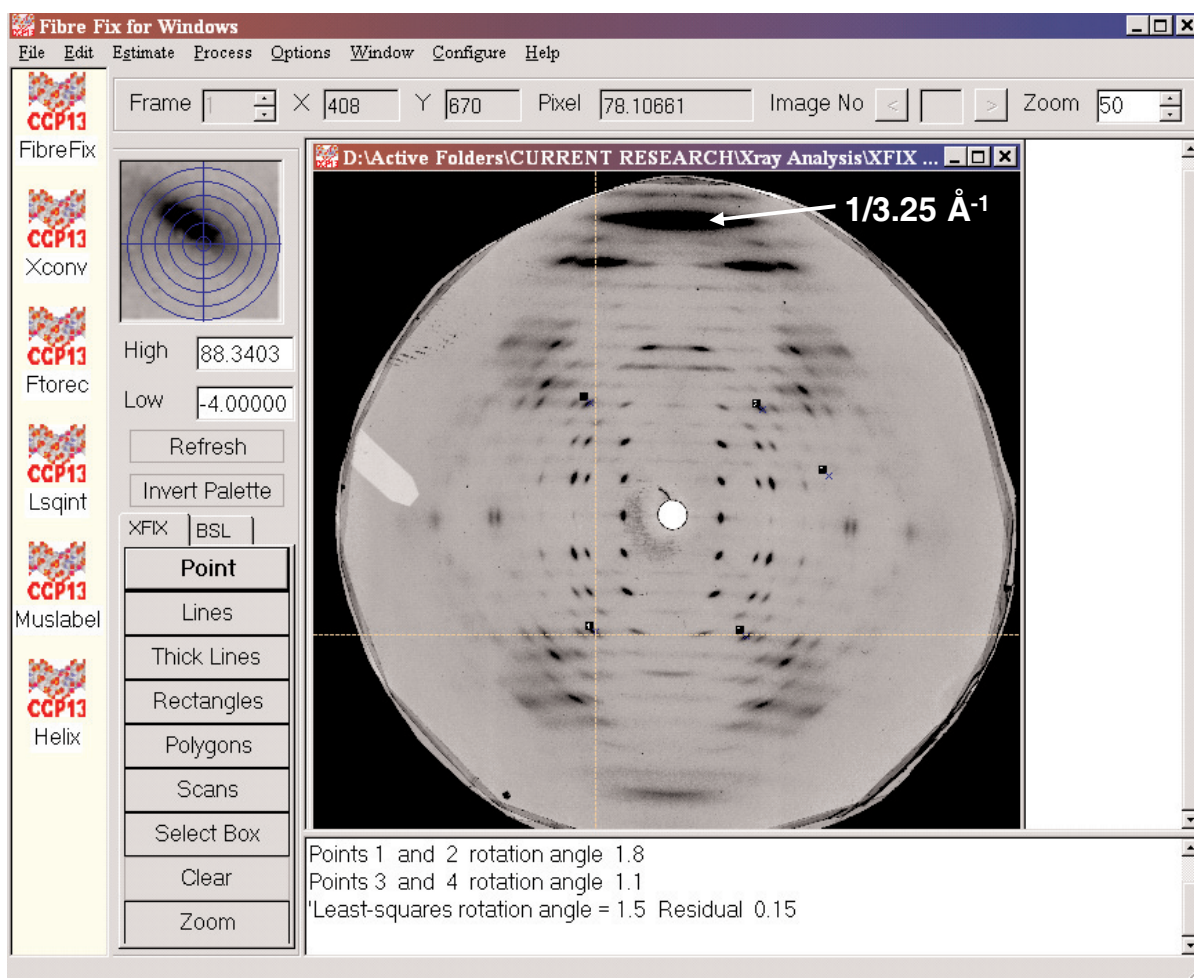


Figure 1: The FibreFix window with a diffraction pattern from E-DNA opened in it.

stream.

Once the image file has been displayed in the **FibreFix** window, its intensity scaling and contrast can be adjusted manually by inserting cut-off values in the **High/Low** boxes just below the small image window at the top left. Alternatively, the image properties can be manipulated simply by pressing the right button of the mouse and running the cursor within the image frame either up and down the mat (to change the upper limit) or side to side (to change the lower limit) until the image appears satisfactory. The numerical cut-off values still appear in the **High** and **Low** boxes for future reference. The palette can also be inverted by a single click on the **Invert Palette** button on the left.

XFIX and BSL Functionality in FibreFix

The new **FibreFix** program incorporates many of the features of **XFIX** as well as **BSL**. The user can select points on the image to enable estimation of, for example, the pattern centre, the camera length, the specimen/ detector rotation and the specimen tilt. These and other computed parameters are automatically saved in a parameter file, which can be accessed from the **Edit** drop-down menu under **Parameters**, where the parameters can be inspected and also manually changed if necessary. The

panels in the lower left part of the **FibreFix** window can be toggled between **XFIX** operations and **BSL** operations (Figure 2). A logical procedure in data analysis is to estimate first the image centre and rotation, then to estimate the camera length from peaks of known spacing (if there are any), and then to determine the specimen tilt and other tilt parameters. To estimate the centre and rotation the user clicks on the **Get Points** button under **XFIX**, and then clicks on four equivalent reflections in the four quadrants of the fibre pattern (Figure 1). Precise estimation of the peak centres can be aided by the enlarged window (top left). After left-clicking on four points, clicking the right hand mouse button then brings up a window asking which parameters to determine. The calculated centre and rotation parameters are then stored in the parameter file and are also displayed in the text box below the image, which provides a running record of the procedures carried out, together with the estimated parameter values. This file is automatically saved as a **.log.txt** file at the end of each processing session on a particular image. The window can also be used to **Apply** the centre and rotation parameters to the image. Note that when these parameters are applied, a new, corrected, version of the image is automatically displayed in a new window (Figure 3) and is automatically saved in the directory where the original image came from. For example, the raw datafile in

Figure 1 with filename E01000.BSL was saved as E01000.BSL.ROT after the centre and rotation operations had been applied. This is a general theme throughout the processing - the processed images are saved at each stage and the nature of the saved file is evident from the cumulative file extensions. As mentioned above, the corrected image appears within the **FibreFix** frame as a new window and the original image is retained there too in its own separate window (see Figure 3). Operations such as zooming and intensity scaling apply to each image separately depending on which window is activated (by clicking on it). Different centred and properly oriented images of the same type but from different experiments can then be added together using the **.AVE** (gives an average) or **.SUM** (gives a sum) instruction under **BSL**.

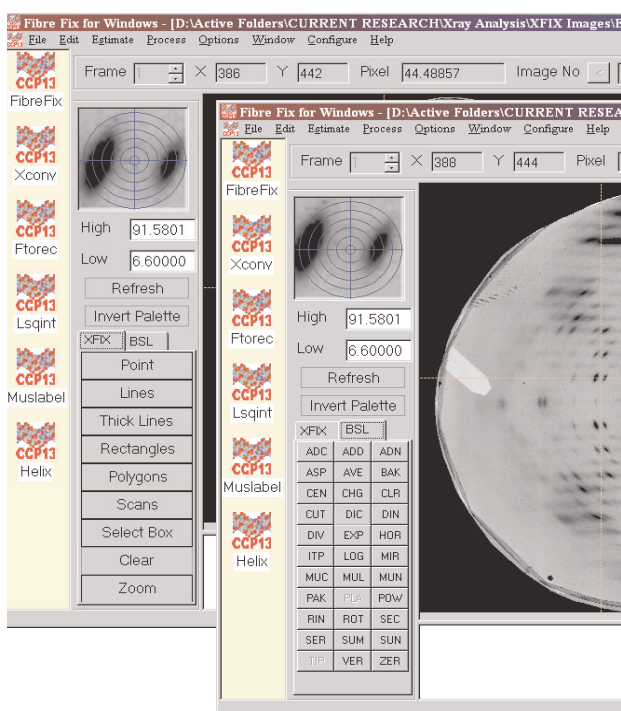


Figure 2: Toggling between the **XFIX** and **BSL** set of operations. Note that some **BSL** options are only active if there is more than one frame in the data.

The next step in the processing procedure is to estimate the camera length if there is a salt ring or specific reflection of known spacing. This can be achieved by first entering the known calibration spacing in Ångstroms into the **Parameter** table under the **Edit** drop-down menu. Then, once any previously selected points or circles on the corrected image have been removed using **Clear**, select **Get Points** from the **XFIX** menu and, for a calibration ring, click on several points around the ring. Right clicking on the mouse and selecting **Estimate distance** from the menu will then estimate the camera length and put this value in the **Parameter** table. If there is only a single reflection of known spacing, click on this reflection and then right click on **Estimate distance** to estimate the camera length. If there is no known calibration peak,

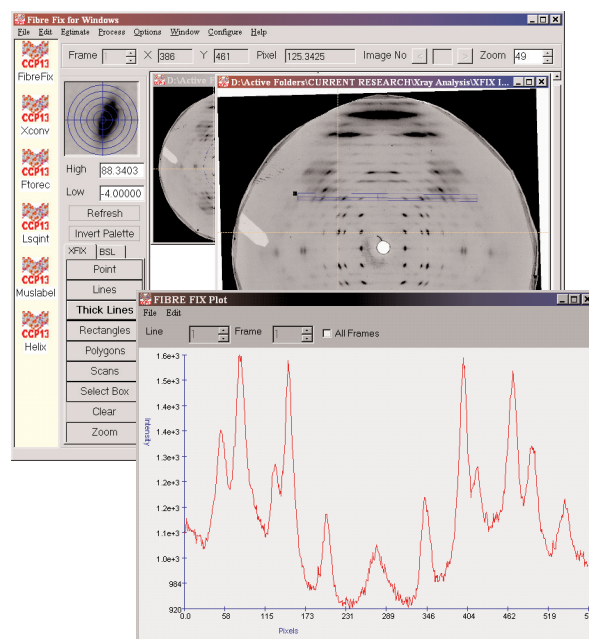


Figure 3: The E-DNA pattern from Figure 1 shown at a reduced scale at the back of the FibreFix frame (top) and the centred, rotated version of the same pattern shown at a larger scale in front. The **XFIX** operation **Thick Lines** is being used to plot the integrated intensity along the rectangle shown up in blue on this pattern. Right clicking on the mouse produces the 1D plot shown at the bottom. This plot can be saved using the **File** drop-down menu, or rescaled using the **Edit** drop-down menu.

then the user needs to estimate manually the camera length in units of detector pixels based on the physically measured length (specimen to detector distance) of the camera and knowing the detector pixel characteristics. This calculated value then needs to be input manually into the **Parameter** table.

The specimen tilt and other tilt parameters cannot be calculated until the camera length is known and input into the **Parameter** table. To estimate the tilt, once again the image should first be cleared, **Get Points** should be selected, and four equivalent reflections carefully selected in the image. Right clicking then allows **Estimate tilt** to be selected. How to check that the tilt is sensible is detailed below in the Section entitled '**Estimating Unit Cell Parameters**'.

Note that in the case of multiframe data from time-resolved experiments, the **FibreFix** program, using **.BAK** under **BSL**, will correct the various time frames both for the beam strength during each frame (e.g. from an ionisation chamber reading in a calibration channel) and for the frame length (if this is not constant through the series), to give a normalised series of frames. It can also subtract a suitably weighted blank cell exposure from each frame in the time series to reduce the background. Different but equivalent time-resolved experiments, suitably processed like this, can then be added automatically frame by frame, to give a normalised, summed, time-series using **.SUM** in **BSL**. Under **BSL** the time series, once corrected as

above, can also be viewed as a movie (using **.PLA**) to allow rapid visual inspection of the data.

Generating 1D Intensity Profiles

A feature of the new software is that such things as intensity profiles along a line, or projected within a rectangle, or taken around an arc in the pattern, or taken radially through a certain angular segment of the data, can now be carried out by very simple operations directly on the image. The user clicks on the appropriate button under **XFIX**, say **Thick Lines**, then chooses two ends of the long axis of the line (a broken line will appear on the image) and then two ends of the short axis, at which point a broken rectangle will appear. If the user then does a right click on the mouse, the intensity profile will be displayed instantly in a new window (Figure 3), where the observed data range along the intensity axis can be adjusted as needed using a drop-down menu (**Edit**). From another drop-down menu (**File**) in that window the profile can be saved either as an image or as a text file for subsequent processing as a 1D array. The old **BSL** operations **.VER** (integrate vertically) and **.HOR** (integrate horizontally) can also be used for this, but the new implementation of these plotting routines under **XFIX** is more versatile in that the lines and rectangles can have any orientation in the image. In using **.HOR** or **.VER** under **BSL**, the user left clicks on two points at opposite corners of a vertical or horizontal rectangle and then a right click brings up the plotted profile as under **XFIX**. Note that the application of the annular mask either as **Scans** under **XFIX** or as **.SEC** and **.RIN** under **BSL** can give either circumferential (angular) intensity plots, useful, for example, in the analysis of textures, or can give radial intensity plots of various kinds as needed for solution scattering analysis.

Note finally that in the case of a time series which has been corrected for beam strength and exposure time as detailed above, the intensity variation of a particular part of the pattern through the series can be plotted by first selecting the area of interest using the **Rectangles** button under **XFIX** and then clicking in **BSL** on the **.TIP** button. This will give a 1D profile of intensity in the chosen rectangle against time that can be scaled or saved as with any of the other 1D plots.

Estimating Unit Cell Parameters

An important part of the analysis of fibre diffraction data is to be able to estimate unit cell parameters from well-sampled patterns. A real advantage of doing this at an early stage is that it immediately shows up whether the chosen image centre, rotation and specimen tilt have been accurately estimated. Clicking on equivalent spots in a pattern is subject to human error, but if a calculated lattice is superimposed on the corrected pattern then it can be immediately obvious if, for example, the centre needs to be moved slightly.

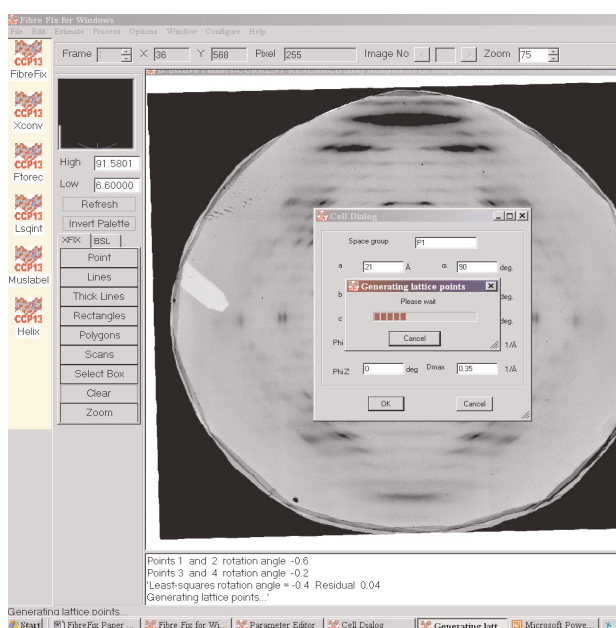


Figure 4: Fitting calculated reciprocal lattice points to the corrected pattern in Figure 1. Clicking on Edit and then Cells allows postulated unit cell parameters to be input. Clicking OK generates the lattice points (see Figure 5). There is a wait box showing that the calculation is proceeding.

Lattice generation can be achieved by using the **Edit** menu in **FibreFix** and clicking on **Cells**. If the user has some idea of the unit cell dimensions then the usual parameters a , b , c and α , β , γ can be input manually, as can the range of spacings in reciprocal space over which the lattice points need to be calculated. Clicking **OK** in the cell dialogue window will then cause calculation of the estimated spot positions and these will be drawn on top of the active image as a series of small circles (in the colour and size specified in the **Options** drop-down menu). This process may take some time depending on the size of the unit cell and the range in reciprocal space over which it is calculated (don't let this range be bigger than necessary), and a 'wait' window appears while the calculation is in progress (Figure 4). Inspection of the fit of the calculated spot positions and the observed peaks will show immediately whether the chosen unit cell is reasonable and whether the plotted lattice points and the image peaks coincide.

Note that if the image and lattice appear too small to see clearly, the whole **FibreFix** frame can be enlarged to **full screen** using the normal Windows top right icons in the **FibreFix** frame and within this enlarged frame the image can be enlarged at will using the **Zoom** facility, also top right. Making the image as large as practicable clearly makes visual inspection of the goodness of fit of the lattice and the intensity peaks much more critical.

After such visual inspection, the unit cell parameters, the centre values and so on can be adjusted easily by the user until a sensible fit is obtained. Proper fitting is usually an iterative process and almost always requires some user intervention to optimise the parameters. Once this has

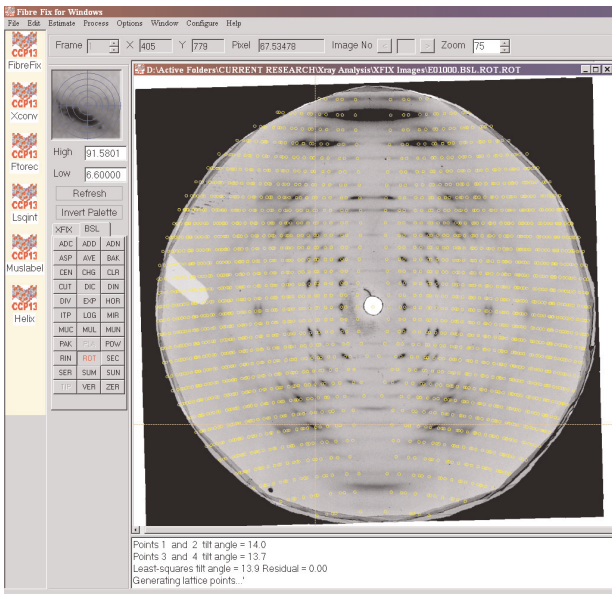


Figure 5: The result of the lattice generation process (see Figure 4) where the predicted reciprocal lattice points are plotted, based on the chosen unit cell parameters and the previously estimated camera length and tilt of the specimen. The lattice points can be changed in size, colour and line thickness under the **Options** drop-down window. This process can show whether the original pattern has been properly centred and rotated and whether the chosen unit cell parameters are sensible.

been done, the parameter values which are retained in the **Parameter** table will be carried forward automatically into **FTOREC** and **LSQINT** where they will be refined as part of the pattern modelling process.

Direct Parameter Feed into FTOREC and LSQINT

One of the advantages of the new integrated program is that parameters determined in the initial **FibreFix** analysis, using the old **XFIX** and **BSL** procedures, and contained in the **Parameter** files, are automatically taken forward into subsequent processing steps, such as **FTOREC** and **LSQINT**. In the **FTOREC** image, diffraction data in the four quadrants of the active image are folded together allowing for the variable sampling of the layer lines by the Ewald sphere. The data are then remapped into reciprocal space. Inspection of this image can show whether the chosen parameters are sensible or not. As mentioned above, satisfactory data analysis is usually an iterative process and the effectiveness of each step in the process needs to be constantly assessed. Assuming that a corrected image is active in the **FibreFix** window, an **FTOREC** image is obtained by clicking on the **Process** drop-down menu and selecting **FTOREC**. This will bring up another dialogue box containing a variety of parameters, many of which have been brought forward from the earlier analysis. If the parameters have been properly determined, the **FTOREC** process should produce an accurately quadrant-folded version of the raw data remapped into reciprocal space. In Figure 6(top) an **FTOREC** image has been superimposed onto one

quadrant of the original image being processed to show its effect. In this case, a muscle diffraction pattern, the diffraction angles are very small, and the specimen tilt angle is close to zero, so the transformation to reciprocal space is not dramatic. For fibre diffraction data at much higher angles, the specimen tilt value becomes particularly critical. It may be necessary to refine the estimated tilt angle by a process of trial and error to obtain an accurately transformed **FTOREC** image. If the **FTOREC** process has been successful, layer-lines in fibre diffraction patterns should become straight horizontal lines of intensity and equivalent peaks from the four quadrants should be properly overlapped and not be spatially separate. It is usually obvious if **FTOREC** is applied with inappropriate parameters.

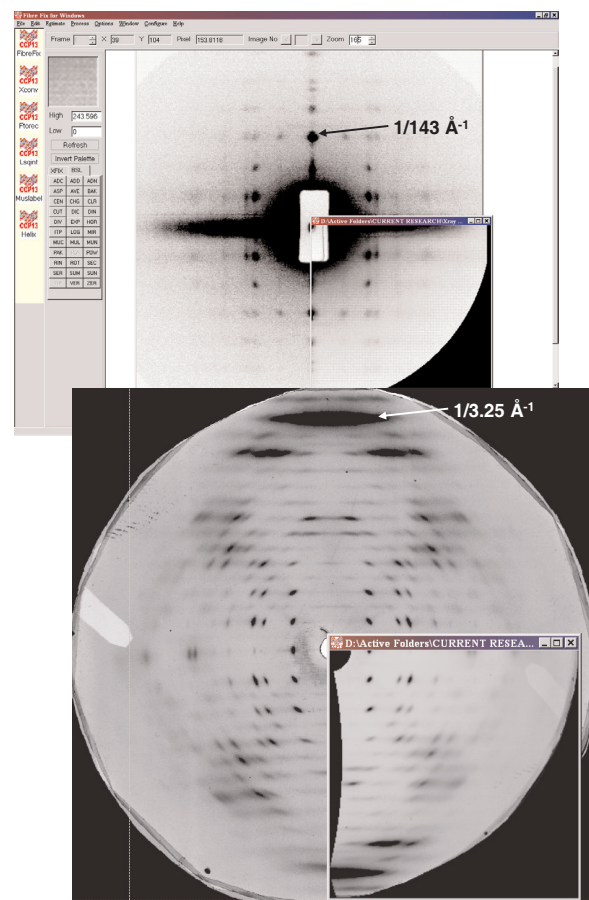


Figure 6: Application of the **FTOREC** process to a low-angle muscle diffraction pattern (top) where the original layer-lines were already rather straight and the fibre tilt was close to zero. **FTOREC** folds the data in each quadrant and remaps the intensities into reciprocal space. In the lower part of the figure the same has been done with the high-angle pattern from E-DNA shown in Figure 1. The original layer-lines are highly curved, the specimen tilt was substantial (about 13.5), but the **FTOREC** output has properly remapped the data to reciprocal space.

Figure 6(bottom) shows an example of a high-angle pattern from E-DNA which has been correctly folded. Once again the **FTOREC** quadrant image with layer-lines that are now straight and horizontal, has been superimposed on the uncorrected image where many of the

layer-lines are clearly curved. Note that a second image showing the standard deviations between the four quadrants is also generated in the **FTOREC** process and this can help to show whether the parameters used in **FTOREC** were accurate.

Background Fitting

Estimation and removal of the background intensity can be carried out either under **FibreFix** or in **LSQINT** (Figure 7). It is recommended that the user carries out initial background fitting in **FibreFix** in order to learn what each method of background does and what the background shape is like. The same background-fitting algorithms are incorporated in both **FibreFix** and **LSQINT**. There are three methods of background estimation (see Denny, 1993): (a) Paul Langan's "roving window" method, (b) calculation of a circularly-symmetric background, and (c) calculation of a "smoothed" background through iterative low-pass filtering based on the method of Ivanova and Makowski (1998). These methods are described in detail within the CCP13 documentation.

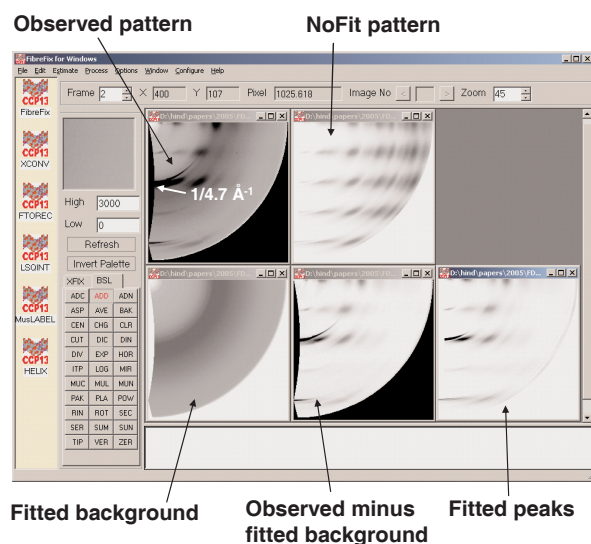


Figure 7: Application of the **LSQINT** fitting procedure to an amyloid fibre diffraction pattern. In the **FibreFix** frame is the **FTOREC** version of the pattern, the **NoFit** image which mimics peak shapes but not intensities, the subtracted background, the observed minus fitted background and the fitted peaks alone. The bottom three figures are all from a single fitting procedure in **LSQINT** where the background, profile parameters, unit cell parameters and peak intensities are refined together. The quality of the fit is quite good and the outer part of the pattern has been totally modelled by the background and not by Bragg peaks, as observed in the original image (top left). Original amyloid data from Dr. Louise Serpell (Sikorski et al., 2003) with permission.

The choice of the background method is entirely dependent on the user, on the type of observed pattern, on the detector, and on the type of specimen used. Therefore, it is necessary that the user tries them all and makes sure that, visually, the background and the background-subtracted pattern look sensible (e.g. the background does

not contain peak information) and that the amount of background subtracted is not so large that a significant number of negative values appears in the subtracted image. Removal of a circularly symmetric background, as might come from scattering from soluble proteins in a native biological fibre specimen, is probably better carried out in **FibreFix** before the pattern is remapped into reciprocal space using **FTOREC**. More background subtraction as well as refinement can then be performed with **LSQINT** on the **FTOREC** data, where the same methods of background fitting appear. The advantage of doing the final background calculation and subtraction with **LSQINT** (Figure 7; see below) is that it refines the background, the profile parameters, the peak intensities and the cell parameters all at the same time. Note that in the latter process the profile of any sampling point (Bragg peak) is trimmed at the edges where the intensity contribution falls below a threshold value. This means that the estimated Bragg peaks have a defined size and shape and this area can then be excluded from the regions of the pattern being used to fit the background.

LSQINT Intensity Fitting: Tutorials on Defined Specimen Types

Assuming that a correctly folded **FTOREC** quadrant image is available, preferably with much of the background already removed, the next step in analysing fibre patterns is to extract suitable intensities from the corrected pattern for further modelling studies. The nature of this extraction process depends on whether the layer-lines consist of Bragg peaks which can be properly fitted with individual h , k and l values to a 3D reciprocal lattice or whether they are continuous, in which case the only meaningful Miller index is the layer-line number l . The program **LSQINT** can deal with both of these situations. For Bragg peaks the **LSQINT** output consists of h , k , l , the multiplicity (M), the integrated intensity (I) of the peak and the standard deviation (σ). In the case of continuous layer-lines the important features are the layer-line number (l), the reciprocal radius along the layer-line (R) and the values of I and σ .

LSQINT processing allows for disorientation in the specimen, for the finite size of the beam and for the intrinsic width and breadth of the diffraction peaks. The fitting of the processed **FTOREC** patterns using **LSQINT** is usually carried out in two stages. The **LSQINT** dialogue window is opened by going to the **Process** dropdown menu in **FibreFix** and selecting **LSQINT**. In the **FileNames & Process** panel of the **LSQINT** dialogue window, selection of the **NoFit** option allows the shapes of the peaks to be determined approximately by visual inspection without any attempt at this stage to fit the intensities. Before clicking on the **Run** button, the **Parameters** part of the **LSQINT** dialogue window can be set. The unit cell parameters will have been brought forward from the earlier analysis. The left hand column of the **Parameters** window contains values relating to the

size and shape of the peaks: **Awidth** is the estimated angular disorientation in the pattern in degrees; **Shape** models different angular distributions ranging from Lorentzian (1) to Gaussian (10). **Zwidth** and **R0width** (both in reciprocal Ångstroms) are related to the broadening due to the specimen itself (**Zwidth** = 1/particle axial size; **R0width** = 1/particle lateral size).

Clicking on the **Limit** tab in **LSQINT** allows selection of the part of the pattern which needs to be fitted, perhaps avoiding the central backstop area and setting a maximum radial position, so that **LSQINT** is not trying to fit non-diffraction parts of the image. With the peak shape parameters put in, clicking on **Run** will generate a **NoFit** image of peaks in the positions defined by the chosen unit cell (Figure 7), but all with equal intensities (apart from differences in multiplicity). This image can then be compared with the original to see if the peak shapes, sizes and disorientations are reasonable. A few iterations of this process will usually produce a sensible **NoFit** pattern.

Proceeding to the full fitting of the pattern, then the choice of appropriate parameter values with which to initiate the **LSQINT** fitting is non-trivial and is not always self-evident, so we have developed a series of tutorials including suggested parameter values for different kinds of specimen. These include crystalline fibre diffraction data from a DNA sample (E-DNA), continuous layer-line data from another type of DNA (TpA), sampled but highly disoriented patterns from amyloid fibres (original pattern courtesy of Dr. Louise Serpell; Sikorski *et al.*, 2003), and low-angle X-ray diffraction patterns from muscle, including time-resolved data (e.g. Harford and Squire, 1992; Squire *et al.*, 2004). An example of an amyloid pattern fitted using **LSQINT** is shown in Figure 7. Note that there are several data output formats from **LSQINT**, including Bragg reflection data in CCP4 format.

The **FibreFix** tutorials can be accessed on the CCP13 website (<http://www.ccp13.ac.uk>) or by clicking the **Help** drop-down menu in the **FibreFix** window. It is our intention to add further tutorials to this as new specimen types are processed. If anyone has particular needs in this for their own particular specimen or has suggestions about the addition of further tutorials then please contact Ganeshalingam Rajkumar (g.rajkumar@imperial.ac.uk).

Other Applications

Note that **BSL** has some other new features. In an application, where, for example, the data consist of a time-series, this series can be displayed using **.PAK** under **BSL** to display them on a chosen raster (Figure 8). In another application where a series of images is obtained by physically mapping across a specimen in a raster, as might occur in microbeam mapping of materials with a texture, the whole series can be plotted as a tiled array in **FibreFix** using the **BSL** instruction **.SER** to make a single file from all the recorded images and then **.PAK** to display them on a raster as before.

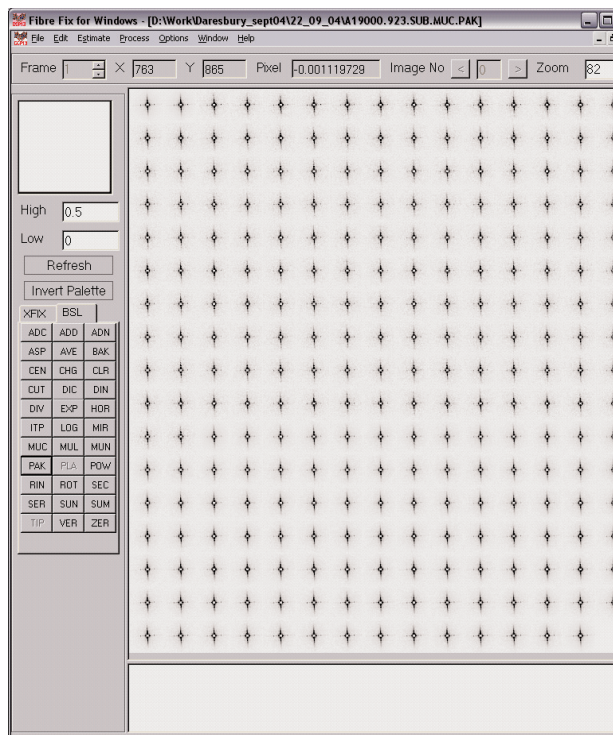


Figure 8: Mapping a series of frames in a single file into a 2D array of images. The original file could be a corrected time series, in which case the new **BSL** operation **.PAK** will display the whole series on a chosen raster, or the original data could be a series of separate files, perhaps obtained in a microbeam scan across a material with varying texture. In the latter case the files need to be collated into a single multiframe file using the **.SER** operation in **BSL**, after which the **.PAK** operation can be carried out as before. Original data here from Eakins *et al.* (unpublished).

Note that the **FibreFix** window also allows all the original CCP13 programs (**XCONV**, **FTOREC**, **LSQINT**) to be used independently if desired. It also incorporates the modelling programs **HELIX** and **MusLABEL** (Knupp and Squire, 2004; Squire and Knupp, 2004), with which to simulate diffraction patterns from helices with different parameters.

Conclusion

The next challenge in the implementation of the strategy described by Squire *et al.* (2003), apart from further development of **FibreFix** and its implementation in JAVA and thus make it platform-independent, is to include modelling programs within the CCP13 suite. These will simulate and refine molecular structures at high resolution (e.g. nucleic acids, crystalline polymers, polysaccharides etc) or molecular assemblies from components of known structure (e.g. from protein crystallography). The programs **LALS** (Okada *et al.*, 2002) and **FXPLOR** (Denny *et al.*, 1997) are being developed for the former application and the program **MOVIE** (Hudson *et al.*, 1997; AL-Khayat *et al.*, 2003; 2004) is being enhanced for exploration of molecular assemblies. It is intended that each of these programs will in due course be part of the CCP13 suite, and that each will have useful manuals

and tutorials.

Acknowledgements

We are indebted to support from the BBSRC/EPSRC (#28/B15281) for the CCP13 grant which funded AH and GR during the first part of the development of this package, the support of the Wellcome Trust (#061729) for the muscle aspects of this development and the support of the BHF for HA (#PG/02/054/13776).

References

- AL-Khayat, H.A., Hudson, L., Reedy, M.K., Irving, T.C. & Squire, J.M. (2003) Myosin head configuration in relaxed insect flight muscle: X-ray modelled resting crossbridges in a pre-powerstroke state are poised for actin binding. *Biophys. J.* 85, 1063-1079.
- AL-Khayat, H.A., Hudson, L., Reedy, M.K., Irving, T.C. & Squire, J.M. (2004) Modelling oriented macromolecular assemblies from low-angle X-ray fibre diffraction data with the program MOVIE: insect flight muscle as an example. *Fibre Diffraction Review* 12, 50-60.
- Denny, R.C. (1993) Integration of Fibre Diffraction Patterns: FTOREC and LSQINT. *Fibre Diffraction Review*. 2, 5-8.
- Denny, R.C. (1996) Fibre Diffraction Spot Profiles and the Lorentz Correction. *Fibre Diffraction Review* 5, 24-27.
- Denny, R.C., Shotton, M. & Forsyth, V.T. (1997) X-PLOR for polycrystalline Fibre Diffraction. *Fibre Diffraction Review* 6,30-33.
- Fraser, R.D.B. (1994) Digital Processing of Fibre Diffraction Patterns. *Fibre Diffraction Review* 3, 8-11.
- Fraser, R.D.B., MacRae, T.P., Miller, A. & Rowlands, R. (1976) Digital Processing of Fibre Diffraction Patterns. *J. Appl. Cryst.* 9, 81-94.
- Harford, J.J. & Squire, J.M. (1992) Evidence for structurally different attached states of myosin crossbridges on actin during contraction of fish muscle. *Biophys. J.* 63, 387-396.
- He, A., Rajkumar, G., Forsyth, T. & Squire, J.M. (2004) Report on CCP13 software developments: Production of an integrated CCP13 environment (ICE) for Windows. *Fibre Diffraction Review* 12, 21-23.
- Hudson, L., Harford, J.J., Denny, R.J. & Squire, J.M. (1997) Myosin head configurations in relaxed fish muscle: resting state myosin heads swing axially by 150Å or turn upside down to reach rigor. *J. Mol. Biol.* 273, 440-455.
- Ivanova, M.I. & Makowski, L. (1998) Iterative Low-Pass Filtering for Estimation of the Background in Fiber Diffraction Patterns. *Acta Cryst. A*54, 626-631.
- Knupp, C. & Squire, J.M. (2004) HELIX: A helical diffraction simulation program. *J. Appl. Cryst.* 37, 832-835.
- Okada, A., Noguchi, K., Okuyama, K & Arnott, S. (2002) WinLALS for a linked-atom least-squares refinement program for helical polymers on windows PCs. *Comput. Biol. Chem.* 27, 265-285.
- Shotton, M.W. & Denny, R.C. (1999) CCP13 Software Development. *Fibre Diffraction Review* 8, 14-19.
- Sikorski, P., Atkins, E.D.T. & Serpell, L.C. (2003) Structure and Texture of Fibrous Crystals Formed by Alzheimer's A (11-25) Peptide Fragment. *Structure* 11, 915-926.
- Squire, J.M. & Knupp, C. (2004) MusLABEL: A Program to Model Striated Muscle A-band Lattices, to Explore Crossbridge Interaction Geometries and to Simulate Muscle Diffraction Patterns. *J. Mus. Res. Cell Motil.* 25, 423-438.
- Squire, J.M., AL-Khayat, H.A., Arnott, A., Crawshaw, J., Denny, R., Diakun, G., Dover, S.D., Forsyth, V.T., He, A., Knupp, C., Mant, G., Rajkumar, G., Rodman, M.J., Shotton, M. & Windle, A.H. (2003) New CCP13 software and the strategy behind further developments: Stripping and modelling of fibre diffraction data. *Fibre Diffraction Review* 11, 7-19.
- Squire, J.M., Roessle, M. & Knupp, C. (2004) New X-ray diffraction observations on the structure of the vertebrate muscle A-band with interpretations based on C-protein (MyBP-C), troponin, titin and nebulin. *J. Mol. Biol.* 343, 1345-1363.

New Functionality in CORFUNC

Stephen King and Damian Flannery

ISIS Facility, Rutherford Appleton Laboratory, Chilton, OX11 0QX, UK

Introduction

CORFUNC is the CCP13 program suite for correlation function analysis [1]. Fundamentally, a correlation function describes how the density varies with distance along a given direction in a sample, for example a semi-crystalline polymer. Parameters that characterise the microstructure of the sample may then be derived from it.

In soft condensed matter science there are analogous functions that describe how the density, or volume fraction, of an adsorbate (such as a surfactant or polymer) varies with distance along the direction normal to an interface (such as the surface of a colloidal particle). This is illustrated schematically in Figure 1.

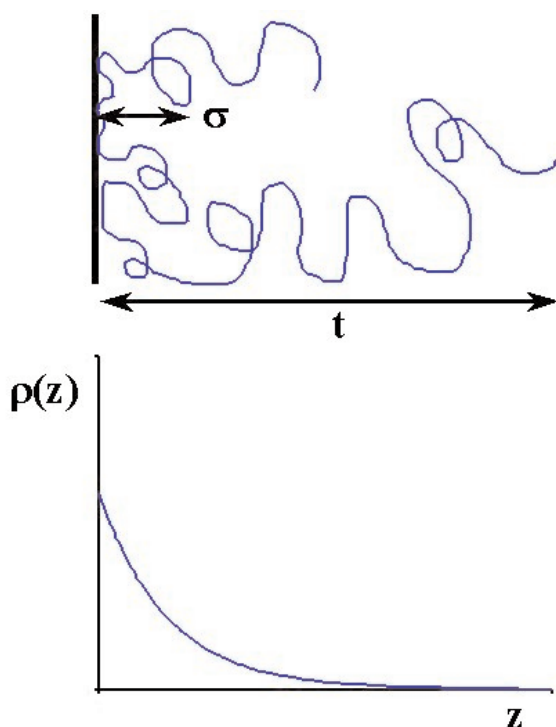


Figure 1: Schematic representation of a polymer molecule adsorbed at a solid interface and the resulting volume fraction profile.

These functions are called the *segment density distribution and volume fraction profile*, respectively, and experimentally are most conveniently measured by "Solution"

Small-Angle Neutron Scattering (SANS). Examples of the sort of colloidal system for which this type of analysis is routinely conducted are dispersions of sterically stabilised pigment particles (such as are found in paint), or dispersions of sterically stabilised liquid emulsion droplets (such as are used in cosmetic, food or pharmaceutical formulations).

The volume fraction profile, $\Phi(z)$, and the segment density distribution, $\rho(z)$, are inter-related through

$$\Phi(z) = \frac{\rho(z) \Gamma}{\Delta} \quad (1)$$

where Γ is the amount of surfactant/polymer adsorbed (with dimensions of mass per unit area) and Δ is the bulk density of the adsorbate (as mass per unit volume).

$\Phi(z)$ provides the most detailed description of the average internal structure of an adsorbed layer [2, 3]. In addition to showing how the adsorbate is arranged in the vicinity of the interface, it also allows several measures of the layer thickness, the adsorbed amount (from the integral under the curve) and the average fraction of segments "bound" at the interface (from the segment density within, say, the first nm) to be derived.

The Scattering from Adsorbed Layers

The SANS from a dispersion of colloidal particles (which are assumed to be spherical) with adsorbed layers may be written

$$\frac{\partial \Sigma}{\partial \Omega}(Q) = N_p P(Q) S(Q) + B \quad (2)$$

where N_p is the number concentration of particles, $S(Q)$ is the interparticle structure factor and B is the background signal. $P(Q)$, the *form or shape factor*, may then be expressed as [4, 5, 6]

$$P(Q) = [(\rho_p - \rho_m) F_p(Q) + (\rho_l - \rho_m) F_l(Q)] \quad (3)$$

where ρ is the neutron scattering length density (with dimensions of length^{-2}) with the subscript "m" signifying the dispersion medium and the subscript "l" the adsorbed layer, $F_p(Q)$ represents the *intraparticle form factor for the core particle* and $F_l(Q)$ represents the *intralayer form*

factor for the adsorbed polymer. $(d\Sigma/d\Omega)(Q)$ thus has dimensions of $(\text{length})^{-1}$ and is normally expressed in absolute units of cm^{-1} . In this type of experiment it is usually arranged that $S(Q)$ and B make a minimal contribution to $(d\Sigma/d\Omega)(Q)$; e.g. $N_p < 5\%$ and there is little or no free polymer in the dispersion medium.

If the curvature of the interface is small compared to Q , that is, if $QR_p \gg 1$, then the bracketed term in Equation 3 may be expanded to give

$$P(Q) = [(\rho_p - \rho_m)^2 F_p(Q)^2] + \quad (4a)$$

$$2(\rho_p - \rho_m)(\rho_l - \rho_m) F_p(Q) F_l(Q) + \quad (4b)$$

$$[(\rho_l - \rho_m)^2 F_l(Q)^2] \quad (4c)$$

from which it can be seen that Equation 4a (here called $I_{pp}(Q)$, but also called $I_2(Q)$ or $I_{gg}(Q)$ in the literature) describes the contribution to $P(Q)$ arising from the core particle, Equation 4c (here called $I_{ll}(Q)$, but also called $I_0(Q)$ or $I_{pp}(Q)$ in the literature) describes the contribution from the adsorbed layer, and Equation 4b (here called $I_{pl}(Q)$, but also called $I_1(Q)$ or $I_{pg}(Q)$ in the literature) is a particle-surface interference term. These three terms may be written explicitly thus

$$I_{pp}(Q) = (\delta_p - \delta_m)^2 \frac{2\pi A_p}{Q^4} \left[1 + \frac{1}{Q^2 R_p^2} \right] \quad (5)$$

$$I_{pl}(Q) = (\delta_p - \delta_m)(\delta_l - \delta_m) \frac{4\pi A_p}{Q^4} \times \left[\int_0^t \rho(z) \cos(Qz) dz - QR_p \int_0^t \rho(z) \sin(Qz) dz \right] \quad (6)$$

$$I_{ll}(Q) = (\delta_l - \delta_m)^2 2\pi A_p \times \left[\frac{1}{Q^2} \left| \int_0^t \rho(z) \exp(iQz) dz \right|^2 + \tilde{I}_{ll} \right] \quad (7)$$

A_p is the surface area per unit volume of a t is the maximum extent of the adsorbed layer

\tilde{I}_{ll} describes fluctuations in the adsorbed layer.

\tilde{I}_{ll} is generally unimportant except in a few special cases in systems with densely grafted layers.

It will be noted that Equation 5 is simply a modified Porod law.

When the particles are at contrast match with the dispersion medium (i.e. $\rho_p = \rho_m$), $P(Q)$ in Equations 4a - 4c reduces to Equation 7. Unfortunately, because it is the

of the integral that is measured

$\exp(i\varphi Q)$, where φ is unknown. as a phase $\rho(z) = 0$ for $z < 0$. Equation 7 is φ to be

$\partial \varphi / \partial Q$ and $\partial \text{Ln} \left| \int \rho(z) \exp(iQz) dz \right| / \partial Q$ 5]. With a knowledge of φ , $\rho(z)$ can then be obtained from $I_{ll}(Q)$ scattering data.

Q to prevent Gibbs

This procedure always generates a possible $\rho(z)$ that is model-independent. Unfortunately, the Hilbert transformation is not guaranteed to produce a unique distribution and so back-transformation must be treated with caution.

It is possible to obtain $\rho(z)$ by Fourier transformation of off-contrast $I_{pl}(Q)$ data, but experimentally this procedure involves subtracting a large background from a small signal and is thus not particularly well-conditioned. The new routines incorporated into CORFUNC and which are described below assume that the input scattering data is on-contrast (i.e. at contrast match).

Analysis of the Volume Fraction Profile

Invariably one has a reasonable estimate of the adsorbed amount Γ from other techniques and this allows $\Phi(z)$ to be iteratively normalised to Equation 1 given that

$$\int_0^t \Phi(z) dz = \frac{\Gamma}{\delta} = M \quad (8)$$

The n -th moment of the volume fraction profile can then be defined as

$$\langle z^n \rangle = M^{-1} \int_0^t \Phi(z) z^n dz \quad (9)$$

from which the root-mean-square thickness, t_{rms} , and the second moment about the mean (or standard deviation), σ , of the volume fraction profile may be defined as

$$t_{rms} = \langle z^2 \rangle^{1/2} \quad (10)$$

$$\sigma = \left[\langle z^2 \rangle - \langle z \rangle^2 \right]^{1/2} \quad (11)$$

respectively. Physically, σ provides an estimate of the average distance of the centre-of-mass of the adsorbed layer from the interface.

An additional parameter that can be determined is the bound fraction, $\langle p \rangle$, given by the expression:-

$$\langle p \rangle = \int_0^l \Phi(z) dz / \int_0^l \Phi(z) dz \quad (12)$$

This is the average fraction of segments in an adsorbed surfactant/polymer molecule that are "bound" to the interface. Although intuitively it may seem sensible to choose l to be the length of one segment, say, ≤ 0.5 nm, in practice it is better to choose a larger value in order to offset the effects of any interfacial inhomogeneities. By scaling experimental data from simple systems to simulated data from contemporary mean-field theories it has been suggested that one lattice layer in a simulation corresponds to a distance of 1.3 nm [2]. On this basis the software has been coded to take a more pragmatic approach and to use $l = 1$ nm.

Implementation within CORFUNC

The reason for choosing to add this new functionality to *CORFUNC* was quite simply that the program suite already included tried and tested data extrapolation routines of the sort necessary to pre-process scattering data from adsorbed layers prior to Hilbert inversion.

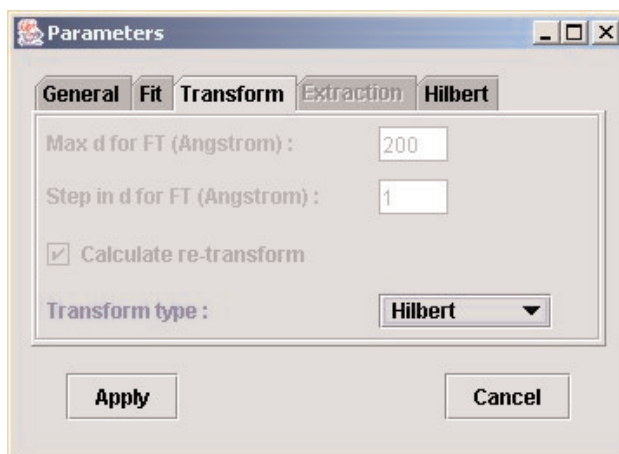
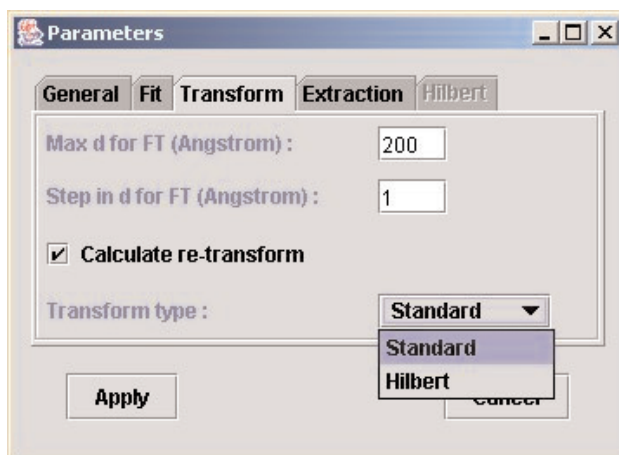


Figure 2: Two views of the new Edit - Parameters window showing how the transform type selection activates the Hilbert tab.

The software design principles necessary to incorporate the new analysis routines into *CORFUNC* have already been described [7]. Below the changes to the Graphical

User Interface (GUI) are described.

The most noticeable change is the addition of an extra "tab", called **Hilbert**, to the **Edit - Parameters...** window. This tab is only activated if **Transform type** on the **Transform** tab is set to "Hilbert". At the same time the **Extraction** tab is disabled, see Figure 2.

To perform conventional correlation function analysis Transform type should be set to "Standard". *CORFUNC* will then operate as it has always done. But having selected "Hilbert" it is then necessary to enter parameters in the Hilbert tab, see Figure 3.

If the dimensions of the Q-axis are not identified correctly the normalisation of the volume fraction profile will be wrong. The Normalisation accuracy is the maximum acceptable difference between the specified Adsorbed amount and the integral of the volume fraction profile (see Equation 8).

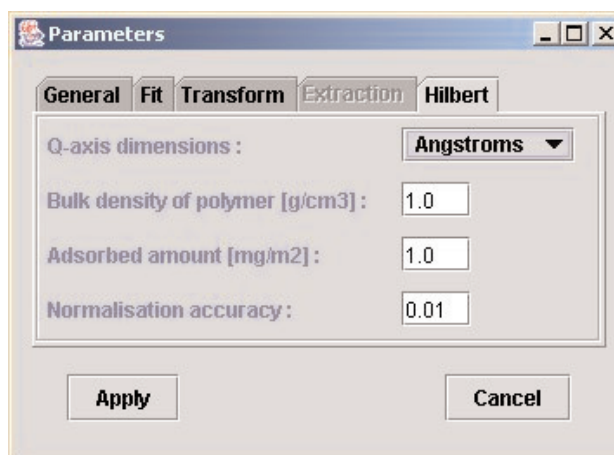


Figure 3: The Edit - Parameters - Hilbert tab.

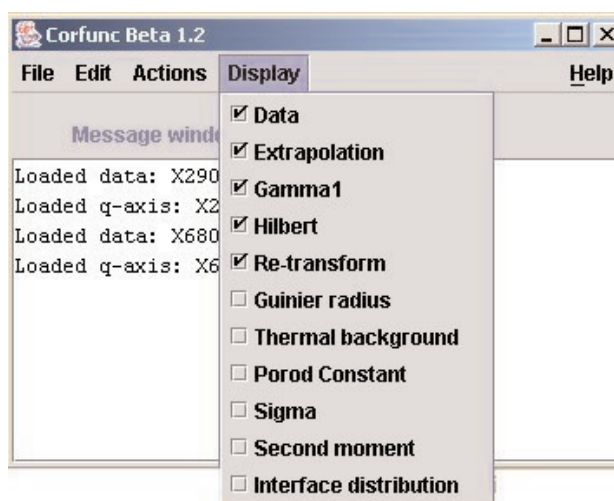


Figure 4: The Display menu.

The **Display** menu has also been updated, as shown in Figure 4. Only the **Data**, **Extrapolation** and **Hilbert**

options have any meaning if **Transform type** is set to "Hilbert" (although the other options are not disabled).

Generating a Volume Fraction Profile

The sequence of actions necessary to generate a volume fraction profile is:

File ==> Load data...

File ==> Load q-axis...

At this point a graph of the data is drawn if **Data** is checked in the **Display** menu, Figure 5.

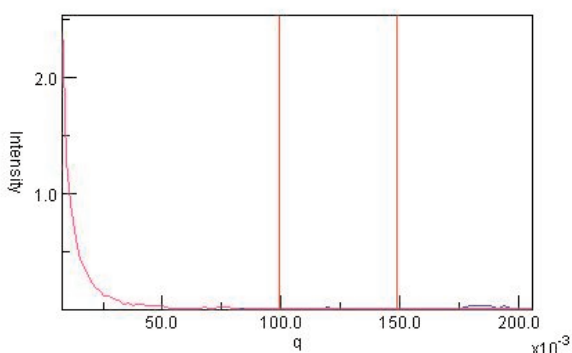


Figure 5: Typical SANS data from a sterically stabilised dispersion of colloidal particles (blue curve) overlaid by the extrapolation (purple curve).

Move the left-hand limit marker to $q=0$.

Move the central and right-hand limit markers to define the "tail" region of the data that is to be extrapolated to high-Q (in this example the region $50 \times 10^{-3} < q < 100 \times 10^{-3}$ would suffice).

Edit ==> Parameters...

General: select **Data scale:** "Absolute"

Fit: select **Back extrapolation:** "Guinier"

Fit: select **Tail fit:** "Porod"

Transform: uncheck **Calculate re-transform**

Transform: select **Transform type:** "Hilbert"

Hilbert: select **q-axis dimensions**

Hilbert: enter the **Bulk density**

Hilbert: enter the **Adsorbed amount**

Hilbert: enter the **Normalisation accuracy**

Click **Apply**

Actions ==> Extrapolate

At this point the extrapolated data will be drawn over the input data if **Extrapolation** is checked in the **Display** menu, Figure 5.

If the extrapolation is acceptable:

Actions ==> Transform

At this point another graph window will open displaying the volume fraction profile if **Hilbert** is checked in the **Display** menu, Figure 6.

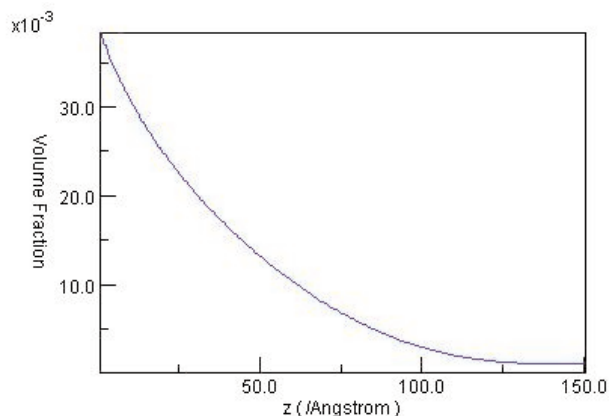


Figure 6: The volume fraction profile derived from the extrapolated SANS data in Figure 5.

Note that **Actions - Extract parameters** has *no meaningful effect* when **Transform type** is set to "Hilbert". Analysis of the volume fraction profile, as described above, is performed automatically.

Acknowledgements

We would like to thank Dr Nick Terrill and Prof. Terry Cosgrove for their help in testing the software.

References

- [1] Ryan, A.J. SAXS Correlation Functions: New Software at Daresbury. *Fibre Diffraction Review*, 3, 25 (1994).
- [2] Fler, G.J., Cohen Stuart, M.A., Scheutjens, J.M.H.M, Cosgrove, T., Vincent, B. *Polymers at Interfaces*, Chapman & Hall, London (1993).
- [3] Cosgrove, T. Volume-fraction Profiles of Adsorbed Polymers. *J. Chem. Soc. Faraday Trans.*, 86, 1323-1332 (1990).
- [4] Crowley, T.L. D.Phil Thesis. University of Oxford, (1984).
- [5] Cosgrove, T., Crowley, T.L., Vincent, B., Barnett, K.G., Tadros, Th.F. *The Configuration of Adsorbed Polymers at the Solid-Solution Interface*. Faraday Symposium of the Chemical Society, No.16, Royal Society of Chemistry, London, (1981).
- [6] King, S.M., Griffiths, P.C., Cosgrove, T. Using SANS to Study Adsorbed Layers in Colloidal Dispersions. Chapter 4, *Applications of Neutron Scattering to Soft Condensed Matter*, Gabrys, B.J. (editor), Gordon & Breach, Amsterdam (2000).
- [7] Rodman, M. Development of CORFUNC. *Fibre Diffraction Review*, 12, 24 (2004).

Intensity Analysis of Myosin-based X-ray Meridional Reflections from Live Skeletal Muscles in Relaxed and Contracting States

Kanji Oshima¹, Yasunori Takezawa¹, Yasunobu Sugimoto¹, Thomas C Irving²
and Katsuzo Wakabayashi^{1*}

1. Structural Biophysics Laboratory, Division of Biophysical Engineering, Graduate School of Engineering Science, Osaka University, Toyonaka, Osaka 560-8531, Japan

2. BioCAT and CSRRI, Department of Biological, Chemical and Physical Sciences, Illinois Institute of Technology, Chicago, Illinois 60616, USA

* Corresponding author.

Abstract

Intensity analysis of the myosin-based meridional reflections in the high-resolution X-ray fibre diffraction patterns of live frog skeletal muscles has been performed to elucidate a more detailed structural model for the myosin crown periodicity and the axial disposition of two-headed crossbridges along thick filaments in a sarcomere. Analysis of X-ray interference between the two-headed crossbridge arrays in opposite halves of each thick filament allows us to determine the location of crossbridge arrays with a perturbed periodicity along the thick filament. Modelling studies have revealed that the thick filament has a mixed structure of two different periodicities for the arrangement of myosin crossbridge crowns in the relaxed state, consistent with previous results [3,12] and that such a mixed structure remains and the crown periodicities and the axial disposition of two-headed crossbridges alter when muscles go from the relaxed to an isometrically contracting state: the perturbed regions shrink with a change in inter-crown repeat and each head of a myosin crossbridge in a pair is closer to its neighbour than in relaxed muscles. Several factors have significant influences on the intensities of the myosin-based meridional reflections.

Introduction

Muscle contraction takes place when thin actin and thick myosin filaments interact and slide past each other, powered by the hydrolysis of ATP. Structural changes of both filaments in contracting muscle are thought to play an important role in force generation mechanism during muscle contraction. Detailed atomic structural models of actin filaments have been proposed [1,2], but little is known about the precise structure of myosin filaments of vertebrate skeletal muscles in relaxed and contracting states although some modelling studies of X-ray data [3,4] and three-dimensional reconstruction of electron microscopic images [5,6] have been made.

X-ray fibre diffraction patterns from relaxed vertebrate skeletal muscles show a series of strong myosin-based layer-line reflections including reflections on the meridian that index to a crystallographic period of 42.9 nm. When muscles contract, the myosin-based layer-line reflections are markedly weakened by disordering of the helical disposition of the two-headed myosin projections due to actomyosin interaction during force generation. But the meridional reflections at orders $3n$ (n an integer) of the basic period are strong and the other order reflections may still be observed although with a weakened intensity. From a structure such as a myosin crown arrangement with a regular subunit repeat of 14.3 nm within a 42.9 nm basic repeat, only reflections that index

to orders of 14.3 nm can appear on the meridian. However, a series of meridional reflections which index to a 42.9 nm-period in the relaxed state and a 43.5 nm-period in the contracting state have always been observed [7]. Such features in relaxed muscle have been thought to originate from systematic perturbations in the axial repeat of the myosin crossbridge crowns within the crystallographic period [8,9]. All these meridional reflections are sampled by interference between the two symmetrical halves of the thick filament centred on the M-line in a sarcomere [10,11]. From such sampled myosin-based meridional reflections from relaxed skeletal muscles, Malinchik and Lednev [3] modelled a myosin filament with two regions consisting of different periodicities of 14.3 nm and 42.9 nm.

We have analyzed the sampling periods in the myosin-based meridional reflections in X-ray diffraction patterns with higher angular resolution from live frog skeletal muscles in relaxed and contracting states in order to precisely determine the location of crossbridge arrays with a perturbed periodicity along the myosin filament in a sarcomere. In this analysis, the myosin crown periodicity and the axial disposition of two-headed myosin crossbridges along the thick filaments in relaxed and contracting states were simulated. The present analysis required some significant modifications of the findings that were reported previously [3,12]. Here we present some of our

findings in preliminary form.

Experimental

Live sartorius muscles from bullfrog (*Rana catesbeiana*) were used for X-ray studies. Intact muscles were mounted in a chamber with two Mylar windows for X-rays to pass through. Chilled frog Ringer solution was circulated through the chamber. X-ray diffraction experiments were performed at 10°C by using collimated synchrotron X-rays with a wavelength of 0.150 nm from the bending magnet source on the beamline 15A1 [13] at the Photon Factory (Tsukuba, Japan). Two-dimensional X-ray diffraction patterns from relaxed and isometrically contracting muscles were recorded with an image plate (Fuji Film Co., Tokyo) at the specimen-to-detector distance of ca. 2.4 m to measure the first to the eleventh order myosin-based meridional reflections as described previously [14].

Muscles with a full overlap length between thin and thick filaments in a sarcomere were electrically stimulated at 10 °C under isometric conditions for 1.4 s with trains of 1-ms supramaximal current pulses. Data during an isometric contraction were taken in a 1-s exposure when the force had reached its plateau phase, and the measurements were repeated ten times with resting intervals of 90 s between contractions to accumulate X-ray data on the same image plate. X-ray data of relaxed muscles were collected in a 1-s exposure \times 10 before stimulation. Diffraction patterns of four muscles were used after performing an appropriate scaling. The intensities of the myosin-based meridional reflections above the background level in the X-ray patterns were obtained by radial integration of the data in the very narrow range of 0 - 8.5×10^{-4} nm⁻¹, since we were investigating the structure of a myosin filament projected onto the fibre axis. The intensity profile of each reflection was deconvoluted by Gaussian functions, providing its integrated intensity and peak position. In order to correct the effect of lattice sampling on the intensities of the myosin-based meridional reflections, the intensity of each reflection on the meridian was multiplied by the square of its radial width so that the reflection volume in reciprocal space is identical in both states.

In order to measure precisely the separation between the closely-spaced peaks within the myosin-based meridional reflections arising from interference between the arrays in the two halves of each myosin filament centred on the M-line in a sarcomere, X-ray diffraction experiments were also carried out at the 18ID beamline (BioCAT) at the Advanced Photon Source (Argonne, USA) [15,16]. Muscles were stimulated by using the same protocol as above. X-ray patterns of muscles were recorded with a CCD detector [17] with a spatial resolution of ~60 μ m at the specimen-to-detector distance of ca. 5 m by using highly collimated synchrotron X-rays ($\lambda=0.1033$ nm) from the multipole undulator source. X-ray data with an order-to-order resolution of ~6000 nm, much higher angular resolution than were obtainable previously, were

collected in 100 ms- to 500 ms-exposure time in relaxed and contracting muscles, and the data from four muscles were used.

Modelling of thick myosin filaments

One-dimensional models of the myosin filaments projected onto the fibre axis were constructed to calculate the intensities of meridional reflections by assuming that the contributions of C-protein, other accessory proteins and the M-line structure have a minor effect on those intensities. In particular, the C-protein periodicity is known to be slightly different from the myosin periodicity. The intensities of the myosin-based meridional reflections are generally determined by interference between the diffraction from the myosin projections and that from the backbone [18]. We did not take into consideration the contribution to the intensities of myosin-based reflections from the backbone, because we have no information on the phase relationship between the diffraction from myosin projections and that from the backbone. To model the crossbridge arrangement along the whole thick filament we used the intensities of the second to the eleventh order reflections with a basic period of 42.9 nm in the relaxed state and of 43.5 nm in the contracting state. The intensity of the first order reflection was less than that of the fourth order reflection although it was hard to measure due to its partial overlap with the first order C-protein-based reflection. According to electron microscopic data, ca. 50 crossbridge crowns are located in each half of the thick filament with an average repeat of 14.3 nm with a bare zone lacking crossbridges in the centre of the filament that is ca. 160 nm long [19]. In our simulation, the length of the bare zone was varied in the transition of muscle from the relaxed state to the contracting state. In the modelling studies, we assumed a mixed structure consisting of triplet and singlet repeating units of crossbridges as was suggested by Malinchik and Lednev [3] (see below). The triplet repeating structure (a unit cell) of crossbridges has a 42.9-nm periodicity, within which the three myosin crown levels deviate from the regular 14.3 nm-repeat. The singlet structure has a 14.3-nm periodicity. Hereafter the regions containing the triplet structures and the singlet structures are referred as perturbed regions and regular regions on the filament, respectively. The same definitions apply to a contracting muscle, but the triplet repeat is 43.5 nm and the singlet repeat is 14.5 nm. The location of the perturbed region on the filament can be determined by analyzing the sampling period of the meridional reflections. As neither the length of the perturbed region nor that of the regular region is known, the number of crossbridge levels in each region is taken to be variable. In order to perform more detailed modelling of the myosin pattern than was done previously [3,12], we introduced a number of parameters that describe the projected structure of a two-headed crossbridge in both regions. The projected densities of individual heads of each crossbridge were approximated by Gaussian functions. Thus eleven parameters in total were allowed to

vary independently; the width (a_r , b_r and a_p , b_p) of projected density of each myosin head, the distances (d_r , d_p) (r,p; regular and perturbed regions, respectively) between two heads of a crossbridge, the shifts (δ_1 , δ_2) of the crown level from the regular repeat (14.3 nm or 14.5 nm) in the triplets, the number of the crossbridges (l , k) in the singlet and triplet regions, and the total number (C) of the crossbridge crown levels in a half of the thick filament (see Fig. 4). The most probable values of these parameters were determined by searching the best fit between the calculated intensities and the observed ones of the meridional reflections to minimize the R-factor that was defined previously [12].

Our simulation searched for the global minimum in a parameter space which consists of eleven parameters. The range of parameters was restricted within physically reasonable boundaries. As mentioned above, the fact that the intensity of the first order reflection is very weak (less than the fourth order intensity) in both states was taken into consideration.

Results and Discussion

X-ray diffraction patterns taken at the APS had much higher angular resolution than those taken at the Photon Factory and previous data [3], making more precise modelling possible. The myosin-based meridional reflections were clearly sampled axially by interference between the two symmetrical halves of a thick filament centred on the M-line in a sarcomere in both relaxed and contracting muscles (Fig. 1A). Under the assumption of a mixed structure of a myosin filament, the axial sampling on the reflections (M1, M2, M4....), except for those of order $3n$, should come from the separation between the two regions with a 42.9-nm basic period centred on the M-line where the crown levels are systematically perturbed, although the apparent spacing of the sampled pattern tends to be longer than the interference distance [20]. This was confirmed by our simulation of the observed intensity data below. On the other hand, the $3n$ order reflections should be subjected to sampling effects from both the perturbed and regular regions on the thick filaments. Figure 1A and B show such interference peaks of the myosin-based meridional reflections from relaxed and

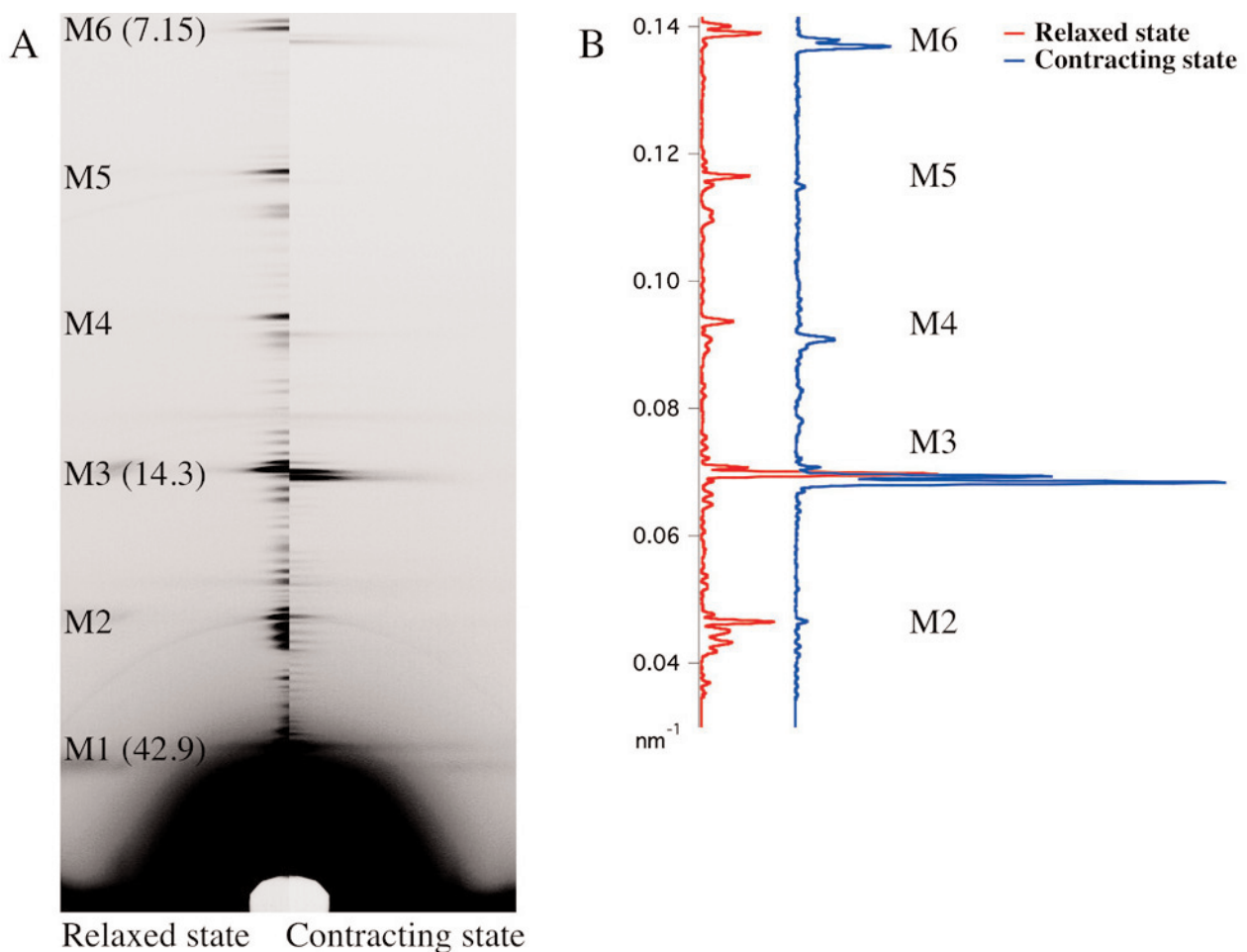


Figure 1: A. X-ray diffraction patterns of frog sartorius muscles taken at APS. Left side is in the relaxed state and right side is in the contracting state with the meridional axis coincided. M1 to M6 denote the first to the sixth order myosin-based meridional reflections with a basic period of 42.9 nm or 43.5 nm. B. Intensity distributions of the meridional reflections. Fine peaks on the myosin reflections are caused by interference between two halves of thick filament centred on the M-line in a sarcomere.

contracting muscles. Detailed analysis of the fine sampling peaks on the M2 and M5 reflections in the APS data indicated that the apparent period was ca. 820 ± 40 nm in the relaxed state, while it was ca. 1010 ± 40 nm in the contracting state. The estimated interference distances suggest that the perturbed regions of the crossbridge crown levels occupy the central part of a thick filament in a half of the sarcomere in the relaxed state and shift towards the Z-band in the contracting state. This finding was used for selecting the best-fit model of the crossbridge arrangement along the thick filaments (see figure 1).

To gain insight into the nature of these putative perturbed crossbridge crown arrangements along the thick filament in relaxed and contracting states, we simulated the intensities of the myosin-based meridional reflections by constructing one-dimensional models. The intensities of the meridional reflections from the models were calculated by varying the values of all parameters mentioned above. We started with a model having a regular region on either side of the perturbed region. Here the range of the centre-to-centre distance between the perturbed regions was restricted to be within the experimentally determined range given above. The most probable values of these parameters were determined by minimizing the R-factor between the calculated reflection intensities and the observed ones. Figure 2 compares the observed intensities of the meridional reflections with the calculated ones

turbulent regions are ca. 560-nm long having 13 triplet levels of the 42.9-nm repeat. There is both an inner (towards the M-line) and an outer (towards the Z-band) regular regions on either side of the perturbed regions. Their lengths are ca. 57 nm and ca. 86 nm, respectively. Thus the length of the perturbed region is much larger (ca. four times) than the total length of the regular region. In the contracting model, the perturbed regions become shorter by ca. 15% than that of the relaxed model; their length is ca. 480 nm in which 11 triplet levels of the 43.5-nm repeat are involved. The inner regular region increases in length to ca. 160 nm and the outer regular region shrinks to ca. 73 nm. The total length of the regular region becomes ca. 1.6 times longer in the contracting state than that in the relaxed state and the length of the perturbed region shrinks by ca. 15% in the contracting state. Thus the thick filament has a mixed structure of two different periodicities of the myosin crossbridge crown arrangement, and the perturbed region remains but with a slightly shorter length when muscle goes from the relaxed to the contracting state. The orientation of a two-headed myosin projection along the thick filament in the perturbed region is different from that in the regular region in both the relaxed and contracting models, generating the asymmetric profile of its projected density. The two heads of a crossbridge are flared axially in both states. Each pair of crossbridges in the two regions is closer to its neighbour in the contracting model than that in the

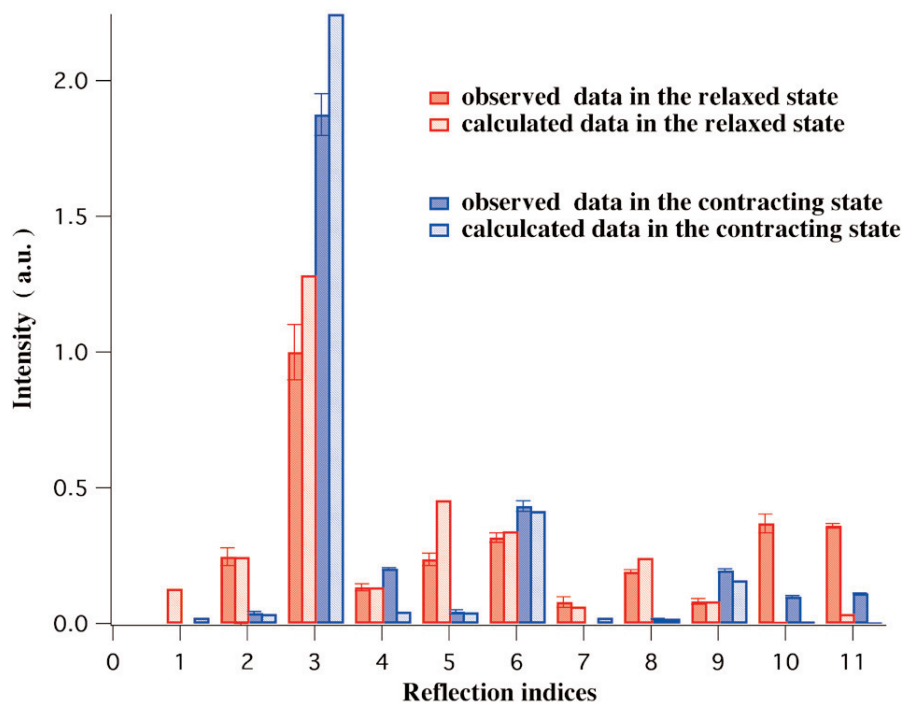


Figure 2: Comparisons of the calculated intensities from the best-fit models (slashed bar graphs) with the observed intensities (solid bar graphs) of the myosin-based meridional reflections with a 42.9-nm period in the relaxed state and a 43.5-nm period in the contracting state. These intensities are normalized so that the sum of the intensities from the second to the eleventh order reflections is same between relaxed and contracting states. Vertical lines on the solid bar graphs are standard deviation of the mean from four data sets.

from the model giving the lowest value of the R-factor (ca. 0.36); a fairly good agreement was obtained in both states.

The best fit to the experimental intensity data yielded a model for the crossbridge arrangement in relaxed and contracting states (Fig. 3). In the relaxed model, the per-

relaxed model. Thus the projected density of a two-headed myosin crossbridge in each region of the contracting model is sharper than that of a two-headed myosin crossbridge in each region of the relaxed model. The distances among the crowns of crossbridges in the perturbed region are 15.3 nm, 16.3 nm and 11.3 nm in the relaxed model and 15.5 nm, 14.5 nm and 13.5 nm in the contracting

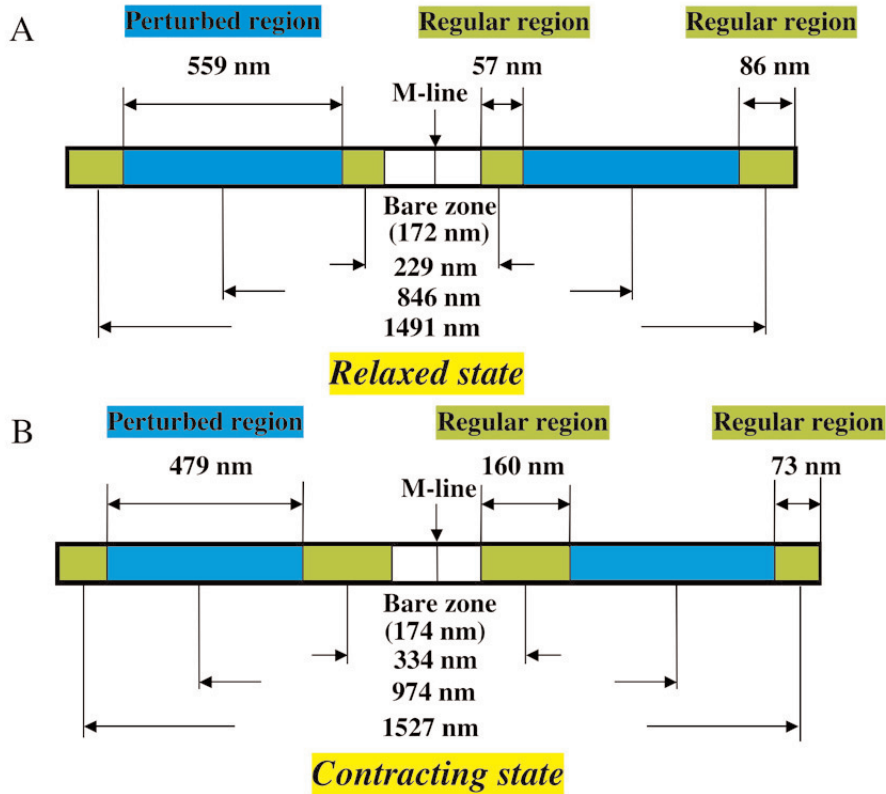


Figure 3: Distributions of the arrays of myosin crossbridge along the thick filament derived from the best-fit models. A, the relaxed state and B, the contracting state.

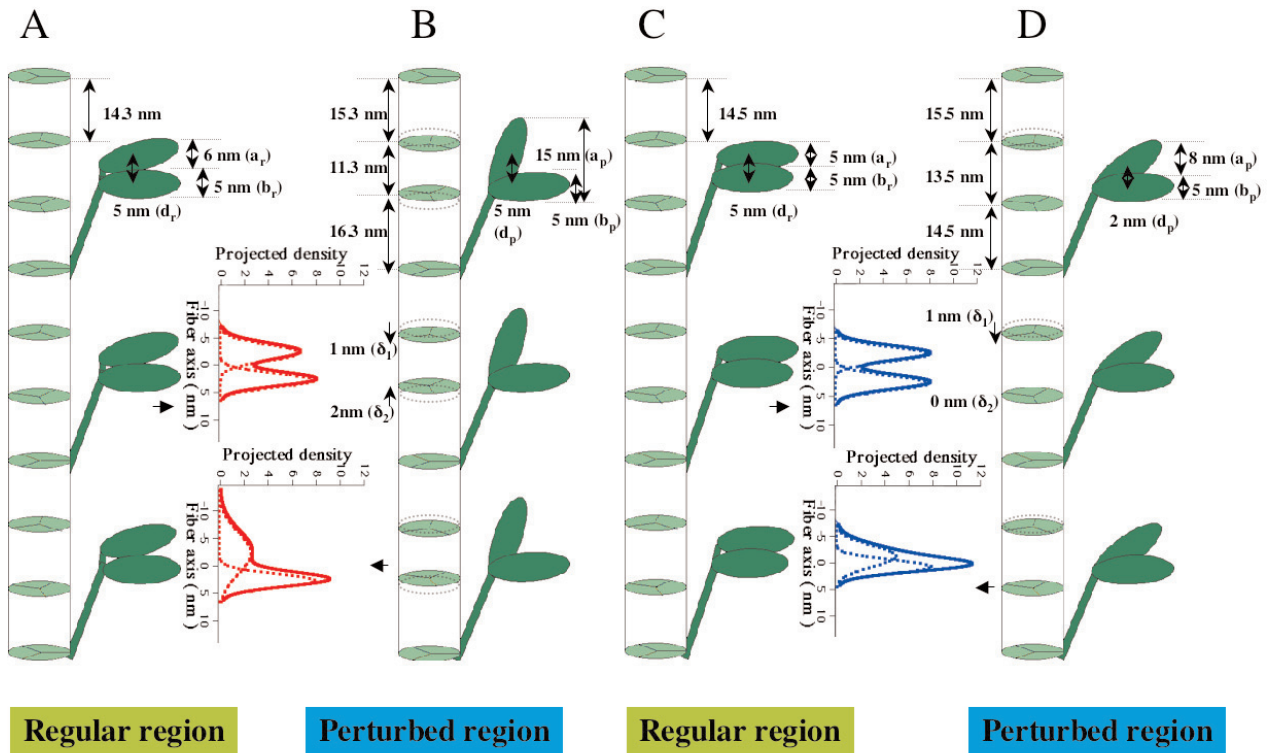


Figure 4: A schematic diagram of myosin crown periodicity and axial disposition of two-headed crossbridges along the thick filament in the regular and perturbed regions of the best-fit models. A, the regular region and B, the perturbed region in the relaxed state. C, the regular region and D, the perturbed region in the contracting state. Each crossbridge crown repeat in a triplet structure of the perturbed regions is shown along with the axial density profiles of a two-headed myosin crossbridge projected onto the fibre axis in the regular and perturbed regions (insets).

model (Fig. 4). The inter-crown distance in the regular region is 14.3 nm in the relaxed model and 14.5 nm in the contracting model. The deviation of each crown from the regular repeat becomes smaller in the contracting state than that in the relaxed state. Our modelling studies revealed a more precise conformation of the two-headed crossbridge in both states than those reported previously [3,4]. Although the number of parameters used in the modelling studies of Malinchik and Lednev [3] were much fewer than in our case, the number of the crossbridge levels in the perturbed region in their relaxed model was almost same as that in our model but their perturbed region shifted towards the M-line, lacking the

and/or C-protein.

In the present modelling studies, the best fit to the observed intensity data was made by allowing all eleven parameters to vary. In order to examine which parameters or parameter sets dominantly affect the intensities of myosin-based meridional reflections, we investigated the variation of the R-factor when variables of the best-fit relaxed model are substituted for those of the model that yielded the lowest R value of the contracting models (Fig. 5). Examination reveals that the value of the R-factor is primarily influenced by the crossbridge shifts from the regular repeat distance in the triplet region and the pro-

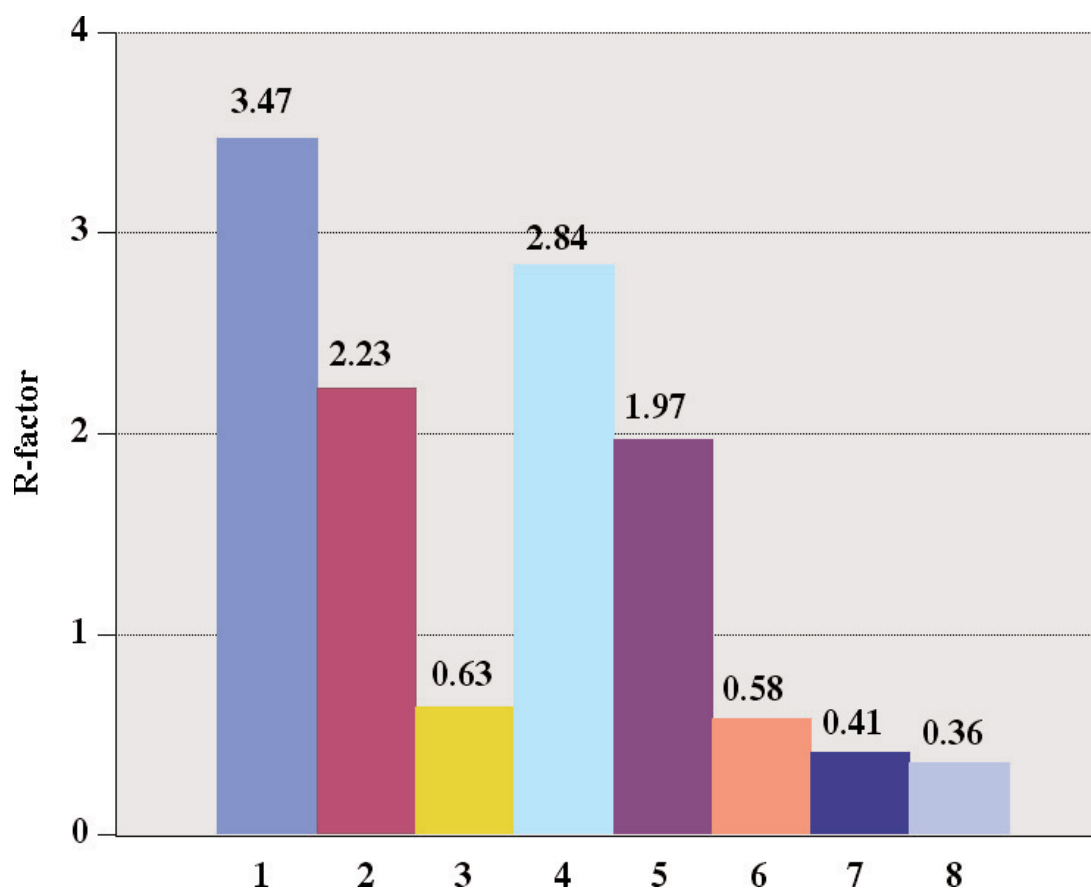


Figure 5: Changes of the value of R-factor in the contracting state when parameters or parameter sets of the best-fit model in the relaxed state were substituted for those of the model that yielded the lowest value of R-factor in the contracting state. 1; a relaxed parameter set, 2; the parameters of crossbridges (a_r , b_r , d_r , a_p , b_p , d_p) were substituted for the corresponding parameters of the contracting state, 3; the parameters of shifts from the regular repeat (δ_1 , δ_2) are substituted for those of the contracting state, 4; the parameters of the numbers of crossbridge levels (l , k) in both perturbed and regular regions are substituted for those of the contracting state, 5; the combination of 2 and 4, 6; the combination of 2 and 3, 7; the combination of 3 and 4, 8; a contracting parameter set.

inner regular region. The asymmetric profile of the projected density profile of a crossbridge in the perturbed region in the contracting model is consistent with the report of Juanhuix et al. [4] showing that each myosin head in the pair has a distinctly different axial orientation in the isometrically contracting state, although they did not distinguish their profiles in the perturbed and regular regions. The difference between the calculated intensities and the observed ones seen in M10 and M11 reflections in Fig. 2 may be attributed to the effects of the backbone

projected density profiles of a two-headed crossbridge in the singlet and triplet regions together with the lengths of both regions. More detailed examination will be reported elsewhere.

Conclusion

Our present findings show that the myosin filaments have a mixed structure with two different periodicities of crossbridges both in relaxed and contracting states; the

perturbed region is surrounded by two regular regions. The intensities of the meridional reflections that are not three-multiple orders are weakened in the contracting state by the fact that displacement of each crown repeat in the triplet structure shifts towards the regular distance and the densities of all crossbridges projected onto the fibre axis become sharper in the contracting model. Together, the length of the perturbed region becomes shorter in the contracting state than that in the relaxed state. These changes cause relative strengthening of the intensities of the 14.5 nm-based meridional reflections in the contracting state. Our modelling studies suggest that not only structural changes of two-headed myosin crossbridges but also changes of the inter-crown distances along the thick filament together with the length change of the perturbed region make significant contributions to the intensity change of the myosin-based meridional reflections when muscles go from a relaxed state to a contracting state. A full analysis and discussion of these findings will appear elsewhere.

Acknowledgements

The authors thank Drs. T. Kobayashi and H. Tanaka for their kind help with physiological and X-ray experiments at the Photon Factory and Dr. D. Gore for his help in setting the optics at the Advanced Photon Source. This work was approved by the Photon Factory Advisory Committee, and supported in part by the Special Coordination Funds from the Ministry of Education, Science, Sports and Culture of Japan. Use of the Advanced Photon Source was supported by the US Department of Energy, Basic Energy Sciences, Office of Energy Research, under Contract No. W-31-109-ENG-38. BioCAT is a NIH-supported Research Center (RR08630).

References

- [1] Holmes, K. C., Popp, D., Gebhard, W., and Kabsch, W. (1990) Atomic model of actin filament. *Nature*, 347, 44-49.
- [2] Lorentz, M., Poole, J. V., Popp, D., Rosenbaum, G., and Holmes, K. (1995) An atomic model of the unregulated thin filament obtained by x-ray fibre diffraction on oriented actin-tropomyosin gels. *J. Mol. Biol.*, 246, 108-119.
- [3] Malinchik, S. B., and Lednev, V. V. (1992) Interpretation of the x-ray diffraction pattern from relaxed skeletal muscle and modelling of the thick filament structure. *J. Muscle Res. Cell Motil.*, 13, 406-419.
- [4] Juanhuix, J., Bordas, J., Campmany, J., Svensson, A., Bassford, M. L., and Narayanan, T. (2001) Axial disposition of myosin heads in isometrically contracting muscles. *Biophys. J.*, 80, 1429-1441.
- [5] Stewart, M., and Kensler, W. (1986) Arrangement of myosin heads in relaxed thick filaments from frog skeletal muscle. *J. Mol. Biol.*, 192, 831-851.
- [6] Hashiba, S., Yasunaga, T., and Wakabayashi, T. (1999) Structure of native thick filaments revealed by cryo-electron microscopy and holographic image reconstruction technique. *Biophys. J.*, 76, Part 2, A32 (Abstr.), and cited by T. Wakabayashi in *Mechanisms of Biomolecular Motors*, Kyuoritsu Syuppan, Tokyo, pp.106-116 (1997) (in Japanese).
- [7] Huxley, H. E., and Brown, W. (1967) The low-angle x-ray diagram of vertebrate striated muscle and its behaviour during contraction and rigor. *J. Mol. Biol.*, 30, 383-434.
- [8] Yagi, N., O'Brien, E. J., and Matsubara, I. (1981) Changes of thick filament structure during contraction of frog striated muscle. *Biophys. J.*, 33, 121-138.
- [9] Squire, J. M. (1981) *The Structural Basis of Muscular Contraction*, Plenum Press, London, pp.344-362.
- [10] Haselgrove, J. C. (1975) X-ray evidence for conformational changes in the myosin filaments of vertebrate striated muscle. *J. Mol. Biol.*, 92, 113-114.
- [11] Linari, M., Piazzesi, G., Dobbie, I., Koubassova, N., Reconditi, M., Narayanan, T., Diat, O., Irving, M., and Lombardi, V. (2000) Interference fine structure and sarcomere length dependence of the axial x-ray pattern from active single muscle fibres. *Proc. Natl. Acad. Sci. USA*, 97, 7226-7231.
- [12] Oshima, K., Takezawa, Y., Sugimoto, Y., Kiyotoshi, M., and Wakabayashi, K. (2003) Modelling analysis of myosin-based meridional x-ray reflections from frog skeletal muscles in relaxed and contracting states. *Adv. Exp. Med. Biol.*, 538, 243-249.
- [13] Amemiya, Y., Wakabayashi, K., and Itoh, K. (1998) Renewal of the mirror system in the BL15A1 optics. *Photon Factory News*, 16, 9-10. (in Japanese).
- [14] Wakabayashi, K., Sugimoto, Y., Tanaka, H., Ueno, Y., Takezawa, Y., and Amemiya, Y. (1994) X-ray diffraction evidence for the extensibility of actin and myosin filaments during muscle contraction. *Biophys. J.*, 67, 2422-2435.
- [15] Irving, T. C., Fischetti, R. F., Rosenbaum, G., and Bunker, G. B. (2000) Fibre diffraction using the BioCAT undulator beamline at the Advanced Photon Source. *Nucl. Instrum. Methods*, A448, 250-254.
- [16] Fischetti, R., Stepanov, S., Rosenbaum, G., Barrea, R., Black, E., Gore, D., Heurich, R., Kondrashkina, E., Kropf, A.J., Wang, S., Zhang, K., Irving, T. C., and Bunker, G. B. (2004) The BioCAT undulator beamline 18ID: a facility for biological non-crystalline diffraction and x-ray

- absorption spectroscopy at the Advanced Photon Source. *J. Synchrotron Rad.*, 11, 399-405.
- [17] Phillips, W. C., Stewart, A., Stanton, M., Naday, I., and Ingersoll, C. (2002) High-sensitivity CCD-based x-ray detector. *J. Synchrotron Rad.*, 9, 36-43.
- [18] Wakabayashi, K., Namba, K., and Mitsui, T. (1984) Configurations of myosin heads in the crab striated muscle as studied by x-ray diffraction. *Adv. Exp. Med. Biol.*, 170, 237-250.
- [19] Squire, J. M., Harford, J. J., Edman, A. C., and Sjoström, M. (1982) Fine structure of the A-band in cryo-sections. III. Cross-bridge distribution and the axial structure of the human C-zone, *J. Mol. Biol.*, 155, 467-494.
- [20] Huxley, H. E. (2004) Fifty years of muscle and sliding filament hypothesis, *Eur. J. Biochem.*, 271, 1403-1415.

The interpretation of simultaneous small and wide-angle X-ray scattering data collected during quiescent crystallisation

S. Hanna

H.H. Wills Physics Laboratory, University of Bristol, Tyndall Avenue, Bristol, BS8 1TL

Abstract

Small and wide-angle X-ray scattering patterns have been calculated from randomly oriented stacks of lamellar crystals of isotactic polypropylene, at various stages during a hypothetical growth process. When the crystals have a small lateral width, it is possible to detect a long-period peak in the small-angle pattern when the crystalline wide-angle trace is too weak to be detected above the background noise. This finding has important implications for the interpretation of simultaneous small and wide-angle X-ray data collected during quiescent crystallization experiments. In particular, it challenges the suggestion that such measurements provide evidence for crystal growth through spinodal decomposition.

Keywords: SAXS; WAXS; Polymer Crystallisation; Spinodal Decomposition.

Introduction

Recently there has been considerable interest in studying the development of crystallinity in semi-crystalline polymers, using simultaneous measurements of small and wide-angle X-ray scattering (SAXS and WAXS) patterns. The value of such measurements lies in the fact that it is possible to relate changes in the local arrangements of chains within crystalline lamellae, to developments in the organisation of the lamellae within spherulites or other large scale structures. Performing the measurements simultaneously removes any ambiguity over the nucleation time of the crystallites being studied, allowing a straightforward comparison between the two sets of scattering data.

Simultaneous small and wide-angle measurements are now routine at a number of synchrotron X-ray sources around the world, and several studies of polymer crystallisation have been published [1-14]. A number of authors have noted that, during isothermal crystallisation of certain polymers from the melt, the small-angle patterns appear to develop peaks before there is any sign of crystalline scattering in the wide-angle region [10-13]. This observation has been interpreted by some as meaning that there are density fluctuations in the melt, prior to the formation of crystals. This, in turn, has been used as the basis for a new model of polymer crystallisation, based on the phenomenon of spinodal decomposition [12,15]. In the spinodal model, molten material is said to separate into regions with differing conformational disorder, and hence different densities. The denser regions, i.e. those with more conformational order, are then viewed as the places where crystal nucleation is most likely to occur.

The main aim of the present paper is to examine the experimental basis upon which the spinodal model was built. For this reason, the data of Terrill et al. (see Figure 2 of ref. [11]), which relate to the isothermal crystallisa-

tion of isotactic polypropylene (iPP), have been re-examined. It will be shown that, for stacks of crystals with small lateral width, it is possible to observe small-angle scattering, when the wide-angle scattering is below the threshold for observation. Thus the evidence for a spinodal model is far from secure.

Method

The lamellar stack model

The model chosen consists of a stack of growing crystalline lamellae of iPP (see Figure 1). It is assumed that the stack exists, *a priori*, on the grounds that such structures are found at the cores of spherulites of iPP and many other polymers, and thus occur at the earliest stages of crystallisation. No attempt is made to explain the origin of the lamellar stack. It is assumed that the lamellae all increase in width at the same linear rate, and that, at any point in time, all crystallites have the same dimensions. These assumptions may be regarded as highly idealised. However, they have been made in order to minimise the number of parameters in the model. The lamellar thickness, parallel to the chain axis, is assumed constant. Thus, the crystals only grow laterally. In addition, it is assumed

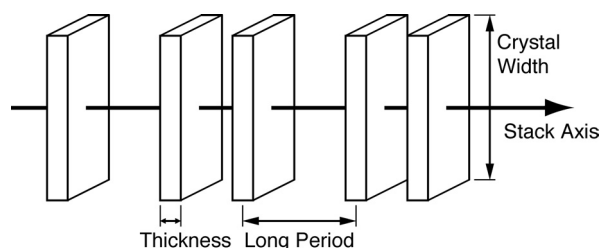


Figure 1: Schematic representation of the lamellar stack used as the basis of the diffraction calculations presented here. The lamellae have an approximately square cross section, and are of uniform thickness parallel to the stack axis. The widths of the lamellae are also uniform, and increase simultaneously and at the same rate.

that the lamellae are approximately square in cross-section perpendicular to the axis of the stack, and that there is no crystallographic register between the crystallites. The positions of the crystalline lamellae are represented by a 1-dimensional paracrystal, with nearest neighbour distribution governed by Gaussian statistics [16,17]. The merits of more sophisticated distribution functions have been discussed elsewhere [18,19].

The crystals are represented as parallelepipeds, with sides parallel to the unit cell axes **a**, **b** and **c**, and dimensions $L_a = N_a a$, $L_b = N_b b$ and $L_c = N_c c$. N_a , N_b and N_c are the numbers of unit cells parallel to **a**, **b** and **c** respectively, and must be integers for the following analysis to apply. The unit cell parameters for iPP were taken from ref. [20] to be $a = 6.65 \text{ \AA}$; $b = 20.96 \text{ \AA}$; $c = 6.50 \text{ \AA}$; $\alpha = \gamma = 90^\circ$ and $\beta = 99.33^\circ$. In the results presented below, N_c was taken to be 20 unit cells, and the ratio of $N_a = 3N_b$ was maintained so that $L_a \approx L_b$. N_b was varied between 1 and 20 unit cells, corresponding to a variation in crystal width between *ca.* 20Å and *ca.* 400Å.

The scattered X-ray intensities were calculated from first principles and normalised by the number of lamellae in the stack, in order to ensure that the calculated values were directly comparable between small and wide-angle regions. However, the intensity units quoted are not absolute, because no account was taken of the number of lamellar stacks per unit volume. Further, in order to ensure comparability with experiment, additional geometric correction factors were applied.

Wide-angle scattering calculation

The wide angle scattering from a single lamella was obtained by explicitly summing the scattered amplitudes from all of the unit cells in the crystal [21]. The resulting expression was multiplied by its complex conjugate and averaged over all polarisations of the incident radiation to give:

$$I_{Lamella}(\mathbf{s}) = I_e F(\mathbf{s}) F^*(\mathbf{s}) \frac{\sin^2(\pi N_a \mathbf{s} \cdot \mathbf{a})}{\sin^2(\pi \mathbf{s} \cdot \mathbf{a})} \cdot \frac{\sin^2(\pi N_b \mathbf{s} \cdot \mathbf{b})}{\sin^2(\pi \mathbf{s} \cdot \mathbf{b})} \cdot \frac{\sin^2(\pi N_c \mathbf{s} \cdot \mathbf{c})}{\sin^2(\pi \mathbf{s} \cdot \mathbf{c})} \exp(-B s^2/2) \quad (1)$$

where **s** is the scattering vector, related to the scattering angle by $s = (2/\lambda)\sin \theta$, and I_e is the classical scattering from a single electron, which decays as the inverse square of the distance from the sample to the detector. This relationship is of importance when comparing the intensities measured by the small and wide-angle detectors, which are normally at quite different distances. $F(\mathbf{s})$ is the structure factor for a particular scattering vector, calculated from atomic coordinates for iPP, assuming the *Cc* space group [20]. The exponential factor in equation (1) is a temperature factor which accounts for thermal motion. At room temperature, an appropriate value for B is 8.5 \AA^2 [20]. However, at 145°C , which is the temperature of the study being considered, B may be modified to 11.9 \AA^2 , using a harmonic approximation. The overall reduction in intensity as a result of this increase in temperature is

around 6% for the main Bragg reflections.

In order to simulate unoriented or powder diffraction data, the diffracted intensity was integrated over all possible orientations, giving, for a stack of N independent lamellae:

$$I_{WAXS}(\mathbf{s}) = \frac{N}{4\pi} \int_0^{2\pi} d\Phi \int_0^\pi \sin \Theta d\Theta \cdot I_{Lamella}(\mathbf{s}) L_{WAXS} \quad (2)$$

The integration in equation (2) was carried out numerically. It should be noted that the intensity given by equation (2) represents the X-ray flux per unit area of the diffraction circle, and implicitly includes the same Lorentz factor that occurs in a powder diffractometer experiment, thus allowing a direct comparison with the experimental data without further correction. The extra factor, L_{WAXS} , takes into account the geometry and sensitivity of the detector, and will be discussed in more detail below.

The amorphous contribution to the wide-angle scattering was not calculated. Instead, the experimental amorphous background was fitted approximately using an analytical function, which was then added to the intensities shown in the results section. No account was taken of crystalline defects in calculating the wide-angle scattering patterns. Since lattice disorder would be expected to broaden and weaken the crystalline reflections, the results presented here should be considered to provide an upper bound on the expected wide-angle peak intensities.

Small-angle scattering calculation

The form factor of a single lamella is given by:

$$I_{Form}(\mathbf{s}) = I_e (n_e V \Delta\rho)^2 \frac{\sin^2(\pi N_a \mathbf{s} \cdot \mathbf{a})}{(\pi N_a \mathbf{s} \cdot \mathbf{a})^2} \cdot \frac{\sin^2(\pi N_b \mathbf{s} \cdot \mathbf{b})}{(\pi N_b \mathbf{s} \cdot \mathbf{b})^2} \cdot \frac{\sin^2(\pi N_c \mathbf{s} \cdot \mathbf{c})}{(\pi N_c \mathbf{s} \cdot \mathbf{c})^2} \quad (3)$$

where V is the volume of a crystal, n_e is the number of electrons per unit volume of the crystal and $\Delta\rho$ is the fractional difference in density between the crystal and the amorphous matrix. At 145°C , which is the temperature of interest here, the literature value of $\Delta\rho$ is *ca.* 0.15 [22].

The lamellar stack was modelled using a 1-dimensional paracrystal to represent the positions of the centres of mass of the crystals. A Gaussian distance distribution function was employed, with a mean crystal separation $\bar{z} = 200 \text{ \AA}$ and standard deviations $\sigma = 10, 20$ and 40 \AA . Results were compared from both infinite and finite stacks. For an infinite stack, with N lamellae per unit length, the scattering is given by [16,17]:

$$I_{Stack}(\mathbf{s}) = N I_{Form}(\mathbf{s}) \cdot \Re \left(\frac{1 + H(Z)}{1 - H(Z)} \right) \quad (4)$$

where $H(Z)$ is the Fourier transform of the nearest neighbour distribution function, and Z is the component of **s** taken along the stack axis, which is taken to coincide with

the crystallographic c axis. For a finite stack of N lamellae, the scattered intensity may be written as:

$$I_{Stack}(\mathbf{s}) = NI_{Form}(\mathbf{s}) \cdot P(Z) \quad (5)$$

in which $P(Z)$ is given by:

$$P(Z) = 1 + 2 \sum_{j=1}^{N-1} \frac{(N-j)}{N} \exp[-2j(\pi\sigma Z)^2] \cos(2\pi jZz) \quad (6)$$

As for the wide-angle calculation, the diffracted small-angle intensity was integrated over all possible orientations, to give:

$$I_{SAXS}(\mathbf{s}) = \frac{1}{4\pi} \int_0^{2\pi} \int_0^{\pi} \sin\Theta d\Theta \cdot I_{Stack}(\mathbf{s}) L_{SAXS}(2\theta) \quad (7)$$

L_{SAXS} is a machine dependant correction factor, and the integration in equation (7) was performed numerically.

Machine dependent correction factors

Before it is possible to compare the calculated traces for the small and wide-angle regions of the diffraction patterns, it is necessary to correct for the detector geometry employed. The data of ref. [11] were collected at the simultaneous SAXS/WAXS facility at Daresbury. The wide-angle data were collected using a curved Inel 1-dimensional position sensitive detector, 0.3m from the sample, and the small-angle data collection used a quadrant detector at a distance of 3.5m. The resolutions of the two detectors are nominally 0.1° for the Inel detector and $250 \mu\text{m}$ for the quadrant detector. It is assumed that the resolutions can be used to define the active areas of each channel of the detectors. The correction factors consist of the product of the active area in each case, with an attenuation factor:

$$\begin{aligned} L_{WAXS} &= \left(0.1^\circ \times \frac{\pi}{180^\circ}\right) \times lr \times A_W \\ L_{SAXS} &= (250\mu\text{m}) \times \frac{2\pi r \sin 2\theta}{4} \times A_S \end{aligned} \quad (8)$$

in which l is the aperture of the Inel detector perpendicular to the knife-edge, and A_W and A_S are the relevant attenuation factors, required to avoid saturating the detectors. Typical values for these parameters are $l = 5\text{mm}$ [23] and $A_W = 0.4 A_S$ [24]. r is the sample-detector distance relevant to each detector. It is also assumed that the quantum efficiencies of the two detectors are the same.

Results

Figure 2 shows SAXS and WAXS patterns calculated for infinite stacks of iPP lamellae at 145°C , for nominal crystal widths ranging between 20 and 400\AA , using $\bar{z} = 200\text{\AA}$ and $\sigma = 20\text{\AA}$. The crystal widths indicated on the graphs are nominal, since the actual widths must be an integral number of unit cells. The most striking feature observed is that the small-angle peak, at $s \sim 0.005\text{\AA}^{-1}$ is much more intense than the main Bragg reflections in the

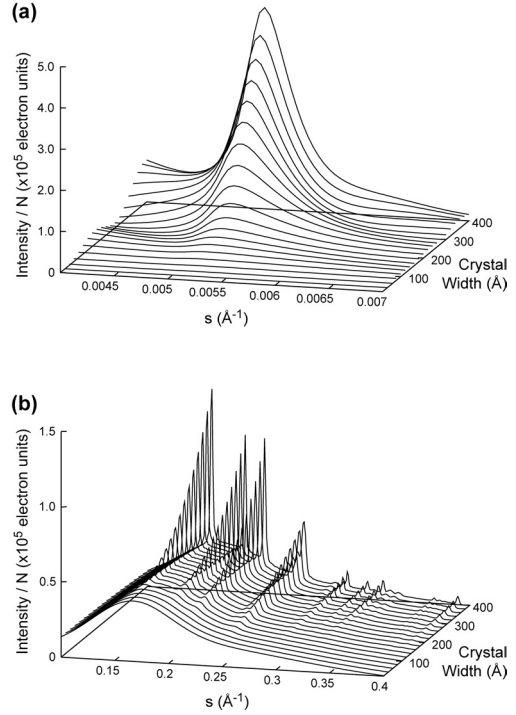


Figure 2: Calculated (a) SAXS and (b) WAXS patterns for infinite stacks of iPP lamellae at 145°C , for nominal crystal widths between 20 and 400\AA , using $\bar{z} = 200\text{\AA}$ and $\sigma = 20\text{\AA}$. The intensities are given as multiples of the scattering expected from a single electron (electron units), and are normalised by the number of lamellae per unit length of the stack, N . ($s = (2/\lambda)\sin\theta$).

wide-angle trace. In fact, for this particular model, the small-angle peak is *ca.* 5 times more intense than the wide-angle-peaks, for a given crystal width. This result can be seen more clearly in Figure 3, in which the intensities of the small and wide angle peaks are compared as a function of nominal crystal width.

The large disparity in the peak intensities raises the question of whether it is possible for the small-angle peak to be visible when the wide-angle peaks are not. The visibility of the peaks will depend on a combination of the sensitivity of the X-ray detector and the X-ray counting statistics. If it is assumed that the small and wide-angle detectors have the same sensitivity, it is clear from Figure 3 that the wide-angle peaks will not be visible until some time after the small-angle peak has appeared. For example, if the horizontal dotted line in Figure 3 represents an arbitrary threshold, in this case 4×10^3 electron units, above which the peaks may be detected, then it can be seen that the SAXS peak will become visible at a crystal width of $\sim 70\text{\AA}$, while the (110) reflection will not be visible until $\sim 120\text{\AA}$, as indicated by the arrows labelled (1) and (2) respectively.

Poor X-ray counting statistics will also affect the wide-angle traces more than the small-angle ones. This is partly because of the lower absolute intensity of the wide-angle trace, but mainly because the crystalline reflections

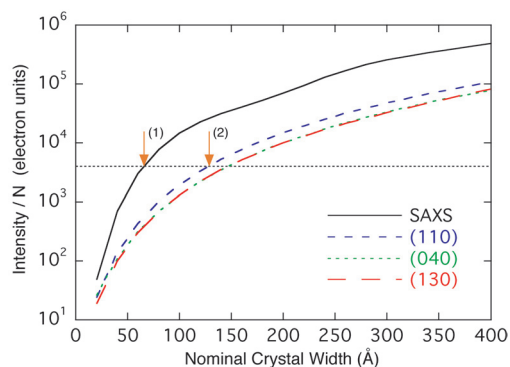


Figure 3: Semi-log plot showing the variation in intensities of the small-angle peak, and the principal wide-angle reflections in Figure 2, with nominal crystal width. The value taken for the small-angle intensity is the maximum value of the small-angle peak. The horizontal dotted line indicates how, for a given detection limit, the small-angle peak will be detected before the Bragg peaks are visible. Arrows (1) and (2) are referred to in the text.

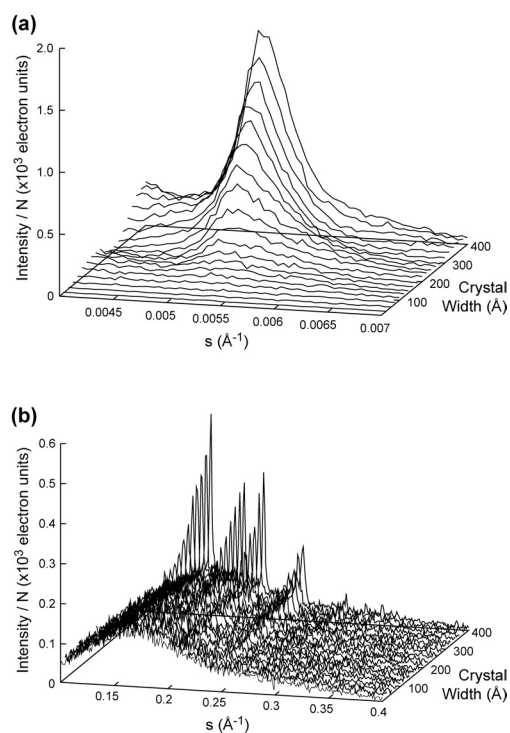


Figure 4: Calculated (a) SAXS and (b) WAXS patterns for the same model as in Figure 2. The intensities have been scaled and Poisson noise has been added, as described in the text ($s = (2/\lambda)\sin \theta$).

are superimposed on a substantial amorphous halo. This means that, when the crystalline reflections are weak i.e. at early crystallisation times, they may be lost in the noise resulting from the amorphous background. This effect is demonstrated in Figure 4, where the scattering curves from Figure 2 have been scaled by a constant amount and random Poisson noise has been added. The amount of scaling was chosen in order to get an approximate match in noise levels between Figure 4 and the published traces. It is clear from Figure 4, that the visibility of the wide-

angle peaks is profoundly affected by the amount of background noise present, whereas the small-angle peak, by virtue of its greater intensity and larger signal-to-noise ratio, is still clearly apparent. In the results shown, the small-angle peak is visible from crystal widths of $\sim 100\text{\AA}$, while the wide-angle peaks are not visible until the crystal width reaches $\sim 200\text{\AA}$.

Discussion

Model Predictions

From the results shown in Figures 2,3 and 4, it is clear that the simple lamellar stack model presented here is capable of producing qualitatively similar behaviour to that observed experimentally. The main observation, that the SAXS intensity is much greater than the WAXS intensity, leads to the conclusion that, as a consequence of the relative signal-to-noise ratios, there will be situations in which the SAXS peak is observable where the WAXS peaks are not. This conclusion is consistent with the data of Terrill et al. (Figure 2 of ref. [11]), which, indeed, shows that the wide-angle traces are noisier, and hence of lower intensity, than the small-angle ones. Thus, it appears that the experimental data *may* be accounted for by a conventional model of stacks of lamellae, and that it is not necessary to invoke a model of spinodal decomposition in order to explain the observations. This point will be discussed further below.

It is, in fact, a common observation in published simultaneous SAXS/WAXS experiments that the wide-angle data are noisier, than the corresponding small-angle data (*e.g.* see refs. [3,11,13,25]). This finding must, in part, be due to the types of detector in use. For example, Hsiao and coworkers [25] have studied the sensitivity of the wide-angle detector on the X27C beamline at Brookhaven National Laboratory, using model alkane systems, and have concluded that the lower limit of detection in this case is 0.56% crystallinity. These workers have also reported data similar to ref. [11] for iPP.

Model Deficiencies

It would be wrong to claim that the lamellar stack model presented here can provide an exact match to the experimental data. The model has several deficiencies, and is certainly not correct in detail. The main criticism of the lamellar stack model must be that it is too ideal. It has been assumed that the crystals have sharp edges, are all the same size and grow at exactly the same rate. In reality, the crystals would be expected to vary both in thickness and in width, and there should be a more diffuse boundary between the crystalline and amorphous phases. These factors would lead to changes in the form of equations (3) and (4) which would affect the small-angle peak height and width. Also, the calculated SAXS profiles are narrower than those of ref. [11], which is a consequence of the choice of interlamellar distance distribution function. More sophisticated models for infinite paracrystalline stacks have been discussed at length by several

other authors [18,19,26-30] and it is clear that there is scope for considerable modification to both the width and the overall shape of the small-angle peak. The most likely outcome of any such refinement to the model would be to broaden the peak and slightly diminish its intensity.

The results shown in *Figures 2 to 4* were based on the assumption that the stack of crystals was of infinite extent. However, inspection of electron micrographs suggests that a stack of between 5 and 10 lamellae would be more appropriate. The effect of stack size on the small-angle peak intensity is illustrated in *Figure 5*. For a given variation in interlamellar spacing ($\sigma = 20\text{\AA}$) the peak intensity falls by about one third and the width increases by about 50% on reducing the size of the stack to $N=5$. A smaller change is observed for $N=10$. The peak shape is also sensitive to variations in σ , and it can be seen, that small decreases in σ can lead to significant increases in the peak height. Thus finite and infinite stack models produce similar predictions for the small-angle peak intensity, with the exact intensity and peak shape being sensitive to the choice of N and σ . Any realistic model should include a distribution of stacks with different values for N , σ and z , as was invoked to explain the SAXS data from polyethylene [31].

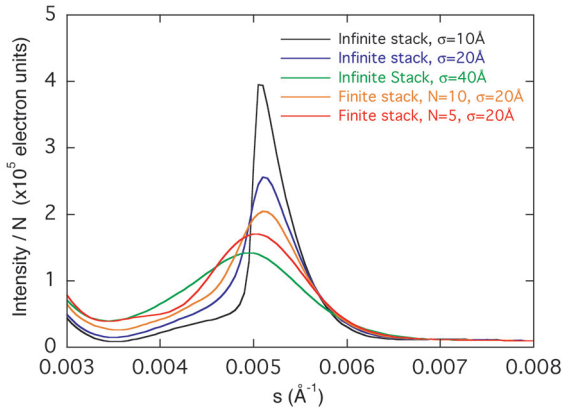


Figure 5: Small-angle peak profiles for several different lamellar stack models. In all cases, the mean interlamellar spacing, z , is 200\AA , and the crystal width is nominally 300\AA .

Other deficiencies in the model, include the lack of lattice distortions, mosaic structure and other forms of disorder, which would broaden and weaken the wide-angle peaks without affecting the small-angle peaks, and uncertainties over the exact sensitivities and quantum efficiencies of the detectors used experimentally.

Spinodal Analysis

Although the intensities shown in *Figure 2a* were generated on the assumption of a uniformly growing lamellar stack, it is interesting, nevertheless, to analyse them as if they resulted from a Cahn-Hilliard model of spinodal decomposition [32,33]. The Cahn-Hilliard analysis consists, essentially, of looking for a peak in the graph of $R(s)$

versus s , in which $R(s)$ is the growth rate of the logarithm of the scattered intensity:

$$R(s) = \frac{d \log_e I_{Stack}(s,t)}{dt} \quad (9)$$

It is interesting to consider whether the present model could produce such a maximum.

The discussion will be limited, initially, to the intensity distribution along the crystallographic c^* axis. In this case, we may write, in place of equation (5):

$$I_{Stack}(s,t) = const. \times V^2(t) \times G(s) \quad (10)$$

where:

$$G(s) = \frac{\sin^2(\pi N_c \mathbf{s} \cdot \mathbf{c})}{(\pi N_c \mathbf{s} \cdot \mathbf{c})^2} \cdot P(Z) \quad (11)$$

and $V(t)$ is the time-varying volume of crystals. Taking logarithms, we have:

$$\log_e I_{Stack}(s,t) = const. + 2 \log_e V(t) + \log_e G(s) \quad (12)$$

from which it is clear that the growth rate will be independent of s , irrespective of the crystal growth kinetics. The separation of variables in equation (12) occurs because the form factor, $G(s)$, is independent of time. This is only true along the c^* axis: in other regions of reciprocal space, we have an additional factor due to the crystal width, of:

$$\frac{\sin^2(\pi N_a \mathbf{s} \cdot \mathbf{a})}{(\pi N_a \mathbf{s} \cdot \mathbf{a})^2} \times \frac{\sin^2(\pi N_b \mathbf{s} \cdot \mathbf{b})}{(\pi N_b \mathbf{s} \cdot \mathbf{b})^2} \quad (13)$$

in which N_a and N_b both increase with time. However, the process of orientational averaging leads only to a weak dependence of growth rate on s , as shown in *Figure 6*. In the figure, it is assumed that N_a and N_b increase linearly with time, and $R(s)$ is calculated by performing a least squares fit to the scattered intensities from the earliest part of the growth process (*i.e.* from 20 to 100\AA). For a spinodal process we would expect the peak to be considerably more obvious.

It would appear that the only way to obtain a true maximum in $R(s)$ is if the form of the small angle scattering factor, $G(s)$, changes during the initial development of the stack. This could result for example from changes in the thickness, or density, as the lamellae are initially established. Indeed there have been several recent studies which have followed the development of the crystalline morphology in polyethylene from isolated lamellae to well defined stacks [34-37]. However, such refinements would be difficult to include in the current model in anything other than an *ad hoc* manner, and will not be considered further here.

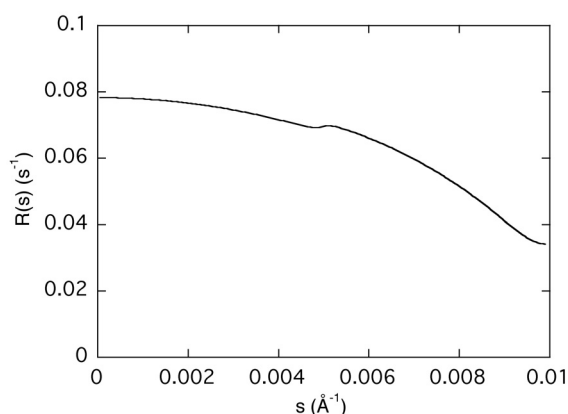


Figure 6: Plot of $R(s)$ versus s for an infinite lamellar stack, with $z = 200\text{\AA}$ and $\sigma = 20\text{\AA}$, with $R(s)$ calculated over the interval from crystal widths of 20 to 100\AA .

Thus the model, as presented, is able to reproduce the key feature of the experimental data i.e. the presence of a small-angle peak in the absence of wide-angle peaks, but cannot explain the experimental growth kinetics without further development.

Conclusions

X-ray scattering calculations have been performed, based on a simple model of a stack of growing crystalline lamellae of iPP. The model indicates that it is possible to observe the main interlamellar peak in the small-angle scattering pattern at early times in the crystal growth, when the wide-angle crystalline reflections are too weak to be observed over the background noise. The model can therefore explain the lack of crystalline reflections in experimental data from quiescent crystallisation studies of iPP, without the need to invoke spinodal decomposition. However, the uniformly growing lamellar stack model, as presented here, is too simplistic to reproduce the early-stage growth kinetics reported by Ryan and coworkers [10-12]. A more complete model would need to consider the initial stages of the development of order in growing crystals in more detail.

Acknowledgements

This paper was based on an oral contribution delivered at the 12th Annual CCP13 Fibre Diffraction and Non-Crystalline Diffraction Workshop in Cambridge, July 2003. The author would like to thank Dr. Peter Barham for initially suggesting the analysis described in this paper, and for providing electron micrographs and crystallisation data from isotactic polypropylene. He would also like to thank Drs. W. Bras, J.K. Hobbs, P.D. Olmsted and N.J. Terrill, and Profs. D.J. Blundell, J.S. Higgins and A.J. Ryan for several stimulating discussions during the preparation of this paper.

References

- [1] Laggner, P. and Mio, H. Nucl. Instrum. Meth. Phys. Res. (1992), A323, 86-90.
- [2] Bras, W., Derbyshire, G.E., Ryan, A.J., Mant, G.R., Felton, A., Lewis, R.A., Hall, C.J. and Greaves, G.N. Nuc. Inst. Meth. Phys. Res. (1993), A326, 587-591.
- [3] Zachmann, H.G. and Wutz, C. in Crystallisation of Polymers M. Dosière Ed., NATO ASI-C series on Mathematical and Physical Sciences, Vol. 405, (Kluwer, Dordrecht, Netherlands) (1993), pp.559-564.
- [4] Ryan, A.J., Naylor, S., Komanschek, B., Bras, W., Mant, G.R. and Derbyshire, G.E. ACS Symposium Series, (1994), 581, 162-180.
- [5] Haswell, R., Van Mechelen, J.B., Mensch, C.T.J. and De Groot, H. Nucl. Instrum. Meth. Phys. Res. (1995), B97, 242-247.
- [6] Ezquerro, T.A., López-Cabarcos, E., Hsiao, B.S. and Baltà-Calleja, F.J. Phys. Rev. E, (1996), 54, 989-992.
- [7] Hamley, I.W., Fairclough, J.P.A., Ryan, A.J., Bates, F.S. and Towns-Andrews, E. Polymer, (1996), 37, 4425-4429.
- [8] Fougnes, C., Damman, P., Villers, D., Dosiere, M. and Koch, M.H.J. Macromolecules, (1997), 30, 1385-1391.
- [9] Rueda, D.R., Gutierrez, M.C.G., Ania, F., Zolotukhin, M.G. and Baltà-Calleja, F.J. Macromolecules, (1998), 31, 8201-8208.
- [10] Ryan, A.J., Terrill, N.J. and Fairclough, J.P.A. ACS PMSE Prep. (1998), 79, 358-359.
- [11] Terrill, N.J., Fairclough, P.A., Towns-Andrews, E., Komanschek, B.U., Young, R.J. and Ryan, A.J. Polymer (1998), 39, 2381-2385.
- [12] Ryan, A.J., Fairclough, J.P.A., Terrill, N.J., Olmsted, P.D. and Poon, W.C.K. Faraday Discuss. (1999), 112, 13-29.
- [13] Hsiao, B.S., Wang, Z., Yeh, F., Gao, Y. and Sheth, K.C. Polymer (1999), 40, 3515-3523.
- [14] Lefebvre, X., Koch, M.H.J., Reynaers, H. and David, C. J. Polym. Sci. B - Polym. Phys., (1999), 37, 1-18.
- [15] Olmsted, P.D., Poon, W.C.K., McLeish, T.C.B., Terrill, N.J. and Ryan, A.J. Phys. Rev. Lett., (1998), 81, 373.
- [16] Vonk, C.G. in Small Angle X-ray Scattering, O. Glatter, & O. Kratky Eds. (Academic Press, London) (1982), pp433-466.
- [17] Hosemann, R. and Bagchi, S.N. Direct Analysis of Diffraction by Matter (North Holland, Amsterdam) (1962), pp408-420.
- [18] Crist, B. J. Polym. Sci.: Polym. Phys. Ed. (1973), 11, 635-661.
- [19] Crist, B. and Morosoff, N. J. Polym. Sci.: Polym. Phys. Ed. (1973), 11, 1023-1045.
- [20] Natta, G. and Corradini, P. Nuovo Cimento Suppl. (1960), 15, 40.

- [21] Warren, B.E. X-ray Diffraction (Addison-Wesley, Massachusetts) (1969), pp27-30.
- [22] Albrecht, T. and Strobl, G. *Macromolecules* (1995), 28, 5267-5273.
- [23] Bras, W. Private communication (1999).
- [24] Terrill, N.J. Private communication (1999).
- [25] Wang, Z., Hsiao, B.S., Kopp, C., Sirota, E.B., Agarwal, P. and Srinivas, S. *ACS PMSE Prep.* (1999), 81, 355-356.
- [26] Hall, I.H. and Toy, M. in *Structure of Crystalline Polymers* edited by I.H. Hall (Elsevier Applied Science Publishers, London) (1984), pp181-228.
- [27] Blundell, D.J. *Acta Cryst.* (1970), A26, 472-476.
- [28] Blundell, D.J. *Acta Cryst.* (1970), A26, 476-483.
- [29] Ruland, W. *Colloid and Polym. Sci.* (1977), 255, 417-427.
- [30] Blundell, D.J. *Polymer* (1978), 19, 1258-1266.
- [31] Strobl, G. and Müller, N. *J. Polym. Sci.: Polym. Phys. Ed.* (1973), 11, 1219-1233.
- [32] Cahn, J.W. and Hilliard, J.E. *J. Chem. Phys.* (1958), 28, 258.
- [33] Cahn, J.W. *J. Chem. Phys.* (1965), 42, 93-99.
- [34] Tashiro, K., Sasaki, S. and Kobayashi, M. *Macromolecules* (1996), 29, 7460.
- [35] Tashiro, K., Sasaki, S. and Kobayashi, M. *Polym. J.* (1998), 30, 485.
- [36] Sasaki, S., Tashiro, K., Kobayashi, M., Izumi, Y. and Kobayashi, K. *Polymer* (1999), 40, 7125-7135.
- [37] Akpalu, Y.A. and Amis, E.J. *J. Chem. Phys.* (1999), 111, 8686-8695.

Flexible Filamentous Virus Structures from Fiber Diffraction

Gerald Stubbs, Lauren Parker, Justin Junn and Amy Kendall

Center for Structural Biology, Vanderbilt University, Nashville, TN 37232-8725, USA

Abstract

A combination of orientation using strong magnetic fields and the use of highly collimated synchrotron radiation has allowed the determination of the symmetry, surface structural features, and radial density distribution for potato virus X. A diffraction pattern from the related narcissus mosaic virus promises significantly more accurate determination of the radial density distribution. Diffraction patterns from the potyviruses wheat streak mosaic virus and bean common mosaic virus offer, for the first time, the possibility of similar determinations for potyviruses, economically the most important plant viruses in the world.

Filamentous plant viruses

Filamentous plant viruses have been the object of fiber diffraction studies since the 1930s. Bernal and Fankuchen (1941) published diffraction patterns from oriented sols of a number of viruses, including the rigid rod-shaped tobacco mosaic virus (TMV) and the flexible filamentous potato virus X (PVX).

TMV and related viruses (tobamoviruses) were studied extensively in the following years. The symmetry was determined from fiber diffraction patterns using an isomorphous mercury derivative (Franklin & Holmes, 1958), and found to be 49 subunits in three turns of the viral helix. The viruses were shown to be about 180 Å in diameter and to have a central hole of diameter 40 Å. A single strand of RNA follows the basic viral helix at a radius of about 40 Å (Caspar, 1956; Franklin, 1956a).

Isomorphous replacement was used by Barrett et al. (1972) to obtain an electron density map of TMV from fiber diffraction data at 10 Å resolution. The structure was determined at 4 Å resolution (Stubbs et al., 1977) using the technique of multi-dimensional isomorphous replacement (Stubbs & Diamond, 1975). This determination required six isomorphous heavy-atom derivatives. Further advances in data processing (Makowski, 1978), phasing (Stubbs & Makowski, 1982) and refinement (Stubbs et al., 1986) methods allowed the structure determination at 3.6 Å resolution (Namba & Stubbs, 1986), and eventually phase extension and refinement at 2.9 Å (Namba et al., 1989). The entire protein chain and the RNA were visible in the 2.9 Å map. Interpretation of the maps was aided by parallel studies by Klug's group on crystals of the isolated TMV coat protein, which led to an independent structure of a large part of the protein without RNA (Bloomer et al., 1978).

Other tobamoviruses had also interested the early workers; radial density distributions were determined for the U2 strain of TMV, cucumber virus 4, and the so-called "bean form" of the Nigerian cowpea strain of TMV, later

called sunn-hemp mosaic virus (Franklin, 1956b; Holmes & Franklin, 1958). The structure of U2 was later determined by molecular replacement from TMV using fiber diffraction data at 3.5 Å resolution (Pattanayek & Stubbs, 1992), cucumber green mottle mosaic virus at 3.4 Å using a combination of isomorphous replacement and molecular replacement (Lobert & Stubbs, 1990; Wang & Stubbs, 1994), odontoglossum ringspot virus at 3.5 Å by molecular replacement (Planchart, 1995; Wang et al., 1998), and ribgrass mosaic virus (RMV) at 2.9 Å by molecular replacement (Wang et al., 1997). These four virus structures were all refined using the molecular dynamics refinement program F-XPLOR (Wang & Stubbs, 1993), so although the TMV data are probably the best tobamovirus fiber diffraction data available, the RMV structure is probably the best determined structure.

Despite the early work of Bernal and Fankuchen, many years were to elapse before significant progress could be made with fiber diffraction from the flexible filamentous potyviruses. Beginning in the 1960s, Tollin, Wilson, and their colleagues determined helical pitch values and symmetries for PVX, narcissus mosaic virus (NMV), white clover mosaic virus, papaya mosaic virus, and clover yellow mosaic virus (reviewed by Tollin and Wilson, 1985). These studies used diffraction from dried fibers of the viruses, supplemented by electron microscopic observations. Magnetically oriented sols (Yamashita et al., 1998) of potyviruses yielded dramatically improved diffraction patterns, however, and these patterns allowed Parker et al. (2002) to determine the symmetry of PVX with considerably more accuracy, and to construct a low-resolution model whose features included deep grooves running both longitudinally and azimuthally in the viral outer surface.

There have been very limited studies of the rigid tobamoviruses (Finch, 1965; Tollin & Wilson, 1971) and hordeiviruses (Finch, 1965), largely confined to determinations of the helical repeat and partial symmetry determinations.

Potyvirus make up the largest and most economically important plant virus group, including almost a third of the known plant viruses and responsible for over half the viral crop damage in the world (Riechmann et al., 1992; López-Moya and García, 1999). Nevertheless, structural studies of these viruses have been extremely limited, and published reports are in fact confined to estimates of the helical pitch (about 33 Å) based on the observation of a single reflection in optical diffraction patterns from electron micrographs (Varma et al., 1968; McDonald and Bancroft, 1977).

Specimen preparation

Fiber diffraction specimens were either oriented sols or dried fibers.

Oriented sols were made by an extension of the method of Gregory and Holmes (1965). Soft centrifuged virus pellets were drawn into glass capillaries and moved back and

mg/ml virus solution in a 1 mm gap between the ends of a re-moulded paper clip. Drying was controlled by maintaining a constant relative humidity of 86% in equilibrium with a saturated solution of potassium chloride. In later experiments, copper wire was used in order to allow drying in the magnetic field.

Diffraction data

Preliminary diffraction data were collected using an R-AXIS IV image plate detector and a Rigaku RU200 rotating anode X-ray generator equipped with a 100 µm source. Synchrotron data were collected at the BioCAT beam line of the Advanced Photon Source synchrotron at Argonne National Laboratory. The beam had dimensions of 35 µm vertically and 60 µm horizontally at the detector, and because of the long focal length of the mirrors, was very close to this size at the specimen. Data were recorded using a CCD detector approximately 115 mm

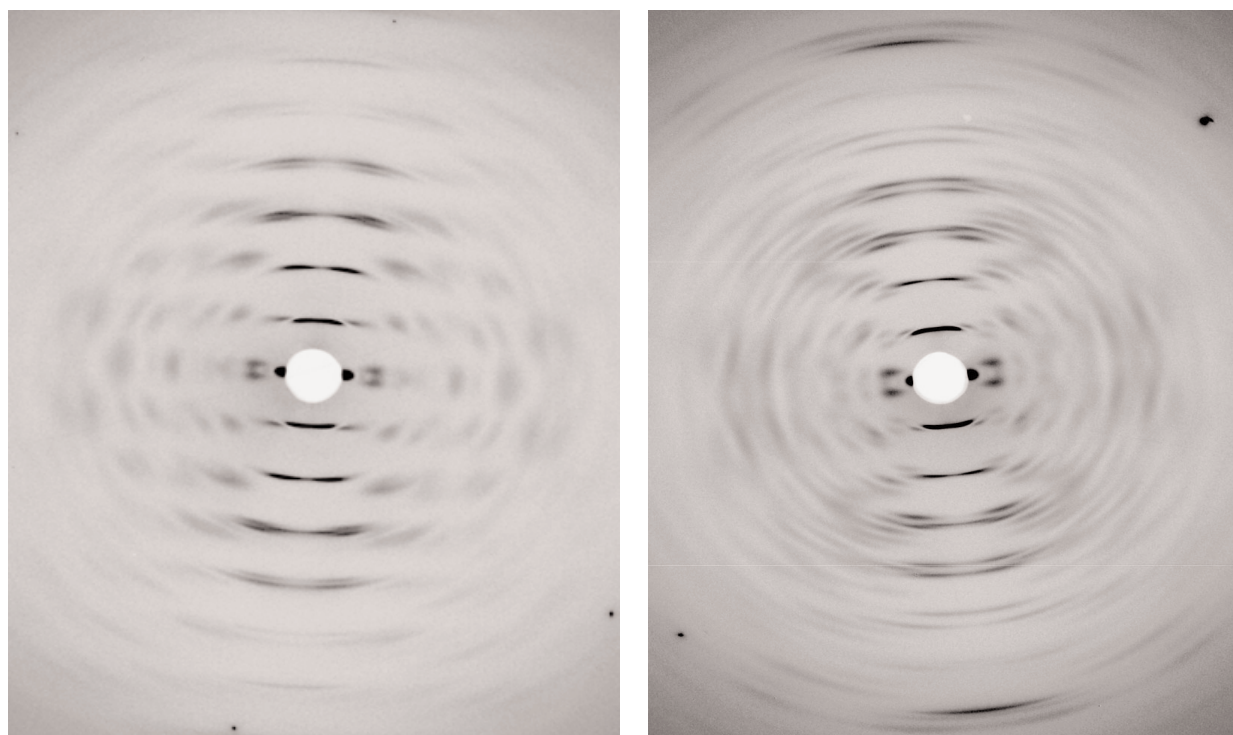


Figure 1: Diffraction patterns from magnetically oriented sols of potato virus X (left) and narcissus mosaic virus (right).

forth by aspiration. Shearing forces produced some orientation, demonstrated by viewing under a polarizing microscope. Following the method of Yamashita et al. (1998), the capillaries were sealed and centrifuged, typically for two to three days at around 5000 g. The dilute region at the top of the capillary was removed, and the capillaries were re-sealed and exposed to the high magnetic field of an NMR magnet (Bruker, Germany), typically 18.8 T for several days or weeks.

Dried fibers were made by suspending 5 µl drops of 10

from the specimen; a low-angle data set was recorded for PVX using a specimen-detector distance of ~400 mm. The detector measured approximately 85 mm horizontally and 50 mm vertically, with a pixel size of 24 µm square. The X-ray wavelength was 1.03 Å.

Data were analyzed using the public domain NIH Image program (developed at the U.S. National Institutes of Health, <http://rsb.info.nih.gov/nih-image/>) for direct measurements and the program WCEN (H. Wang and G. Stubbs, unpublished) for measurements in reciprocal space, including the fitting of layer lines.

Results

Figure 1 shows diffraction patterns from oriented sols of PVX and NMV.

The patterns exhibit, as expected from the similarity between the two viruses, very similar distributions of diffracted intensity. The strong intensities on the first layer lines and on the first near-meridional layer lines indicate the presence of deep intersecting sets of grooves running longitudinally and azimuthally in the viral surfaces (discussed for PVX by Parker et al., 2002). Both viruses exhibit a helical pitch of about 34.5 Å.

The most noteworthy difference between the two patterns is in the layer line spacing. In the PVX pattern, the first layer line is located at about one tenth of the distance of the first near-meridional layer line from the equator. Taken together with other data, this spacing suggests that there are 8.9 subunits per turn of the viral helix. In the NMV pattern, the first layer line is at one fifth of the near-meridional line spacing, indicating that there are only 8.8 subunits per turn. These values are similar to those obtained from lower resolution patterns by earlier workers (Tollin and Wilson, 1985).

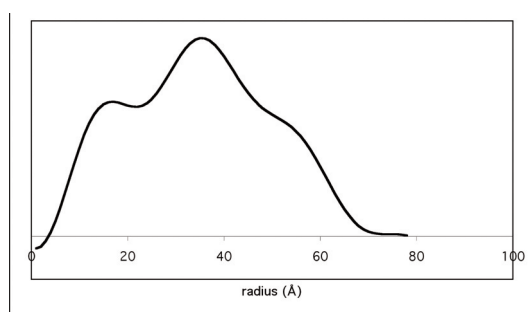


Figure 2: Radial density distribution calculated for PVX. Units on the ordinate are arbitrary

An approximate radial density distribution was determined for PVX. Equatorial structure factors were determined by integrating intensity in the z direction. Because of interference from the first layer line, data were obtainable only for three peaks, including the origin peak, which is behind the beamstop in Fig. 1 but was measured in the low-angle pattern. Structure factors at very low resolution (below 200 Å resolution, the inner part of the origin peak) were estimated as the transform of a cylinder, linearly scaled to be continuous with the measured part of the peak. The origin peak and the next peak were assigned phases of 0° and 180° by the maximum wavelength principle (Bragg and Perutz, 1952). Fourier-Bessel transforms were calculated assigning phases of both 0° and 180° to the third peak, but the resulting radial density distribution was only meaningful for the assigned phase of 180° . A phase of 0° produced a very large, physically implausible electron density peak at zero radius.

The radial density distribution is shown in Fig. 2. The dis-

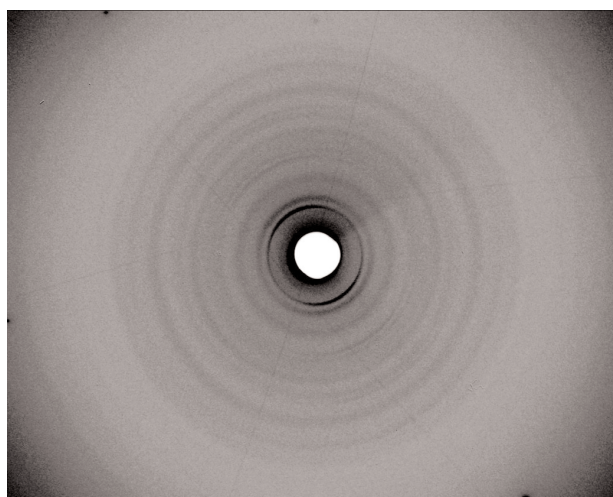


Figure 3: Diffraction pattern from a magnetically oriented sol of wheat streak mosaic virus.

tribution confirms the viral radius as about 65 Å, and shows that the radius of the hole in the center of the filament is about 10 Å, considerably smaller than the 20 Å hole in the tobamoviruses. One might speculate, by analogy with TMV (Caspar, 1956; Franklin, 1956) that the RNA lies at a radius of about 38 Å, corresponding to the highest peak in the density distribution.

Figure 3 shows a diffraction pattern from a magnetically oriented sol of WSMV. While the orientation does not approach that of potexvirus or tobamovirus specimens, there are numerous diffraction maxima, not previously observed in diffraction from any potyvirus. A series of sharp peaks can be interpreted as near-meridional maxima, corresponding to a helical pitch of 33.9 Å, and an off-meridional peak can be interpreted as a layer line at a spacing of 0.0856 Å⁻¹. If this interpretation is correct, WSMV would have a helical symmetry of $u + 0.9$ subunits per turn, and comparison of the viral radius and coat protein molecular weight with those of TMV and PVX suggests that $u = 6$.

A preliminary diffraction pattern (not shown) has been obtained from a dried fiber of the potyvirus bean common mosaic virus (BCMV). This pattern was obtained using a laboratory X-ray source, and shows poor contrast. The orientation, however, is significantly better than that of the WSMV specimen, and it is possible to determine that the helical repeats for the two viruses are very similar.

Discussion

The fine collimation and high intensity of the X-ray beam at BioCAT allowed resolution of layer line 1 in the PVX pattern, and thus permitted accurate determination of the helical repeat and symmetry, a description of the surface features (Parker et al., 2002), and a preliminary determination of the radial density distribution. In the future, the greater layer line spacing in NMV should allow more accurate measurement of equatorial intensities, and a

more accurate radial density distribution. Application of both magnetic orientation and synchrotron radiation has allowed the first determination, albeit preliminary, of the symmetry and helical repeat distance for two potyviruses. Further work with the promising BCMV specimens should allow more accurate determination of these parameters, and offers excellent prospects for the elucidation of more structural features.

Acknowledgements

We thank Markus Voehler and the Vanderbilt University Biomolecular NMR facility for access to magnets, Tom Irving and his staff at BioCAT, David Baulcombe for the inoculum of potato virus X, David Robinson for the inoculum of narcissus mosaic virus, and Phil Berger and Pat Shiel for providing potyviruses. Virus structure research was supported by NSF grant MCB-0235653 and USDA grant 2003-01178. Fiber diffraction methods research was supported by NSF Research Coordination Network grant MCB-0234001. Use of the APS was supported by the U.S. Department of Energy under contract W-31-109-ENG-38. BioCAT is a NIH-supported Research Center RR-08630.

References

- Barrett, A.N., Barrington Leigh, J., Holmes, K.C., Leberman, R., Mandelkow, E., von Sengbusch, P. and Klug, A. (1971) An electron-density map of tobacco mosaic virus at 10 Å resolution. *Cold Spring Harbor Symp. Quant. Biol.*, 36, 433-448.
- Bernal, J.D. and Fankuchen, I. (1941) X-ray and crystallographic studies of plant virus preparations. *J. Gen. Physiol.*, 28, 111-165.
- Bloomer, A.C., Champness, J.N., Bricogne, G., Staden, R. & Klug, A. (1978) Protein disk of tobacco mosaic virus at 2.8 Å resolution showing the interactions within and between subunits. *Nature*, 276, 362-368.
- Bragg, W. L. and Perutz, M.V. (1952) The structure of haemoglobin, *Proc. Roy. Soc. London, ser. A*, 213, 425-435.
- Caspar, D.L.D. (1956) Radial density distribution in the tobacco mosaic virus particle. *Nature*, 177, 928-928.
- Finch, J.T. (1965) Preliminary X-ray diffraction studies on tobacco rattle and barley stripe mosaic viruses. *J. Mol. Biol.*, 12, 612-619.
- Franklin, R. E. (1956b) X-ray diffraction studies of cucumber virus 4 and three strains of tobacco mosaic virus. *Biochim. Biophys. Acta*, 19 203-211.
- Franklin, R.E. (1956a) Location of the ribonucleic acid in the tobacco mosaic virus particle. *Nature*, 177, 928-930.
- Franklin, R.E. and Holmes, K.C. (1958) Tobacco mosaic virus: application of the method of isomorphous replacement to the determination of the helical parameters and radial density distribution. *Acta Cryst.*, 11, 213-220.
- Gregory, J. and Holmes, K.C. (1965) Methods of preparing oriented tobacco mosaic virus sols for X-ray diffraction. *J. Mol. Biol.*, 13, 796-801.
- Holmes, K.C. and Franklin, R.E. (1958) The radial density distribution in some strains of tobacco mosaic virus. *Virology*, 6, 328-336.
- Lobert, S. and Stubbs, G. (1990) Fiber diffraction analysis of cucumber green mottle mosaic virus using limited numbers of heavy-atom derivatives. *Acta Cryst.*, A46, 993-997.
- López-Moya, J.J. and García, J.A. (1999) Potyviruses (Potyviridae). In *Encyclopedia of Virology 2nd edn.*, Vol. 3., Granoff, A. and Webster, R.G., eds. (Academic Press, London), 1369-1375.
- Makowski, L. (1978) Processing of X-ray diffraction data from partially oriented specimens. *J. Appl. Cryst.*, 11, 273-283.
- McDonald, J.G. and Bancroft, J.B. (1977) Assembly studies on potato virus Y and its coat protein. *J. Gen. Virol.*, 35, 251-263.
- Namba, K. and Stubbs, G. (1986) Structure of tobacco mosaic virus at 3.6 Å resolution: implications for assembly. *Science*, 231, 1401-1406.
- Namba, K., Pattanayek, R. and Stubbs, G. (1989) Visualization of protein-nucleic acid interactions in a virus: refinement of intact tobacco mosaic virus at 2.9 Å resolution by fiber diffraction data. *J. Mol. Biol.*, 208, 307-325.
- Parker, L., Kendall, A. and Stubbs, G. (2002) Surface features of potato virus X from fiber diffraction. *Virology*, 300, 291-295.
- Pattanayek, R. and Stubbs, G. (1992) Structure of the U2 strain of tobacco mosaic virus refined at 3.5 Å resolution using x-ray fiber diffraction. *J. Mol. Biol.*, 228, 516-528.
- Planchart, A. (1995) X-ray fiber diffraction studies of odontoglossum ringspot virus. Ph.D. thesis, Vanderbilt University, Nashville.
- Riechmann, J.L., Laín, S., and García, J.A. (1992) Highlights and prospects of potyvirus molecular biology. *J. Gen. Virol.*, 73, 1-16.
- Stubbs, G. and Diamond, R. (1975) The phase problem for cylindrically averaged diffraction patterns. Solution by isomorphous replacement and application to tobacco mosaic virus. *Acta Cryst.*, A31, 709-718.
- Stubbs, G. and Makowski, L. (1982). Coordinated use of isomorphous replacement and layer-line splitting in the phasing of fiber diffraction data. *Acta Cryst.*, A38, 417-425.
- Stubbs, G., Namba, K. and Makowski, L. (1986) Application of restrained least-squares refinement to fiber diffraction from macromolecular assemblies. *Biophys. J.*, 49, 58-60.
- Stubbs, G., Warren, S. and Holmes, K. (1977) Structure of RNA and RNA binding site in tobacco mosaic virus from a 4 Å map calculated from X-ray fibre diagrams. *Nature*, 267, 216-221.

- Tollin, P. and Wilson, H.R. (1971) Some observations on the structure of the Campinas strain of tobacco rattle virus. *J. Gen. Virol.*, 13, 433-440.
- Tollin, P. and Wilson, H.R. (1985). Particle structure. In *The Plant Viruses*, Vol. 4: The Filamentous Plant Viruses, R.G. Milne, ed. (Plenum, New York), 51-83.
- Varma, A., Gibbs, A.J., Woods, R.D. and Finch, J.T. (1968) Some observations on the structure of the filamentous particles of several plant viruses. *J. Gen. Virol.*, 2, 107-114.
- Wang, H. and Stubbs, G. (1993) Molecular dynamics in refinement against fiber diffraction data. *Acta Cryst.*, A49, 504-513.
- Wang, H. and Stubbs, G. (1994) Structure determination of cucumber green mottle mosaic virus by X-ray fiber diffraction. Significance for the evolution of tobamoviruses. *J. Mol. Biol.*, 239, 371-384.
- Wang, H., Culver, J.N. and Stubbs, G. (1997) Structure of ribgrass mosaic virus at 2.9 Å resolution: evolution and taxonomy of tobamoviruses. *J. Mol. Biol.*, 269, 769-779.
- Wang, H., Planchart, A. and Stubbs, G. (1998) Caspar carboxylates: the structural basis of tobamovirus disassembly. *Biophys. J.*, 74, 633-638.
- Yamashita, I., Suzuki, H. and Namba, K. (1998). Multiple-step method for making exceptionally well-oriented liquid-crystalline sols of macromolecular assemblies. *J. Mol. Biol.*, 278, 609-615.

Amyloid Fibrils Formed by Peptide Sequences from a Natural β -Structured Fibrous Protein, the Fibre of Adenovirus

K. Papanikolopoulou^{1,9}, V. Forge², G. Schoehn^{1,2,6}, C. Riekel⁴, J.F. Hernandez^{1,5}, R.W.H. Ruigrok^{3,6}
V. T. Forsyth^{7,8} and A. Mitraki^{1,9}

1. Institut de Biologie Structurale (UMR 5075, CEA-CNRS-UJF), 41 rue Jules Horowitz, 38027 Grenoble, France.
2. Laboratoire de Biophysique Moléculaire et Cellulaire, Unité Mixte de Recherche 5090, Département Réponse et Dynamique Cellulaires, CEA-Grenoble, 17 rue des Martyrs, 38054 Grenoble cedex 9, France.
3. European Molecular Biology Laboratory, 6 rue Jules Horowitz, 38042 Grenoble, France.
4. European Synchrotron Radiation Facility, 6 rue Jules Horowitz, 38042 Grenoble, France.
5. Present address: Laboratoire des Amino Acides, Peptides et Protéines - CNRS UMR 5810, Faculté de Pharmacie, 15 avenue Charles Flahault, 34093 Montpellier, France.
6. Laboratoire de Virologie Moléculaire et Structurale, EA 2939, Université Joseph Fourier, Grenoble 1, France.
7. Institut Laue-Langevin, 6 rue Jules Horowitz, 38042 Grenoble, France.
8. Lennard-Jones Laboratories, School of Chemistry and Physics, Keele University, Staffordshire ST5 5BG, UK
9. Present address: Department of Materials Science and Technology, University of Crete, P.O. Box 2208, 710 03 Heraklion, Crete, Greece.

Introduction

Natural fibrous proteins such as silk fibroins, spider silks and viral spikes are generally both stable and flexible and have recently been shown to contain novel β -motifs composed of repetitive structural elements [1]. Our work focuses on the study of folding, structure and assembly of such a β -structured protein using the fibre from adenovirus as a model system. Adenovirus fibres are trimeric proteins protruding from the viral capsid; they consist of three segments: an N-terminal tail, a long shaft, and a C-terminal globular head. The shaft contains a repeating sequence motif of 15 residues with an invariant glycine or proline and a conserved pattern of hydrophobic amino acids. The structure of a stable domain, comprising the globular head and four shaft repeats [2], has previously been solved at 2.4 Å resolution, revealing a novel triple β -spiral fibrous fold for the shaft [3]. The repeating motif of 15 residues comprises an extended β -strand which runs parallel to the fibre axis, followed by a β -turn containing the conserved glycine or proline. The turn is followed by another β -strand which runs backwards and forms an angle of 45° with the shaft axis; a solvent-exposed loop connects this strand with the extended one of the next repeat. The globular head is thought to play an essential role in the assembly of the protein as mutations or deletions in this part inhibit trimerisation [4, 5]. In order to study the folding and assembly mechanisms of shaft sequences in the absence of the head, a 41 amino-acid peptide corresponding to the part of the shaft that is immediately adjacent to the head was synthesised and studied. This peptide failed to fold into its native triple β -spiral conformation; instead, it self-assembled into amyloid-type fibrils [6]. Amyloid fibrils usually form as a result of misfolding events in proteins, and are associated

with diseases such as Alzheimer's and prion related diseases[7]. In an effort to investigate whether amyloid fibril formation is a general propensity of the shaft sequences, we synthesised shorter synthetic peptides (25, 12, 8, 6 and 4 amino acids) that correspond to specific repetitive sequences from the adenovirus fibre shaft [8]. We report here on the structure and assembly of these 6 peptides using a combination of fibre diffraction, infrared spectroscopy, Congo Red binding and electron microscopy approaches.

Experimental procedure

Peptide synthesis: C-terminal amide derivatives of the 41-mer, 25-mer, 12-mer and 4-mer peptides were synthesised using in-house solid phase chemistry on the Applied Biosystems 430A automated peptide synthesizer [6]. The 6-mer and 8-mer peptides were purchased from Bachem, France. The purity and identity of the peptides were assessed by reverse-phase high performance liquid chromatography and electrospray mass spectrometry. Peptide concentrations were determined by in-house amino acid composition analysis.

Electron microscopy: Peptide powders were dissolved in water prior to adsorption to carbon-coated copper grids. The concentration of the solutions ranged from 0.5 to 20 mg/ml depending on the peptide. The samples were stained with 1% sodium silicotungstate and allowed to dry. Grids were examined with a JEOL 1200 XII transmission electron microscope. Negatively stained crystals of catalase were used as a calibration standard.

Congo Red staining and Birefringence: Peptide fibril suspensions were stained with a 10 μ M Congo red solution

in water. The fibrils were concentrated by centrifugation and applied to glass slides. Samples were observed with a Zeiss Axiophot microscope equipped with cross-polars.

Fourier Transform Infra Red Spectroscopy (FTIR): FTIR samples were prepared by dissolving the peptides in D₂O except for the 25 amino acid peptide which was dissolved in 10mM deuterated ammonium acetate buffer pH 4. Samples were placed between two CaF₂ windows (Spectra tech) separated by a 100 µm spacer. All spectra were recorded on a JASCO 610 Fourier transform spectrometer with a 4 cm⁻¹ resolution at room temperature. The interferograms from sixteen scans were averaged, and the solvent spectrum was subtracted.

X-ray fibre diffraction: Lyophilised peptide powders were dissolved in 10mM ammonium acetate buffer pH 4. Samples for X-ray fibre diffraction were prepared by air-drying a 5 µl drop of fibril solution between two glass-rod ends. For the 41 amino acid peptide, alignment of the fibrils was improved by the use of the magnetic field available in the NMR laboratory at the Institut de Biologie Structurale in Grenoble. For the peptides of 25 and 12 amino acids, we did not note any improvement in the alignment by the use of magnetic field.

Samples were studied using the microfocus beamline ID13 at the European Synchrotron Radiation Facility (ESRF), equipped with a MAR CCD detector with a 130 nm entrance window and the following readout parameters: 2048 x 2048 pixels, 64.45 x 64.45 µm pixel size. The wavelength was 0.976 Å and the beam was 5-10 µm in diameter. The sample-to-detector distance ranged from 57.1 - 42.8 mm. Diffraction datasets were processed and measured using CCP13 software [9] and the FIT2D package [10].

Results and Discussion

The design of different peptides was based on the crystalline structure of the native protein (Fig. 1). The 4 amino acid peptide corresponds to the flexible region connecting the head to the shaft and is not part of the shaft repeats.

Amyloid is defined by three criteria, namely its tinctorial affinity for the dye Congo Red, its fibrillar morphology upon analysis by electron microscopy and its characteristic "cross-β" X-ray diffraction pattern. Linear, non-branching fibrils with variable lengths and a diameter ranging from 16 to 30 Å have been detected by electron microscopy (Fig. 2a) for all the peptides except for the 4 amino acid one. These fibrils bind Congo Red and produce a gold-green birefringence under polarised light (Fig. 2b). Infrared results (Fig. 3) suggest that the fibrils formed from the different peptides adopt a β-sheet conformation as revealed by the presence of the band at ~1620 cm⁻¹. The spectrum recorded for the 4 amino acid peptide displays a peak at 1645 cm⁻¹ characteristic of the random coil conformation.

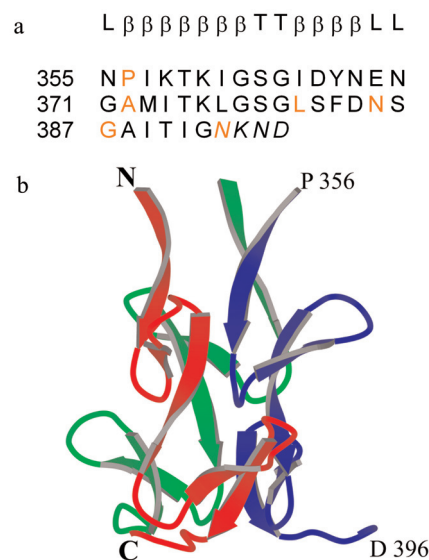


Figure 1: a) Sequence of the various peptides. Residue numbers correspond to positions in the full-length fiber sequence. Each line corresponds to a sequence pseudo-repeat of 15 residues. The last four amino acids in italics are not part of a repeat but belong to the linker region that connects the shaft to the head domain. The first amino acid of each peptide is coloured. The conserved secondary structure of the repeats is shown above with L for loop, β for β-strand and T for β-turn. b) Structure of the 41 amino acid peptide within the native shaft segment. The three chains are coloured differently; their N and C-termini are labeled corresponding to residues 355 and 396 respectively. All the other peptides are subsequences of the 41-mer. (Figure courtesy of Dr. Mark van Raaij, Universidad de Santiago de Compostela, Spain).

Fibre diffraction has turned out to be a key technique for the study of amyloid structures. The power of the method lies in the fact that the data produced are usually directly relevant to the system being studied, and less affected by artefacts that can be important in single crystal work (e.g. limited length of oligomers, presence of crystallising agents). The current diffraction work was aimed principally at using fibre diffraction as a means identifying the fibres as amyloid in character. The samples produced as described above were found to be cylindrically symmetric -i.e. producing diffraction patterns that were invariant as a function of rotation about the fibre axis. Figure 4 shows typical "cross-β" X-ray fibre diffraction patterns recorded from the 41, 25, 12, 8 and 6 amino acid peptides. A clear meridional reflection at 4.7 Å and a more diffuse reflection on the equator between 10 and 11 Å are present in all five patterns. These two reflections are consistent with a β-structure where the β-sheets are spaced by ~10 Å and arranged parallel to the fibre axis with their β-strands aligned perpendicular to that direction [11, 12]. The 4.7 Å reflection on the meridian corresponds to the interstrand distance. Further reflections in the meridional direction at ~2.4 Å and ~1.6 Å are visible in all patterns as shown for the 25 amino acid peptide in Fig. 5. The

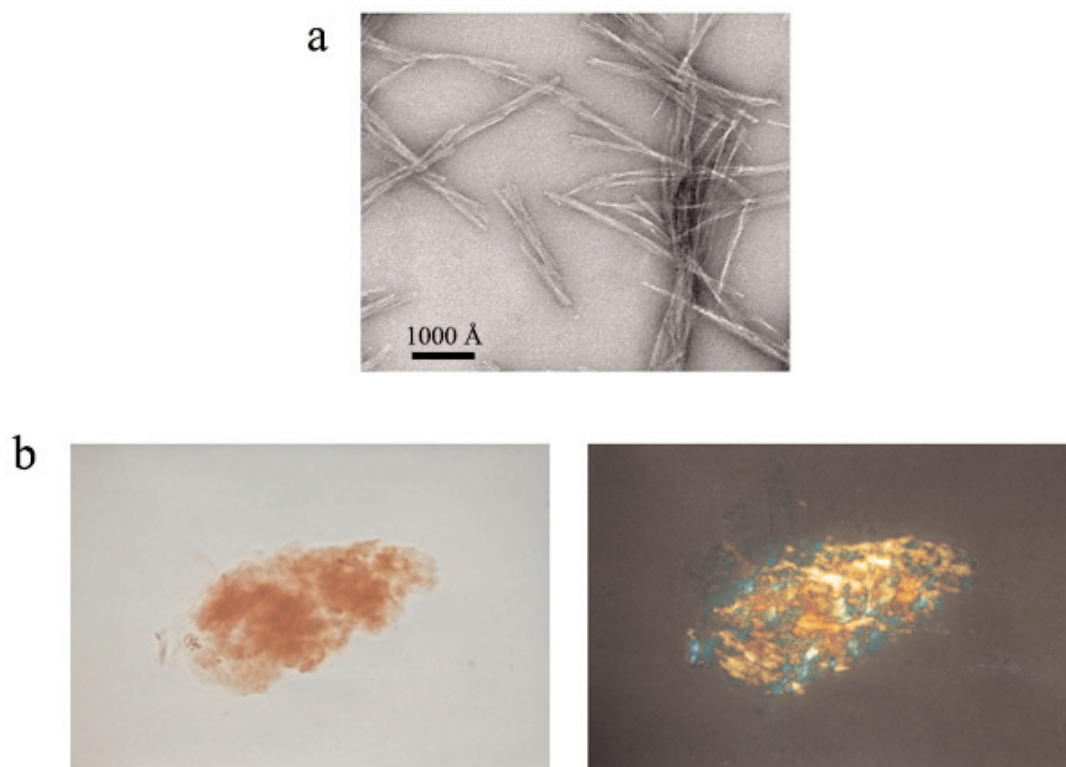
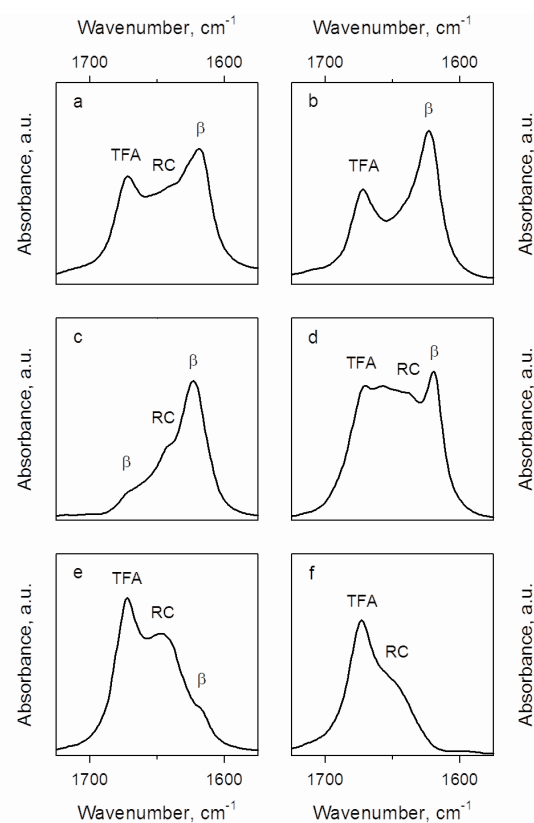


Figure 2: Results are shown for the 41 amino acid peptide. a) Electron micrograph of fibrils stained with 1% sodium silicotungstate. The peptide was solubilised in water at a 0.5 mg/ml concentration. b) Photomicrographs of fibrils stained with Congo Red and observed under bright field illumination (left panel) and between crossed polars (right panel). Similar observations were made for all of the five amyloid-forming peptides.

equatorial reflections in the patterns varied very significantly; they are diffuse in the pattern of the 41 amino acid peptide and become more distinct in the shorter peptides. As judged by the above structural criteria, all the peptides, except for the 4-mer, have an intrinsic capacity to form amyloid fibrils. Thus, self-assembly into amyloid fibrils is a general property of the shaft sequences when isolated from their native context. The X-ray fibre diffraction and infrared results suggest that the fibrils formed from the different peptides share a common β -sheet framework structure where the β -strands lie perpendicular to the fibre axis. From the crystal structure of the shaft segment and the current structural studies it becomes obvious that the amyloid signature is different from the native triple β -spiral fold. The above results further support the essential role of the head domain in fibre assem-

Figure 3: Infrared spectra of the peptide solutions made from the a) 41-mer b) 25-mer c) 12-mer d) 8-mer e) 6-mer and f) 4-mer. Only the amide I region is shown. The positions assigned to the various secondary structure elements are marked as RC for random coil and β for β -sheet. The position corresponding to residual trifluoroacetic acid as a result of the purification procedure is marked as TFA. Peptide solutions were prepared and spectra were recorded after 44 hours for the 41 aa peptide, 18 hours for the 25 aa, 32 hours for the 12 aa, 20 hours for the 8 aa, 6 days for the 6 aa and one month for the 4 aa peptide. The concentrations of the peptide solutions were as follows: 10 mg/ml for the 41-mer, 25-mer and 4-mer, 5 mg/ml for the 12-mer and 20 mg/ml for the 8-mer and 6-mer.



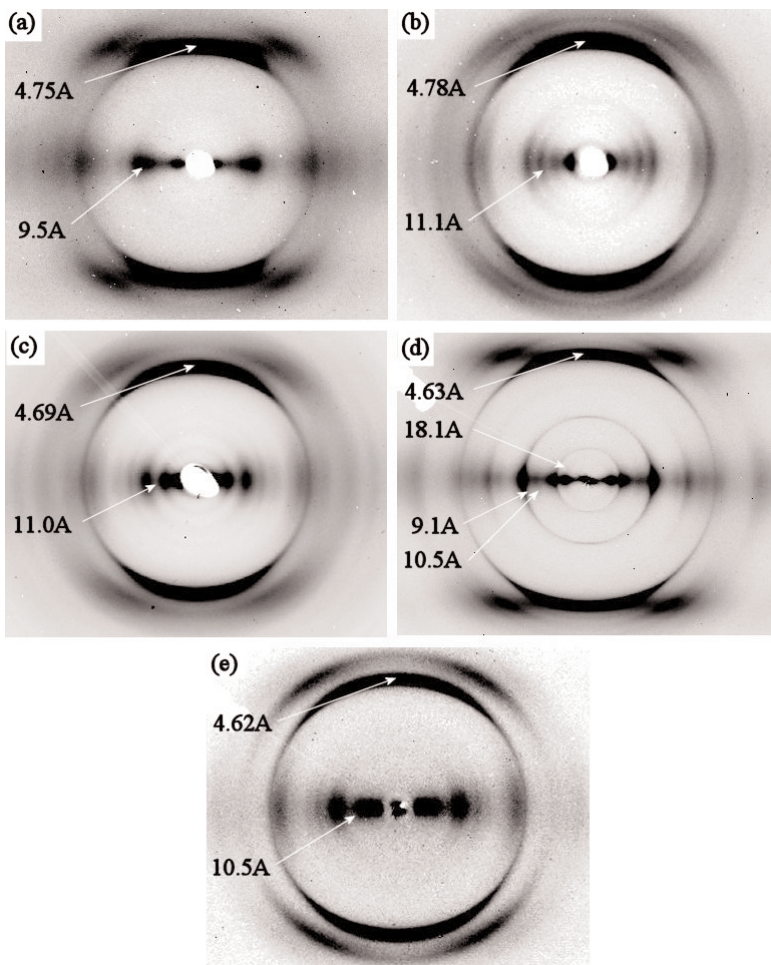


Figure 4: Diffraction patterns recorded from amyloid fibres formed from the shaft peptides of a) 41 b) 25 c) 12 d) 8 and e) 6 amino acids. The two major characteristic reflections (4.7 Å and ~10 Å) of the cross-β structure are marked with arrows. In the pattern of the 8-mer two additional reflections at 9.1 Å and 18.1 Å are indicated.

bly. The aggregation of the shaft sequences into amyloid may occur as a result of out-of register interactions in the absence of the head. The globular part might act as a registration signal necessary for the three chains to align and fold together. It is worth mentioning that, when the native head is replaced by a foreign trimerisation motif, the shaft sequences trimerise successfully and adopt the triple β-spiral conformation [13, 14]. The results reported in this paper are relevant to understanding amyloid formation by repetitive sequences from disease-associated proteins. The adenovirus shaft sequences can provide a model system to study folding, assembly and registration of β-type structures both in native and in amyloid contexts.

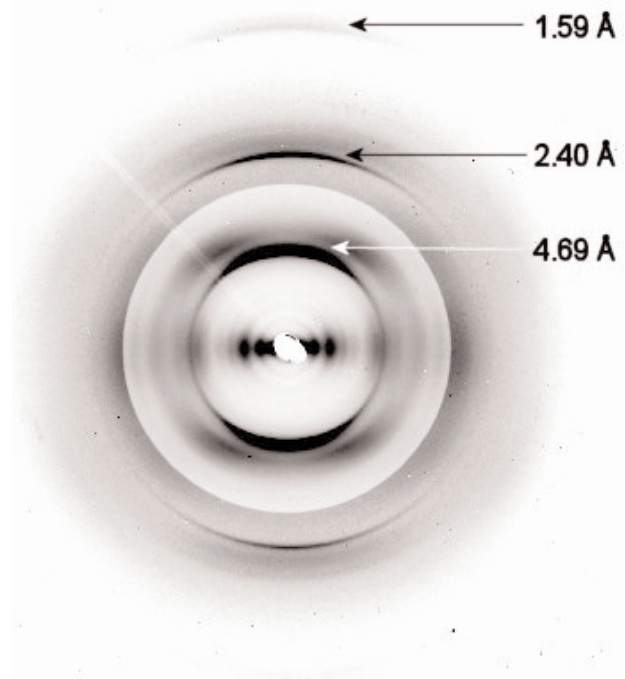


Figure 5: X-ray fibre diffraction pattern taken from aligned fibrils of the 12-mer. The observed meridional reflections at 1.59 Å and 2.40 Å as well as at 4.69 Å are indicated with arrows. Similar results were obtained for all the other peptides.

References

- [1] Mitraki, A., Miller, S. & van Raaij, M.J. (2002). Review: conformation and folding of novel Beta-structural elements in viral fiber proteins: the triple Beta-spiral and triple Beta-helix. *J. Struct. Biol.* **137**, 236-47.
- [2] Mitraki, A., Barge, A., Chroboczek, J., Andrieu, J.P., Gagnon, J. & Ruigrok, R.W. (1999). Unfolding studies of human adenovirus type 2 fibre trimers. Evidence for a stable domain. *Eur. J. Biochem.* **264**, 599-606.
- [3] van Raaij, M.J., Mitraki, A., Lavigne, G. & Cusack, S. (1999). A triple beta-spiral in the adenovirus fibre shaft reveals a new structural motif for a fibrous protein. *Nature*, **401**, 935-8.
- [4] Novelli, A. & Boulanger, P.A. (1991). Deletion analysis of functional domains in baculovirus-expressed adenovirus type 2 fiber. *Virology*, **185**, 365-376.
- [5] Hong, J.S. & Engler, J.A. (1996). Domains required for assembly of adenovirus type 2 fiber trimers. *J. Virol.* **70**, 7071-7078.
- [6] Luckey, M., Hernandez, J., Arlaud, G., Forsyth, V.T., Ruigrok, R.W. & Mitraki, A. (2000). A peptide from the adenovirus fiber shaft forms amyloid-type fibrils. *FEBS. Lett.* **468**, 23-27.
- [7] Kelly, J.W. (1998). The alternative conformations of amyloidogenic proteins and their multi-step assembly pathways. *Curr. Opin. Struct. Biol.* **8**, 101-6.
- [8] Papanikolopoulou, K., Schoehn, G., Forge, V., Forsyth, V.T., Riek, C., Hernandez, J.F., Ruigrok, R.W. & Mitraki, A. (2005). Amyloid fibril formation from sequences of a natural beta-structured fibrous protein, the adenovirus fiber. *J. Biol. Chem.* **280**, 2481-2490.
- [9] Squire, J.M., Al-Khayat, H., Arnott, S., Crawshaw, J., Diakun, G., Denny, R.C., Dover, D., Forsyth, V.T., He, A., Knupp, C., Mant, G.R., Rajkumar, G., Rodman, M.J., Shotton, M.S., Windle, A. (2003). New CCP13 software and the strategy behind further developments: stripping and modelling of fibre diffraction data. *Fibre Diffraction Review*, **11**, 7-19.
- [10] Hammersley AP (1998). FIT2D V9.129 Reference Manual V3.1. ESRF Internal Report **ESRF98HA01T**.
- [11] Serpell, L.C., Fraser, P.E. & Sunde, M. (1999). X-ray fiber diffraction of amyloid fibrils. *Methods Enzymol.* **309**, 526-36.
- [12] Sunde, M. & Blake, C. (1997). The structure of amyloid fibrils by electron microscopy and X-ray diffraction. *Advances in Protein Chemistry*, **50**, 123-159.
- [13] Papanikolopoulou, K., Forge, V., Goeltz, P. & Mitraki, A. (2004). Formation of highly stable chimeric trimers by fusion of an adenovirus fiber shaft fragment with the foldon domain of bacteriophage t4 fibritin. *J. Biol. Chem.* **279**, 8991-8.
- [14] Papanikolopoulou, K., Teixeira, S., Belrhali, H., Forsyth, V.T., Mitraki, A. & van Raaij, M.J. (2004). Adenovirus fibre shaft sequences fold into the native triple beta-spiral fold when N-terminally fused to the bacteriophage T4 fibritin foldon trimerisation motif. *J. Mol. Biol.* **342**, 219-27.

In-situ WAXS Studies of Structural Changes in Wood Foils and in Individual Wood Cells During Microtensile Tests

J. Keckes¹, I. Burgert², M. Müller³, K. Kölln³, M. Hamilton⁴, M. Burghammer⁴, S.V. Roth⁴, S.E. Stanzl-Tschegg⁵ and P. Fratzl².

[1] Erich Schmid Institute for Materials Science, Austrian Academy of Sciences and Institute of Metal Physics, University of Leoben, Austria

[2] Max-Planck-Institute of Colloids and Interfaces, Department of Biomaterials, Potsdam, Germany

[3] Institute for Experimental and Applied Physics, University Kiel, Germany

[4] European Synchrotron Radiation Facility, Grenoble, France

[5] Institute of Physics and Materials Science, BOKU - University of Natural Resources and Applied Life Sciences, Vienna, Austria

Introduction

The distinctive mechanical qualities of biological materials can be directly attributed to their *hierarchical architecture* with a variety of compositional, structural and dimensional units [1]. Moreover, the recent *in-situ* studies of nacre and bone have indicated also the important role of *molecular interactions* and bond recovery phenomena operating at the nanometer level [2]. The molecular mechanistic phenomena are responsible for various stiffness recovery effects at molecular and submolecular levels and originate in deformability, folding, branching, interfacial interaction and compositional variability of polymers in the biological structures [1,2].

Wood is also a complex, hierarchically structured, polymer-like material based on fibrils of crystalline cellulose and amorphous matrix of lignin and hemicelluloses. In comparison with artificial materials, wood exhibits a remarkably good mechanical performance when taking its low density into consideration [3]. There has been a significant effort to characterize the structural and mechanical properties of various wood tissue types using numerous experimental techniques and modelling approaches with an aim to understanding the contribution of the lowest hierarchical units to the mechanical performance of the tissue [4,5]. It has been demonstrated by several authors that the mechanical properties of wood are significantly influenced by fibrils of crystalline cellulose wound in the form of a Z-Helix around the lumen [6-10]. The tilt angle of the cellulose fibrils in the S2-layer versus the longitudinal cell axis (usually called microfibril angle [MFA]) plays an important role in determining the actual stiffness of wood.

When investigating the properties of wood, one of the main difficulties is the compositional, architectural and dimensional variability of the tissue constituents

originating in the hierarchical nature of the material. The understanding of structure-property relationships in wood thus requires use of complex characterization techniques which probe the properties and role of various tissue constituents as well as their interaction. In-situ deformation experiments combined with structural characterization represent a powerful methodological tool to characterize properties of complex materials. In this work, results from synchrotron wide-angle X-ray scattering (WAXS) experiments on thin wood foils and on individual wood cells combined with tensile tests are reported. The main goal of these simultaneous structural and mechanical investigations on wood foils and wood cells was to (i) *characterize structural changes* in the tissues at different stages of the tensile experiments and to (ii) *separate deformation mechanisms* inside the cell-wall from those mediated by cell-cell interactions. The results indicate the presence of a re-stiffening mechanism in the cell wall, which was related to the properties of the amorphous polymer cell constituents [11,12].

Materials and Methods

From compression wood of *Ginkgo biloba* L., *Juniperus virginiana* L. and *Picea abies* [L.] Karst., tangential sections with dimensions of 50 x 5 x 0.2 mm³ and individual cells of 20-30 µm in diameter and 1-1.5 mm in length were prepared. The individual wood cells were isolated mechanically using very fine tweezers in order not to modify the chemical and the structural properties of the cell wall [13]. The application of this isolation technique allowed study of the mechanical behaviour of the unmodified cell wall and made it possible to evaluate the contribution of the distinct cell wall components to the mechanical behaviour of the intact tissue.

The tissues were characterised using *in-situ* diffraction

experiments performed at the European Synchrotron Radiation Facility (ESRF) in Grenoble, France (Fig. 1). The foils as well as the cells were investigated in transmission geometry with the X-ray beam perpendicular to the cell axis. For the investigations on foils, a tensile stage developed by the authors was delivered to the ID1 beamline before the experiment. The computer-controlled stage allowing the measurement of sample elongation and force applied on the sample was inserted in the goniometer. The beam of 0.5 mm in diameter was used and the scattering signal was collected using a two-dimensional (2D) CCD detector. The wood foils were strained in a tensile stage under various strain rates monitoring stress response and structural changes.

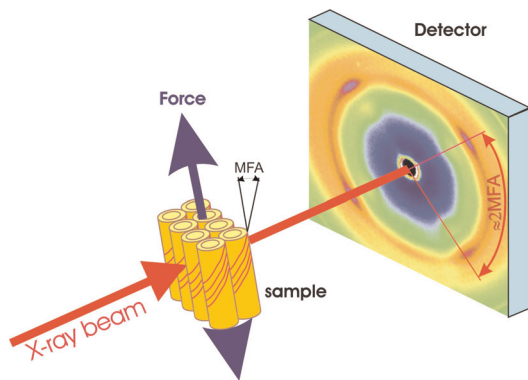


Figure 1. A schematic description of the in-situ synchrotron WAXS. A wood foil (or a single wood cell) was strained in a tensile stage while the structural changes were monitored using the 2D CCD detector in transmission geometry. After the measurement, the MFA magnitudes were evaluated from the WAXS data for different stages of the tensile experiment and, subsequently, the mechanical and the structural values were correlated.

In the case of individual cells, the characterization was performed at the ESRF microfocus beamline ID13 with a beam of 2 μm diameter. The cells were tested in a piezoelectric stretching device provided by the ESRF working with a rate of 500 nm/s. As in the case of foils, the mechanical data (such as force applied on the cell and the cell elongation) and the structural changes (characterized using the 2D CCD detector) were monitored.

By relating the stress-strain curves and scattering results, it was possible to evaluate changes of the MFA as a function of external strain and the strain rate in the tissues. The magnitudes of the MFA were evaluated from cellulose 200 reflections as described in Ref. 8.

Results and Discussion

Figure 2 presents typical WAXS patterns collected at the beginning and the end of the tensile experiments on a foil of *Picea*. In Fig. 3, distributions of the intensity along cellulose 200 Debye-Scherrer rings obtained by the integration of the WAXS patterns (Fig. 2) are presented. The results indicate a change of the MFA from 43° to 30°. The

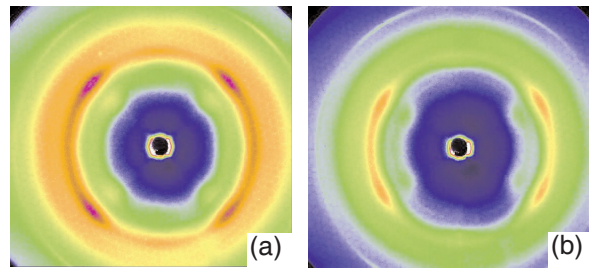


Figure 2. Results from WAXS on a foil of *Picea*. The patterns (a) and (b) collected at the beginning and at the end of the in-situ experiment, respectively, demonstrate a decrease of MFA in the foil.

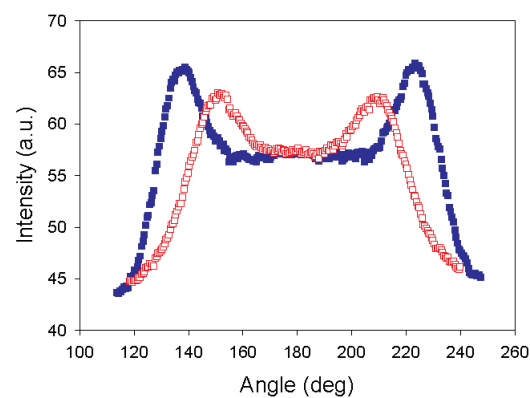


Figure 3. Results from WAXS on a foil of *Picea*. Filled and empty symbols represent integrated data from Fig. 2a and b, respectively. The data demonstrate a decrease of MFA in the foil from 43° to 30° due to straining.

MFA magnitude was evaluated for different stages of the tensile experiments and the mechanical data were correlated with the structural changes, namely with the development of the MFA in the tissues. In Figs. 4,5 mechanical and structural results obtained from foils and cell of *Picea* are presented.

In the case of the foil (Fig. 4a,b), the mechanical behaviour was decisively influenced by the magnitude of MFA in the unstressed state [4,5]. During the initial period of testing, the tissues exhibited a relatively high stiffness. In the plastic region, however, when the straining was interrupted, the original stiffness was recovered after reloading. With an additional increase in the strain, the region with lower stiffness was reached again.

The analysis of the structural data from foils (Figs. 4a,b) documents that the MFA decreases when the strain increases [11]. The MFA magnitude can be related to the actual value of the strain and is not influenced by the strain rate. Even at zero strain rates, the MFA does not change significantly. The MFA dependence on strain can be approximately described by the equation:

$$MFA(\epsilon) = MFA(0) - \cotg[MFA(0)] \epsilon. \quad (1)$$

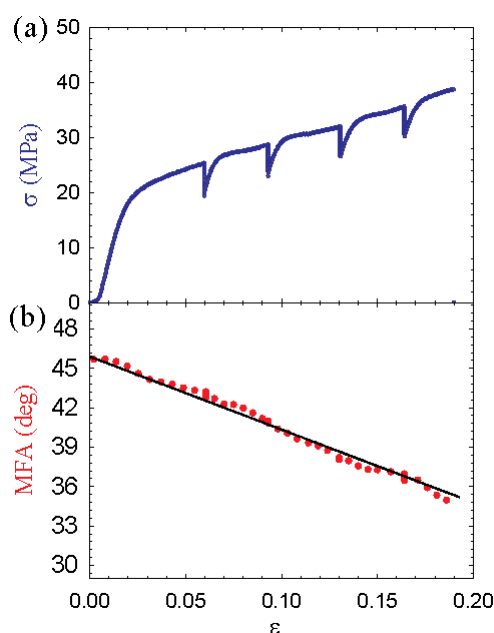


Figure 4. Mechanical and structural data from in-situ WAXS experiments on a foil of *Picea*. The stress-strain curve in (a) documents that the straining of the foil was interrupted four times. In (b) the corresponding dependence of the MFA as a function the strain is depicted by points. The solid line in (b) represents a theoretical dependence of the MFA on the strain calculated on the basis of the model introduced in Ref 11 (Eq. 1).

In the case of *in-situ* tests on individual cells, structural and mechanical behaviour similar to that in foils was observed. The results in Fig. 5a,b document a decrease of MFA in a cell of *Picea* that broke at relatively low strain. The main difference in the behaviour of the foils and the cells was that the deformation in single cells was not uniform over the length of the cell. In some regions the deformation could be exceedingly large (reducing the MFA almost down to zero) while other regions of the cell were less deformed. The results in Fig. 5a,b indicate that, close to the fracture, the MFA in the cell decreased and did not follow the dependence predicted by Eq. 1. In further cyclic loading tests in laboratory conditions (performed without X-ray radiation) individual cells and foils exhibited a similar stress-strain behaviour as the tissues examined during in-situ WAXS experiments [11].

The interpretation of the experimental data indicates that the mechanical behaviour of wood is influenced by the magnitude of the MFA and an additional mechanism responsible for the stiffness recovery beyond the yield point. This mechanism is not likely to originate in crystalline cellulose and must therefore be connected with the amorphous constituents of the cell wall [12]. It is supposed that the re-stiffening effect under cyclic loading originates in the bond recovery occurring in the amorphous matrix between the helical cellulose microfibrils [11,12]. As in the case of nacre and bone, this phenomenon governs the formation and breaking of polymer cross-links in the cell wall and, in this way, provides a

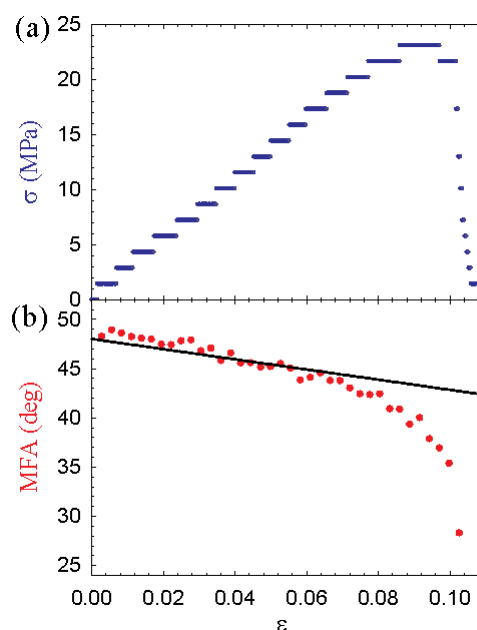


Figure 5. Mechanical (a) and structural (b) data from in-situ WAXS experiments on a single cell of *Picea*. The solid line in (b) represents a theoretical dependence of MFA on the strain calculated on the bases of the model introduced in Ref 11 (Eq. 1).

plastic-like behaviour to the biological material. It can be supposed that this "Velcro-like" behaviour could be mediated by the hemicelluloses attached to the cellulose fibrils [11,12]. However, further investigations are necessary to fully understand the mechanical interaction of the polymers in the cell wall.

Acknowledgements

This work was partly supported by the Fonds zur Förderung der wissenschaftlichen Forschung (FWF), Project P14331-PHY.

References

- [1] Gao, H., Ji H., Jäger, J., Arzt, E., Fratzl, P. (2003). Proc Natl Acad Sci USA. 100, 5597-5600.
- [2] Smith, L.B., Schäffer, T.E., Viani, M., Thompson, J.B., Frederick, N.A., Kindt, J., Belcher, A., Stucky, G.D., Morse, D.E., Hansma, P.K. (1999) Nature 399, 761-763.
- [3] Ashby, M.F., Gibson, L.J., Wegst, U., Olive, R. (1995) Proc. Roy. Soc. Lond. A 450 123-140.
- [4] Köhler, L., Spatz, H.C. (2002) Planta 215, 33-40.
- [5] Navi, P., Rastogi, P.K., Gresse, V., Tolou, A. (1995) Wood Sci. Technol. 19, 411-419.
- [6] Bergander, A., Salmén, L (2002). J. Mater. Sci. 37, 151-156.
- [7] Cave, I.D., Walker, J.C.F. (1994) Forest Products J. 44, 43-48.
- [8] Lichtenegger, H., Reiterer, A., Stanzl-Tschegg, S.E., Fratzl, P. (1998) In: Microfibril Angle in

- Wood, Butterfield, B.G. Editor IAWA-press, pp. 140-156.
- [9] Hoffmann, B.C., Chabbert, B., Monties, B., Speck, T. (2003) *Planta* 217, 32-40.
- [10] Hepworth D.G., Vincent J.F.V. (1998) *Annals of Botany* 81, 761-770.
- [11] Keckes, J., Burgert I., Frühmann K., Müller M., Kölln K., Hamilton M., Burghammer M., Roth S.V., Stanzl-Tschegg S.E., Fratzl P. (2003) *Nature Materials* 2, 810-814.
- [12] Fratzl, P., Burgert, I, Gupta, H. S. (2004) *Phys. Chem. Chem. Phys.* 6, 5575 -5579.
- [13] Burgert I., Keckes J., Frühmann K., Fratzl P., Tschegg S. E. (2002) *Plant Biology* 4, 9-12.

13th Annual Workshop Abstracts

Talk Abstracts

Joint use of small-angle X-ray and neutron scattering from biomacromolecular solutions

Dmitri I Svergun

European Molecular Biology Laboratory, Hamburg
Outstation c/o DESY, Notketstr. 85, D22603 Hamburg,
Germany and Institute of Crystallography, Russian Academy
of Sciences, Leninsky pr. 59, 117333 Moscow, Russia

Small-angle scattering of X-rays and neutrons (SAS) is a fundamental tool in the study of biological macromolecules [1]. SAS allows to study the structure of native particles in nearly physiological solutions and to analyse structural changes in response to variations in external conditions. The method is applicable to a broad range of sizes, from individual macromolecules to multi-domain proteins and large macromolecular assemblies. The scattering data bear information about the overall shape and internal structure at a resolution of 1-2 nm. Recently developed advanced methods of data analysis significantly enhance resolution and reliability of structural models provided by the technique and make solution scattering a useful complementary tool to high resolution methods.

Advanced methods to analyze SAS data from solutions of biological macromolecules will be presented including *ab initio* low resolution shape and domain structure determination and modeling of quaternary structure by rigid body refinement. Special emphasis will be put to the joint use of X-rays and neutrons combined with contrast variation by hydrogen/deuterium exchange. Practical applications of the methods will be illustrated by recent examples.

Why are joint X-ray and neutron scattering studies useful for studying antibodies?

S J Perkins

Department of Biochemistry and Molecular Biology, Royal
Free and University College Medical School, University
College London, Gower Street, London WC1E 6BT, UK

Classical X-ray and neutron solution scattering studies each provide information at low structural resolutions of between 2-4 nm. Analytical ultracentrifugation provides

complementary structural information from sedimentation velocity experiments. In recent years, the structural detail from these experiments has been improved by the use of constrained molecular modelling based on known crystal structures in order to yield structures at medium resolutions. The advantages of a joint X-ray/ neutron/ ultracentrifugation strategy include the use of (1) more reliable experimental data acquisition; (2) a wide range of solute-solvent contrasts; (3) combination of different instrumental conditions; (4) complementary hydrated and unhydrated views of the macromolecule; (5) comparison of different modelling algorithms. The combination of all three experimental approaches has yielded insight into the solution structures of antibodies and their biological function. Examples taken from scattering projects with the five human and mouse antibody classes will illustrate these points.

The use of hydrogenated and deuterated DNA in neutron studies of DNA-membrane interactions

**D J Barlow¹, P Callow^{2,3}, V Laux²,
M J Lawrence¹, T Forsyth^{2,3}, G Fragneto²,
I Parrot², J P Talbot¹, P Timmins² and
M Haertlein²**

1. Pharmacy Department, King's College London,
London SE1 9NN

2. Institut Laue Langevin, Grenoble, France

3. Lennard-Jones Laboratories, School of Chemistry &
Physics, Keele University, Staffordshire ST5 5BG, UK

Vesicles formed from natural phospholipids have been overlooked as DNA delivery vectors because of the low affinity shown by zwitterionic lipids for DNA. Recent studies however have suggested that the interaction of DNA with zwitterionic lipids can be enhanced by the addition of divalent ions such as calcium. The aim of the work was to establish the existence and extent of such interactions using the technique of neutron reflectivity, examining the effects of DNA, in the presence and absence of calcium, on a monolayer formed at the air-water interface by the zwitterionic phospholipids 1, 2,-distearoyl-sn-glycero-3-phosphocholine (DSPC). Deuterated and protonated forms of DMPC and DNA were used in the study.

Analysis of the reflectivity data indicated that structural changes to the phospholipid monolayers were observed in the presence of calcium and were the direct result of interaction with DNA. The DNA appeared to insert itself into the phospholipid monolayer and/or cause a structural rearrangement of the phospholipid molecules within the layer to occupy a greater interfacial area. Changes of a similar nature but of a much smaller magnitude and slower time were observed in the absence of calcium. On the basis of these findings, it has been possible to propose a mechanism for how calcium mediates the interaction of phospholipid with DNA.

It is clear from these studies that calcium does promote interactions between zwitterionic phospholipids and DNA, and that these systems might thus make suitable (non-toxic) vectors for gene delivery.

ILL's instrument suite for biology

P A Timmins

Institut Laue Langevin, 6 Rue Jules Horowitz, 38042
Grenoble Cedex 9, France

Introduction

ILL has a large range of instruments for the study of biomolecular structure and dynamics. In general the instruments are not dedicated to biological studies but are used over a wide range of condensed matter studies. Broadly speaking the instruments may be divided into five categories:

High resolution single crystal and fibre diffraction

LADI is a diffractometer for high resolution neutron crystallography of biological macromolecules, run jointly by ILL/EMBL. It is based on the quasi-Laue principle, which exploits a wavelength of band of some 2 - 4 Å exploiting an image plate as the detecting device. An upgrade of LADI (called LADI-3) is one of the Millennium projects.

D19 is a diffractometer optimised for fibre diffraction and small single crystal systems. Major modifications, funded by the EPSRC, yielding an overall efficiency gain of ~25, will be implemented in the coming 12-18 months.

Low resolution diffraction

D16 is a two axis spectrometer suitable for the study of membrane systems. Over the past 5 years the instrument has been sited on a dedicated 20 cm high guide and been installed with a focussing pyrolytic graphite monochromator. A new multi-wire detector, covering a larger angular range than previously, has been installed.

DB21 is a cold neutron diffractometer jointly run with EMBL and is dedicated to the study of large molecular complexes at low (~10Å) resolution. The H₂O/D₂O contrast variation technique is exploited to look at single components of, for example, protein-nucleic acid com-

plexes.

Small angle scattering

D11 and **D22** are the world's highest flux small angle neutron scattering instruments. D11 has recently been refurbished with a new collimation system allowing an optimal balance between beam divergence and sample-detector distance. D22 has a slightly higher flux than D11 and thanks to its 1 metre square multidetector which can be laterally offset, a wider dynamic Q-range. A new detector consisting of an array of tubes with individual wires allowing count rates of up to 2 x 10⁶ neutrons per second has recently been installed.

Reflectometry

D17 is a time-of-flight reflectometer working with samples in vertical geometry. Its applications in biology are in the study of model membranes and the penetration of peptides or small proteins into the lipid bilayer.

Inelastic scattering

IN5, **IN6**, **IN10**, **IN13** and **IN16** are instruments for inelastic scattering, each of which carries out some studies of the dynamics of macromolecules. The energy and Q resolutions of the instruments vary and therefore any particular study may require the use of a number of these instruments. In general they exploit the incoherent scattering from hydrogen atoms and therefore "reverse" labelling (i.e. the substitution of specific hydrogens into a fully deuterated molecule) is required.

The ILL-EMBL Deuteration Facility: A platform for labeling of biological macromolecules for Neutron Studies

**M Haertlein¹, V T Forsyth^{1,3}, D A A Myles²,
P A Timmins¹**

1. Institut Laue Langevin, 6 Rue Jules Horowitz, 38042
Grenoble Cedex 9, France

2. EMBL Grenoble Outstation, 6 Rue Jules Horowitz, 38042
Grenoble Cedex 9, France

3. School of Chemistry and Physics, Keele University,
Staffordshire, UK

The ability to deuterate samples has for a long time been a key issue for biological neutron scattering. As part of the expansion of its life sciences programme the ILL, in collaboration with the EMBL-Grenoble, has established a joint laboratory to support the deuteration of biological molecules for neutron scattering experiments. This initiative as part of the Partnership for Structural Biology Programme will provide the tools and facilities required for the specific and selective isotopic-labelling of complex bio-molecules such as proteins, nucleic acids and lipids. The provision of these deuterated molecules should greatly enhance both the quality and quantity of

neutron experiments that can be done at ILL and in many cases will make feasible new more sophisticated experiments than can presently be performed.

The laboratory has been totally refurbished and fulfils L2 standard. A young and vigorous research program aims at developing procedures for deuterium labelling and high density cell culture techniques as well as applying these methods to provide material for in-house studies. Last year 3 EPSRC funded post-docs have been recruited to work on UK based projects involving deuteration and neutron diffraction. We are optimizing labelling strategies for over-expressed recombinant proteins and DNA, primarily in *E. coli* and are testing the feasibility of alternative labeling strategies.

As part of the in-house research activity we aim to characterise and evaluate the response of *E. coli* to deuterated environments using proteomic techniques.

Via a peer review procedure external users have access to the facilities, equipment and in-house expertise necessary to support and develop their own deuteration projects.

Likely Future Directions in User Software

Dr Andrew Peter Hammersley

ESRF, BP 220, Grenoble 38043 CEDEX, France

The past and present state of scientific reduction, analysis, and visualisation software will be briefly reviewed. Some possible future directions will be suggested, and a joint ESRF / CCP13 "proto" project for data acquisition, on-line visualisation, and first look data reduction will be presented.

In situ X-ray studies of the mechanism of muscle myosin

Malcolm Irving¹, Massimo Reconditi², Marco Linari², Leonardo Lucii², Alex Stewart³, Yin-Biao Sun¹, Peter Boesecke⁴, Theyencheri Naraynan⁴, Tom Irving⁵, Gabriella Piazzesi², and Vincenzo Lombardi².

1. King's College London
2. University of Florence
3. Brandeis University, Waltham, MA
4. European Synchrotron Radiation Facility, Grenoble
5. Advanced Photon Source, Argonne.

The regular repeat of myosin motors in each half of a bipolar filament produces an X-ray interference effect that allows their axial motions to be followed in an intact

muscle fibre with a precision of about 1Å. We used this effect to measure the unitary working stroke of myosin motors *in situ*, as they pull the actin filaments towards the centre of the myosin filament during muscle shortening (Reconditi *et al. Nature* **428**, 578, 2004). To eliminate axial motions associated with the compliance of the filaments, the load was held constant. At low load (0.25 times the isometric force) the average working stroke was 12 nm, consistent with crystallographic studies. The working stroke was smaller and slower at higher load.

Low-angle X-ray Diffraction Studies of Muscle using the SRS, ESRF and APS

John M. Squire¹, Carlo Knupp^{1,2}, Manfred Roessle³, Hind A. AL-Khayat¹, Michael K. Reedy⁴, Thomas C. Irving⁵, Felicity Eakins¹ & Jeff Harford^{1,6}

1. Biological Structure & Function Section, Biomedical Sciences Division, Faculty of Medicine, Imperial College London, Exhibition Road, London SW7 2AZ
2. School of Optometry and Vision Sciences, University of Cardiff, Cardiff CF10 3NB, Wales
3. ESRF, 6 rue Jules Horowitz, 38000 Grenoble, France
4. Dept of Cell Biology, Duke University, Durham, NC 27710, USA
5. BioCAT, Dept. Biological, Chemical and Physical Sciences, Illinois Institute of Technology, Chicago, IL 60616, USA
6. Biological Sciences Department, Faculty of Life Sciences, Imperial College London, Exhibition Road, London SW7 2AZ

The highly ordered but different striated muscles found in certain vertebrates, such as bony fish, and in some invertebrates, such as the insect asynchronous flight muscles in the giant water bug *Lethocerus*, provide enormously rich low-angle X-ray diffraction patterns which in some cases can be fully 'solved' to yield the dispositions of some of the component molecules in the muscle sarcomeres (Hudson *et al.*, 1997; Squire *et al.*, 1998, 2003(a-d); AL-Khayat *et al.*, 2003). Analysis of the diffraction patterns from resting muscle has already shown that the myosin head shapes and distributions on the myosin filament surfaces in these two muscle types are different, but they both contrive to place the motor (catalytic) domains of some of the outermost myosin heads in a configuration that is almost what is needed for direct attachment of the heads to the adjacent actin filaments. New results from bony fish muscle using the very small and highly collimated X-ray beam on line ID-02 at the ESRF in Grenoble (Squire *et al.*, 2004) reveal the presence of numerous hitherto unseen X-ray reflections. These promise to provide information not just about the myosin heads, but also

about other components of the muscle A-band, namely C-protein (MyBP-C; Squire et al., 2003c) and titin (Connectin) on the myosin filaments, and troponin on the actin filaments. In addition, time-resolved X-ray diffraction studies can help to reveal the sequence of events that takes place on the onset of activation of an intact muscle and the nature of the structural changes that may be involved in force generation. The latest X-ray diffraction results on these two muscle systems will be reported and preliminary interpretations given.

References

- AL-Khayat, H.A., Hudson, L., Reedy, M.K., Irving, T.C. & Squire, J.M. (2003) "Myosin head configuration in relaxed insect flight muscle: X-ray modelled resting crossbridges in a pre-powerstroke state are poised for actin binding." *Biophys. J.* 85, 1063-1079.
- Hudson, L., Harford, J.J., Denny, R.J. & Squire, J.M. (1997) "Myosin head configurations in relaxed fish muscle: resting state myosin heads swing axially by 150Å or turn upside down to reach rigor". *J. Mol. Biol.* 273, 440-455.
- Squire, J.M., Cantino, M., Chew, M., Denny, R., Harford, J.J., Hudson, L. & Luther, P.K. (1998) "Myosin rod packing schemes in vertebrate muscle thick filaments" *J. Struct. Biol.* 122, 128-138.
- Squire, J.M., Knupp, C., AL-Khayat, H.A. & Harford, J.J. (2003a) "Millisecond time-resolved low-angle X-ray diffraction: a powerful, high-sensitivity technique for modelling real-time movements in biological macromolecular assemblies." *Fibre Diffraction Review* 11, 28-35.
- Squire, J.M., AL-Khayat, H.A., Harford, J.J., Hudson, L., Irving, T.C., Knupp, C., Mok, N-S. & Reedy, M.K. (2003b) "Myosin filament structure and myosin crossbridge dynamics in fish and insect muscles." In 'Molecular and cellular aspects of muscle contraction' (Ed. H. Sugi). Kluwer/ Plenum (in press)
- Squire, J.M., Luther, P.K. & Knupp, C. (2003c) "Structural evidence for the interaction of C-protein (MyBP-C) with actin and sequence identification of a possible actin-binding domain." *J. Mol. Biol.* 331, 713-724.
- Squire, J.M., AL-Khayat, H.A., Harford, J.J., Hudson, L., Irving, T., Knupp, C. & Reedy, M.K. (2003d) "Modelling muscle motor conformations using Low-angle X-ray diffraction". *IEE Proc. BioNanotechnology* (in press).
- Squire, J.M., Roessle, M. & Knupp, C. (2004) "New X-ray diffraction observations on the structure of the vertebrate muscle A-band with possible interpretations based on C-protein (MyBP-C), titin, nebulin and troponin" (*J. Mol. Biol.* - in preparation).

SANS studies of the subunit structure of type I restriction-modification (R-M) enzymes

P Callow^{1,2}, G Kneale³, P.A. Timmins⁴

1. Deuteration Laboratory, ILL, 6 rue Jules Horowitz, BP 156, 38042 Grenoble Cedex 9, France
2. Lennard-Jones Laboratories, School of Chemistry & Physics, Keele University, Staffordshire ST5 5BG, UK
3. University of Portsmouth, School of Biological Sciences, King Henry Building, King Henry I Street, Portsmouth, PO1 2DY, UK
4. Large Scale Structures Group, ILL, 6 rue Jules Horowitz, BP 156, 38042 Grenoble Cedex 9, France

Type I restriction-modification (R-M) systems comprise 3 genes, one for each of the subunits (S, M and R) that are responsible for specificity, methylation and restriction respectively. Two genes (M and S) are required to form the trimeric 160kDa methyltransferase (MTase), M₂S, that methylates a specific base within the recognition sequence and protects the DNA from cleavage by the endonuclease.

The way in which the S domains are organised to interact with the two M subunits, and with the DNA recognition sequence, is of considerable interest. A model has been proposed in which the domains adopt a novel circular arrangement with the N- and C-termini in close proximity, leading to a pseudo-two fold rotation axis in the Mtase.

An expression system has now been established to produce the cloned subunits of the DNA methyltransferase M.AhdI, and have found conditions whereby the subunits can be combined to form an active enzyme. Deuteration of individual subunits has now been successfully performed at the Deuteration Laboratory at the ILL. Reconstitution of the methyltransferase with selectively perdeuterated subunits enables us to carry out small angle neutron scattering experiments, making use of contrast variation, to observe the movement of the labelled subunits following the interaction with its specific DNA recognition sequence.

"Report from CanSAS-IV"

S.King

ISIS Spallation Neutron Source, Rutherford Appleton Laboratory, Chilton, DIDCOT OX11 0QX, U.K.

The 4th CanSAS (Collective Action for Nomadic Small-Angle Scatterers) Workshop took place at the Rutherford

Appleton Laboratory, UK, May 12 - 14, 2004.

CanSAS is an "umbrella forum" under which SAS beam line scientists and technical support staff, scientific software developers, and interested SAS experimentalists can meet and exchange views and ideas on the many and varied aspects of small-angle scattering; from experiment design and control to data reduction and analysis. A particular focus of CanSAS is the development of a standardised SAS data file format.

This presentation will give an overview of what was presented and discussed at CanSAS-IV, and the implications for CCP13.

Flexible filamentous virus structures from fiber diffraction

Gerald Stubbs, Lauren Parker, Justin Junn, Amy Kendall

Center for Structural Biology, Vanderbilt University,
Nashville, TN 37232, USA.

Potexviruses and potyviruses are flexible filamentous plant viruses, of great importance in virology, biotechnology, and agriculture. Fiber diffraction patterns had been obtained from oriented sols and dried fibers of potexviruses by earlier researchers, but no fiber diffraction patterns have been reported for potyviruses, and the published potexvirus diffraction patterns have been far less ordered than, for example, the well-known patterns from the rigid rod-shaped tobacco mosaic virus.

We have been able to obtain very good fiber diffraction patterns from oriented sols of the potexviruses potato virus X (PVX) and narcissus mosaic virus (NMV), and we have obtained diffraction from the potyvirus wheat streak mosaic virus (WSMV), which, although limited, is nevertheless much better than anything previously observed.

Oriented sols are prepared by slow centrifugation in capillary tubes, followed by exposure to strong (up to 18.8 Tesla) magnetic fields. This procedure has produced excellent specimens of PVX and NMV. Diffraction data collected at the BioCAT beamline at APS, Argonne, have enabled us to determine the symmetry of PVX, and to demonstrate the presence of deep intersecting grooves in the viral surface. Because of small differences in the symmetry of the different potexviruses, data from NMV have allowed us to determine the inner and outer radii of the virion and a probable location of the genomic RNA. Diffraction from WSMV sols has allowed us to determine a probable symmetry for this virus.

Detailed structure determination of the intact viruses will

probably require both the fiber diffraction data and high-resolution crystallographic structure determination of isolated coat proteins. Experiments directed toward these goals are in progress.

Virus structure research supported by NSF grant MCB-0235653 and USDA grant 2003-01178. Fiber diffraction methods research supported by NSF Research Coordination Network grant MCB-0234001. Use of the APS supported by the U.S. Department of Energy under contract W-31-109-ENG-38. BioCAT is a NIH-supported Research Center RR-08630.

Time-resolved X-ray Diffraction Experiments on Muscles using "High-flux" Beamline at SPring-8

N. Yagi, H. Iwamoto and K. Inoue

SPring-8/JASRI

A beamline for very high flux (BL40XU) has been built at SPring-8, which is based on a helical undulator and two focusing mirrors. This beamline provides a flux more than ten times higher than any other beamline that has been used for muscle diffraction experiments. At present, three different types of muscle experiments are carried out at this beamline. (1) Experiments on whole frog skeletal muscle, which are made at a time resolution of up to 0.5 msec using a CCD-based framing X-ray detector. (2) Experiments using caged compounds: an array of single skinned fibers is used as a specimen. (3) Time-resolved diffraction experiments on a whole mammalian heart.

The X-ray flux is high enough to record an intensity change of the third-order meridional reflection from the thick filament in frog skeletal muscle at 0.5-msec time resolution in a single quick-release experiment. Time course of intensity changes in weak layer-lines from myosin heads was also measured successfully. On the other hand, radiation damage due to the high flux is severe. A hole is found in a muscle after an exposure of 5 msec. Thus, it is necessary to move the muscle rapidly during an exposure in experiments using the high flux.

Analysis of the myosin superlattice in striated muscles

R.P. Millane¹, C.H. Yoon¹, J.R. Maclaren¹,
J. Chen¹, P.J. Bones¹

P.K. Luther² and J.M. Squire²

1. Department of Electrical and Computer Engineering,
University of Canterbury, Christchurch, New Zealand

2. Biological Structure & Function Section, Biomedical
Sciences Division, Faculty of Medicine, Imperial College
London, Exhibition Road, London SW7 2AZ

Luther and Squire observed many years ago that vertebrates possess two classes of underlying muscle ultrastructure in which the packing of the myosin filaments is different. In bony fish muscles the filaments are in rotational register in each myofibril, whereas in most other vertebrate muscles they adopt one of two opposite orientations in a semi-random arrangement. This latter arrangement is referred to as the myosin superlattice. The two different kinds of myosin packing likely lead to functional differences in myosin-actin interactions, but of particular importance in the context of fibre diffraction analysis of muscle structure is the effect of the superlattice packing on fibre diffraction patterns.

In order to model X-ray diffraction from muscle specimens, an accurate statistical description of the superlattice disorder is required. Fortunately, the superlattice can be observed directly using electron microscopy methods developed by Luther and Squire. Methods for automated analysis of the myosin orientations in such micrographs will be described. Data from images of a number of muscle samples have been used to parameterise the disorder in these samples.

Hierarchical Deformation Mechanisms in Collagen and Wood

Peter Fratzl

Max-Planck Institute of Colloids and Interfaces, Department
of Biomaterials, 14424 Potsdam, Germany.

Collagen and wood are fully polymeric biological tissues with remarkable mechanical properties. Details on the deformation mechanisms can be determined by tensile testing and simultaneous synchrotron X-ray diffraction. This in-situ methodology allows to follow deformation processes at several levels of the tissues hierarchical structures. It turns out that collagen fibrils are stretching more than the molecules they are composed of. The whole tissue stretches even more than the fibrils, by an amount depending on the strain rate. This indicates a vis-

coelastic shear coupling between fibrils mediated by a matrix of mostly proteoglycans and water. In wood, cellulose microfibrils are wound helically around the lumen of tube-like cells, which are shown to react to tension like elastic springs. Again, the stiff cellulose fibrils are shear coupled via a matrix, which in this case consists of hemicelluloses reinforced with lignin.

Fibre Diffraction from Poly-Alanine and Poly-Glutamine Assemblies

Kirschner DA¹, Shinchuk LM¹, Sharma D¹,
Reixach N², Blondelle SE², Wetzel R³, and
Inouye H¹

1. Department of Biology, Boston College, Chestnut Hill,
MA 02467-3811

2. Torrey Pines Institute for Molecular Studies, San Diego,
CA 92121

3. Graduate School of Medicine, University of Tennessee,
Knoxville, TN 37920

Pathological accumulation of fibrillar, proteinaceous amyloid deposits can occur in a variety of neurodegenerative diseases, two well-known ones of which are Alzheimer's disease and the transmissible spongiform encephalopathies. In these two examples the misfolded protein or protein fragment (amyloid β and prion, respectively) has a heterogeneous sequence. By contrast, in two additional examples where fibrillar amyloid can accumulate-Huntington's disease (HD) and oculopharyngeal muscular dystrophy (OPMD)-polypeptide homopolymers underlie the fibrillar assembly. In HD, glutamine trinucleotide expansion to $>(CAG)_{35-40}$ results in misfolded proteins (poly-Glutamine_n, or polyGln_n) that may manifest a toxic gain-of-function. Besides HD, there are at least eight other inherited neurodegenerative diseases caused by polyGln expansions. In OPMD, which is an adult-onset disorder, alanine trinucleotide expansion from $(GCG)_6$ to $(GCG)_{8-13}$ in the poly(A) binding protein 2 (PABP2) gene leads to accumulation of intranuclear, 85 Å-wide filaments. To explore how polyGln aggregate structure may depend on expansion length, and how fibril formation may form from expanded polyAla sequences, we are investigating with X-ray fiber diffraction the structures of assemblies formed by synthetic acetyl-Gln₈-amide, Asp₂Gln₁₅Lys₂, Lys₂Gln₂₈Lys₂, and Lys₂Gln₄₅Lys₂, and by peptides having 7, 11, 13 and 20 Ala residues.

Structural Studies at ESRF on Silk Formation by SAXS/WAXS techniques

Christian Riekell

European Synchrotron Radiation Facility, B.P.220, F-38043 Grenoble Cedex France

Silk fibres are produced in nature by spiders or silk worms from liquid crystalline protein solution. Details of the fibre formation by in-situ experiments are currently largely unknown. I will review in my talk the present status of SAXS/WAXS experiments on silk formation using the ID02 and ID13 beamlines of the ESRF. In-situ micro-SAXS/WAXS experiments during silking of live spiders at the ID13 beamline showed the presence of a thread in the immediate vicinity of the spigots but not the onset of fibre formation. Complimentary SAXS/WAXS experiments have therefore been performed during shearing of regenerated *Bombyx mori* silk using Couette cell geometry at the ID02 beamline. These experiments show the evolution of fibroin molecular shape during shearing and an aggregation into an amorphous material at the highest shearing rates. The aggregated material is capable of crystallizing into β -sheet containing silk II during drying. Scanning micro-SAXS/WAXS at ID13 on partially dried material shows the coexistence of silk II with an intermediary hydrated silk I type phase.

Non Crystalline Diffraction on Diamond - I22 and beyond

N.J. Terrill[†], A.F. Grant^{*}, A.R. Marshall[†], A.D. Smith^{*}, K.J. Sawhney[†],

[†] Diamond Light Source, Rutherford Appleton Laboratory, Chilton, Didcot, Oxfordshire, OX11 0QX, UK

^{*}CCLRC Daresbury Laboratory, Daresbury, Warrington, Cheshire, WA4 4AD, UK

Non-Crystalline Diffraction is an important method for studying the structural properties of non- or semi-crystalline states of matter. These include biological macromolecules e.g. fibres or proteins and their complexes in solution, synthetic polymers, gels, liquid crystals, oils, paints, ceramics and environmental aggregates. The technique yields information on the shape and size of these molecular assemblies and is particularly sensitive to phase changes or conformational rearrangements on a length scale ranging from 10 to 10000 Å.

Diamond is the new third generation synchrotron source that is currently being designed and constructed for the UK Science community. The 3GeV machine will begin operations in 2006 with commissioning of the first seven

beamlines to follow.

The requirements to meet the scientific and technological challenges of the next decade are for a high resolution, high brightness beamline. These can only be provided by an undulator insertion device on a 3rd generation synchrotron radiation light source. I22, served by a U25 in vacuum undulator will deliver high photon flux (1×10^{14} ph/s/0.1%b.w.) into a focused $300 \times 75 \mu\text{m}$ spot ($1 \times 1 \mu\text{m}$ with microfocussing) in the energy range 4-20keV. The End Station with associated linear and area detectors for static and time resolved measurements will be capable of recording the scattered radiation from samples contained in purpose designed specialised environmental cells. The end station's modular arrangement will allow a choice between small angle scattering for large fibrous structures or microfocus illumination each with a wide angle scattering option for materials studies. The latest developments in design for the beamline will be described.

The main points of the interim report on a "SAXS Roadmap" for Diamond will also be discussed.

Micro-scale Polymer Processing: using scattering techniques to investigate polymer processing

E.L. Heeley^a, C.M. Fernyhough^a, T. Gough^b, W. Bras^c, A. J. Gleeson^d & A. J. Ryan^a.

a. Department of Chemistry, University of Sheffield, Sheffield, S3 7HF, UK

b. IRC in Polymer Science and Technology, School of Engineering, Design and Technology, University of Bradford, Bradford BD7 1DP, UK

c. Dubble CRG, ESRF, B.P. 220, F-38043 Grenoble Cedex, France

d. Daresbury laboratory, Daresbury, Warrington, Cheshire, WA4 4AD, UK

Following crystallization in semi-crystalline polymers such as polyethylene and polypropylene, can be achieved by using simultaneous Small- and Wide -Angle X-ray scattering (SAXS/WAXS) techniques. Here, SAXS probes the long-range order or macrostructure providing details of the lamellar spacing and WAXS gives information concerning the atomic ordering or microstructure of the system. Following the structure development (crystallization) in polymers is particularly important as this process leads to the stabilisation of the final product, influencing the aesthetic and mechanical properties of the material. Thus, to produce useful materials it is essential to understand and predict the crystallization process,

which can be explored with a variety of scattering experiments.

Several, experiments, which allow us to follow the crystallization in polymers have been performed using synchrotron radiation sources. Quiescent and shear -induced crystallization of samples have been studied using time resolved SAXS/WAXS on various beamlines at the Daresbury SRS and the ESRF. Here, we show how recent beamline developments with improved experimental techniques, can give an insight in to mechanisms of early crystallization kinetics as well as the final crystalline morphology. For example, quiescent crystallization experiments have been performed using an in-situ DSC instrument on the Dubble -CRG station at the ESRF and 8.2 plus the new MPW station 6.2 at Daresbury SRS. This has allowed comparisons of SAXS/WAXS data to be made specifically, concerning new improvements made in detector technology, which have revealed information on the very early crystallization process. Shear-induced crystallization has also been investigated using SAXS/WAXS again on Dubble and station 16.1 at the Daresbury laboratory. An *in-situ* shearing devices and an online extruder, has provided an insight into crystallization under the influence of flow. Finally, experiments involving simultaneous SAXS/WAXS and rheology have been performed on station ID2 at the ESRF. This unique set-up allows time resolved SAXS/WAXS data along with the rheological responses of the polymer to be obtained throughout the crystallization process.

All these techniques are currently being used to investigate the crystallization of commercial and novel polymer systems. The use of time resolved synchrotron radiation is an invaluable technique in probing such processes and his will enable us to expand our understanding of crystallization kinetics with relevance to industrial processing procedures. This is envisaged to give a better understanding of polymer processing towards improved materials for the future.

Real-time investigation of protein kinetics using small-angle neutron scattering on instrument D22 at the ILL

R.P. May

Institut Laue-Langevin, BP 156, F-38042 Grenoble Cedex 9, France

The high neutron flux (10^8 neutrons/cm² s) and the specific sample environment equipment available at the small-angle scattering instrument D22 of the Institute Laue-Langevin allow one to perform time-resolved measurements down to frame lengths of the order of 10 ms. Overall times per frame of about 10 to 100 s are required to achieve sufficient counting statistics per frame. These

are obtained by repeating the measurement cycles a sufficient number of times.

Examples of experiments performed so far include the observation of the formation of complexes between DNA and cationic vesicles with a stopped-flow device, chasing experiments with chaperones (E. coli GroEL), and light-flash activation of photo-active yellow protein.

We expect that with the installation of a new time-resolving high-count-rate (> 2MHz at 10% dead time) detector, investigations in particular of smaller proteins will be further facilitated.

Time-resolved X-ray diffraction patterns from indirect flight muscles in living *Drosophila* during tethered flight

Tom Irving¹, Michael Dickinson², Gerrie Farman¹, Mark Fry², David Maughan³

1. BioCAT, Dept. BCPS, Illinois Institute of Technology, Chicago IL 60616, USA

2. Dept. Bioengineering, California Institute of Technology, Pasadena CA 91125, USA

3. Dept. Molecular Physiology & Biophysics, U. Vermont, Burlington VT 06505, USA

The indirect flight muscles (IFM) of insects provide a particularly well-ordered system for structural studies directed at understanding the molecular mechanisms underlying muscle physiology. The fruit fly, *Drosophila*, with its rich set of tools for genetic manipulation, is a widely used model system for integrative biology. Here I report the results of time-resolved x-ray diffraction experiments on the dorsal longitudinal flight muscles (DLM) of adult flies during tethered flight at the BioCAT beam line at the Advanced Photon Source. Detailed 2D x-ray diffraction patterns were collected at rest and at 8 350 microsecond time frames equally spaced in the ~5 ms wing beat cycle. The results provide convincing evidence for cyclical attachment and detachment of force producing myosin molecules to its binding sites on actin in a living organism. Implications and future directions will be discussed.

X-ray Fibre Diffraction Analyses of Myosin Filaments in Resting and Contracting Skeletal Muscles

Katsuzo Wakabayashi, Kanji Oshima, Masaki Ogino and Yasunori Takezawa

Division of Biophysical Engineering, Graduate School of Engineering Science, Osaka University, Toyonaka, Osaka 560-8531, Japan

X-ray fibre diffraction has for many years played a key role in studying the molecular mechanism of muscle contraction because it has an ability to investigate muscle structures under physiological conditions at the relevant timescale.

X-ray fibre diffraction analyses of the thick myosin filament have been made to elucidate the structure of the two-headed crossbridges in the resting and isometrically contracting states of live skeletal muscle. In the resting state of skeletal muscle, there are rich of layer-line reflections as well as meridional reflections arising from thick myosin filaments, and during contraction, the most of the layer lines are much weakened but the principal meridional reflections are still retained with strong intensity. These myosin-based reflections are partially affected by the lattice structure of a hexagonal filament array in a sarcomere. In the analysis of the resting structure, the cylindrically symmetrical Patterson function $\Delta Q(r,z)$ based on only the layer-line intensity data except those on the equator (Namba, Wakabayashi & Mitsui: JMB, 138, 1-26 (1980)) was used. By removing the interfilament vectors, the $\Delta Q(r,z)$ was inversely transformed to get the interference-free intensity function $I(R)$. The modelling of the two-headed myosin crossbridge was performed to obtain the best-fit to the obtained single-filament intensities.

In the second approach, the meridional reflections that correspond to the mass density projected onto the fibre axis were analysed. The meridional reflections are also heavily sampled by the hexagonal filament array. The sampling effect was markedly reduced during contraction and the reflection widths are radially broadened. The intensity data in the contracting pattern were corrected for such a radial broadening. It has been suggested that the existence of an axial perturbation of the crossbridge repeat generates a series of the reflections indexed to a basic repeat of 43 nm on the meridian, forming a triplet structure of the crossbridge arrangement (14.3 nm x 3). Modelling analysis of the myosin-based meridional reflections was made to derive the more precise crossbridge periodicity and the axial disposition of the two-headed crossbridges.

In the first approach, we could successfully remove the contributions of interfilament vectors from the $\Delta Q(r,z)$

function obtained from the observed intensity data. The resulting $I(R)$ functions were very similar to those obtained from the muscle at non-overlap length of the thick and thin filaments in the sarcomere, where the interference effect was greatly reduced. Modeling results indicated that in the resting state the two heads of a myosin crossbridge are axially separated by about 8 nm and are helically arranged at the radius of 13.5 nm with their curved surface surrounding the filament backbone. The second approach revealed that the myosin filament has a mixed structure of two different periodicities and axial dispositions of the two-headed crossbridges. These features were altered when muscle went from the resting to the contracting state. The crossbridge arrangement consisted of the two regions: in the resting state the crossbridge repeat in the regular region was 14.3 nm and in the perturbed region the repeating unit consisted of three crossbridge repeats slightly deviated from a 14.3 nm-separation. In both the regular and perturbed regions, two myosin heads of a crossbridge were axially separated and tilted against the plane perpendicular to the filament axis. The arrangement of two heads of a crossbridge was different in the regular and perturbed regions. In the contracting state, the disposition of the two-headed crossbridge was altered towards a more perpendicular orientation to the filament axis in the regular and perturbed regions. In the regular region the crossbridge repeat was 14.5 nm and in the perturbed region the basic repeat was 43.5 nm with different triplet repeats.

Reorientation behaviour of smectic liquid crystals due to external fields

W. Bras

DUBBLE CRG @ ESRF, BP 220 F-38043 Grenoble Cedex, France

The reorientation behaviour of smectic liquid crystals due to externally applied forces is at present not very well understood. The interest in these systems lies in the fact that for several classes of smectic liquid crystals it is not necessary to achieve a full 90 degree rotation in order to achieve a 90 degree rotation of the optical axes. This could lead to faster switching displays.

Time-resolved SAXS experiments are a tool that can be used to study such systems. The conventional method of applying electric fields to induce and change orientation is less suitable for diffraction experiments since the alignment axis is not necessarily parallel to the magnetic field nor does the induced electric dipole have a linear relation with the applied field. To overcome these problems we have decided to utilise magnetic fields. Samples were rotated in a 7 Tesla field. The reorientation mechanism that follows is rather complicated and it is shown that

there are several competing pathways for the molecules to realign themselves with the field.

Analytical Model of Fibre Diffraction Layerlines with Bent Baselines

Jianpeng Ma

Department of Biochemistry and Molecular Biology, Baylor College of Medicine, Houston, TX77030

An analytical model for Fourier transformation of a filament with bent baseline was developed. The transformed fibre diffraction layerlines were derived with multiple convolution theory. The theoretical diffraction patterns were calculated for continuous bent helix, discontinuous bent helix, and real filamentous molecules. The method was applied to refine the atomic model of F-actin against the experimental fiber diffraction data. The results were compared with those refined using long-range normal modes in our previous study (Biophys. J. 86, 116 (2004)). Decreases of R-factors were observed and the agreement between the analytical and normal-mode-based models indicates the feasibility of the analytic model. Finally, the advantages of the analytical model and the potential future improvements were discussed.

Fibre Diffraction from Carbon Nanotubes

Jane Crawshaw and Alan Windle

Department of Materials Science and Metallurgy, University of Cambridge, Pembroke Street, Cambridge, CB2 3QZ, UK

We are interested in using fibre diffraction techniques to study ordered assemblies of carbon nanotubes. To this end I am writing computer programs to predict X-ray fibre diffraction patterns from such structures, looking at packing and the effects of misorientation in the first instance. The calculations use helical diffraction theory to calculate the structure factor of carbon nanotubes as reported by Lucas et al (Scanning Microscopy Vol. 12, No. 3, 1998, 415-436).

Real-Time SANS Study of Transient Phases in Polymer Crystallization

X. B. Zeng,* G. Ungar,* S.J. Spells,† S. King‡

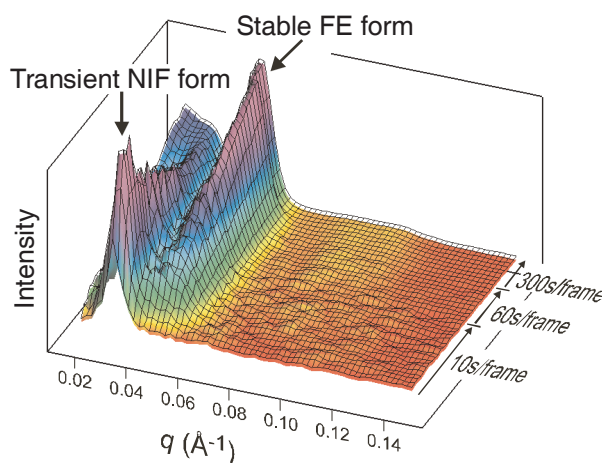
* Department of Engineering Materials, Sheffield University, Sheffield S1 3JD, UK

† Sheffield Hallam University, City Campus, Sheffield S1 1WB, UK

‡ ISIS, Rutherford Appleton Laboratory, Chilton, Didcot OX11 0QX, UK

Small angle neutron and X-ray scattering techniques (SANS and SAXS) are a powerful combination in studying structural details of semicrystalline polymer structure using ultralong linear alkanes with deuterated chain ends as models.¹

Currently, SAXS data with a reasonable signal-to-noise ratio can be collected in sub-second frames by using synchrotron radiation. This makes real-time SAXS suitable for studies of the crystallization process, transient phases, and solid-state transformation in polymer and low-molecular systems. It would be desirable to carry out SANS experiments in real time as well. Although SANS normally requires exposure that are considerably longer (usually hours), in this study it is demonstrated that good quality data can be collected in no more than 10 seconds (see figure below), provided a rational approach is adopted to selected deuteration. We present here the first real-time SANS study of the crystallization process of a model polymer system. The compounds were selectively deuterated so as to maximize the SANS contrast. A T-jump cell is used, capable of rapid cooling of a large sample from melt to the crystallization temperature. This development opens a new way of using neutron scattering in studies of materials under industrial processing conditions.



Real-time SANS spectra recorded during isothermal crystallization of a monodisperse long n-alkane with deuterated chain ends: $C_{12}D_{25}C_{192}H_{384}CHDC_{11}D_{23}$.

Crystal structure of native cellulose - Complementary X-ray and neutron experiments

Martin Müller

Institut für Experimentelle und Angewandte Physik, der
Universität Kiel, D-24098 Kiel, Germany

Native cellulose displays an allomorphism of a monoclinic and a triclinic form. Most native cellulose in plants are a mixture of the two allomorphs. Growth stress might favour one of the two forms. In tension wood fibres of poplar trees the monoclinic crystal form is dominant. The high orientation of the cellulose microfibrils in tension wood fibres makes it possible to collect diffraction data with a resolution of 1.1 Å. Complementary X-ray and neutron data can be used to determine the hydrogen atom positions and, thus, the hydrogen bond network in native cellulose.

Poster Abstracts

SAXS/WAXS data acquisition and reduction programs at ESRF beamline ID02 for time-resolved experiments

**Peter Boesecke, Rainer Wilcke, Armando
Sole, Theyencheri Narayanan**

European Synchrotron Radiation Facility (ESRF), F-38043
GRENOBLE CEDEX, France

Data rates from two dimensional detectors at synchrotron radiation beamlines are steadily increasing. An overview of SAXS/WAXS data treatment on the High-brilliance Beamline (ESRF ID02) is presented.

CCD detectors with 1024 x 1024 pixels and 16 bit data are in routine use for time resolved experiments. Today, up to 14 images per second can be taken. To facilitate automatic data processing each scattering image is saved together with a descriptive set of parameters. The data storage is done inside the framework of the ESRF data format. The use of the bsl format is disliked because it does not provide enough possibilities to include all required information. The data reduction can either be done offline, using the traditional command line based programs of ID02 ("saxs"), or online, using a newly developed program package ("online-saxs").

All detectors require various corrections before the measured intensities are available in absolute differential scattering cross-sections. The data reduction includes the correction of detector artifacts such as dark current, image distortion and spatial inhomogeneities, as well as normalization of intensities to incident photon flux, sample

transmission and spherical angle.

The programs are also used on other ESRF beamlines, e.g. at the anomalous scattering beamline ID01. They can read bsl data and are available to users. Versions for a number of different platforms (UNIX, LINUX, WINDOWS) are available.

Spatial mapping of collagen fibril organisation in primate cornea

Craig Boote, Sally Dennis, Keith M. Meek

School of Optometry and Vision Sciences, Cardiff
University, Redwood Building, King Edward VII Avenue,
Cardiff CF10 3NB, Wales, UK

WAXS methods were used to map the fibrillar arrangement and distribution of collagen over 3 common marmoset corneas, at 0.5 X 0.5 mm resolution. The maps provide new insight into corneal structure in the normal marmoset eye, and should aid the interpretation of data from pathological corneas or primate models of refractive surgery. The results indicate the presence of a circumcorneal annulus of highly aligned collagen, 0.5 to 1.5 mm wide, where the cornea and sclera fuse at the limbus; a feature similar to that observed in human tissue. As in humans, the annulus varies in width, fibril angular spread and collagen density around its circumference. Implications for the mechanical properties of the cornea are discussed. More centrally, the marmoset cornea features a preferred lamella orientation in which proportionally more fibrils are oriented along the superior-inferior corneal meridian. This observation is in striking contrast with the situation in the central human cornea, where an orthogonal arrangement of preferentially aligned fibrils dominates. Investigation of a further 16 corneas confirmed that approximately 33% (+/- 1%) (n = 76) of fibrils in the central marmoset cornea lie within a 45-degree sector of the superior-inferior meridian. These observations may help to explain the difference in corneal birefringence between humans and monkeys.

Time course of formation of myosin cross-bridges and rise of a parallel elasticity measured by X-ray diffraction in tetanized single fibres from frog muscle

Elisabetta Brunello^{1,2}, Pasquale Bianco¹, Massimo Reconditi^{1,2}, Marco Linari^{1,2}, Pierre Panine³, William Helsby⁴, Gabriella Piazzesi¹, Malcolm Irving⁵ and Vincenzo Lombardi^{1,2}

1. University of Florence, Florence, Italy
2. Istituto Nazionale di Fisica della Materia OGG, Grenoble, France
3. ESRF, Grenoble, France
4. CRLC, Daresbury, United Kingdom
5. King's College London, London, UK

Two-dimensional X-ray patterns from intact skeletal muscle fibers of *Rana temporaria* (2.1 μ m sarcomere length, 4°C) were recorded with 5ms time resolution using a gas-filled detector (RAPID) at beam line ID02, ESRF, Grenoble, France. Isometric force development was accompanied by an increase of the spacing of the third order myosin meridional reflection (S_{M3}) from 14.34 nm to 14.56 nm (Piazzesi et al., *J. Physiol.* 514:305, 1999). When unloaded shortening (velocity V_0) was imposed 5ms after the start of stimulation, S_{M3} decreased to 14.30 nm during shortening, then increased to 14.56 nm during force development after shortening. When shortening at $1/4 V_0$ was imposed at 55 ms, to maintain a force of half the isometric plateau force (T_0), S_{M3} continued to increase from 14.45 nm to 14.56 nm during shortening, with the same time course as in an isometric tetanus. In contrast, the intensity of the M3 reflection (I_{M3}) during such a shortening period was less than during the same period of an isometric contraction, and was similar to the value observed when shortening at $1/4 V_0$ was imposed from the tetanus plateau. These results suggest that during muscle activation shortening at V_0 , but not at $1/4 V_0$, prevents the formation of force-generating cross-bridges, revealing the rise of an elasticity joining the Z-line with the thick filament (Bagni et al., *Biophys. J.* 82:3118, 2002). This elasticity exerts a compressive force on the thick filament.

Supported by MIUR (Italy), MRC (UK), ESRF, EMBL

SANS studies of the subunit structure of type I restriction-modification (R-M) enzymes

P Callow^{1,2}, G Kneale³, P.A. Timmins⁴

1. Deuteration Laboratory, ILL, 6 rue Jules Horowitz, BP 156, 38042 Grenoble Cedex 9, France
2. Lennard-Jones Laboratories, School of Chemistry & Physics, Keele University, Staffordshire ST5 5BG, UK
3. University of Portsmouth, School of Biological Sciences, King Henry Building, King Henry I Street, Portsmouth, PO1 2DY, UK
4. Large Scale Structures Group, ILL, 6 rue Jules Horowitz, BP 156, 38042 Grenoble Cedex 9, France

Type I restriction-modification (R-M) systems comprise 3 genes, one for each of the subunits (S, M and R) that are responsible for specificity, methylation and restriction respectively. Two genes (M and S) are required to form the trimeric 160kDa methyltransferase (MTase), M2S, that methylates a specific base within the recognition sequence and protects the DNA from cleavage by the endonuclease.

The way in which the S domains are organised to interact with the two M subunits, and with the DNA recognition sequence, is of considerable interest. A model has been proposed in which the domains adopt a novel circular arrangement with the N- and C-termini in close proximity, leading to a pseudo-two fold rotation axis in the Mtase.

An expression system has now been established to produce the cloned subunits of the DNA methyltransferase M.AhdI, and have found conditions whereby the subunits can be combined to form an active enzyme. Deuteration of individual subunits has now been successfully performed at the Deuteration Laboratory at the ILL. Reconstitution of the methyltransferase with selectively perdeuterated subunits enables us to carry out small angle neutron scattering experiments, making use of contrast variation, to observe the movement of the labelled subunits following the interaction with its specific DNA recognition sequence.

The Fibrillar Arrangement and Distribution of Collagen in Normal and Keratoconus Corneas

S.Dennis, Y.Huang, S.Tuft, C.Boote,
K.Meek

Department of Optometry and Vision Sciences, Cardiff
University, Cardiff, UK

Department of Ophthalmology, Great Wall Hospital,
Beijing, China

Moorfields Eye Hospital, London, UK

Purpose: To examine the distribution and the preferred fibril orientation of collagen in the normal human cornea and in corneas with the disease keratoconus and to relate any observed variations to features on corneal surface topography maps.

Methods: Keratoconus corneal buttons of 8mm diameter (n 4) and normal human corneas (n 3) were tagged with a nylon suture at the 12 o'clock position, before being preserved in formaldehyde. For each cornea a videokeratographic image of surface dioptric power was recorded (in vivo for keratoconus corneas and in vitro for the normal controls). Wide angle x-ray scattering (WAXS) patterns were obtained at 0.4mm intervals over the entire area of each sample using a computer operated translation stage on Station 14.1 at the Daresbury Synchrotron Radiation Source, UK. Each WAXS pattern was analysed to produce quantitative information regarding the total amount of collagen (aligned and isotropic), the preferred orientation of aligned collagen and the ratio of aligned to total collagen at a known corneal location. By arranging the data onto a grid of corneal position various maps were produced to illustrate the distribution and preferential orientation of collagen. The relationship between collagen arrangement and surface topography was examined in detail for both the normal and keratoconus corneas.

Results: In the cone region of keratoconus corneas the orthogonal preferred orientation of collagen fibrils that is seen in the normal human cornea, is absent. In the normal cornea there is a gradual symmetrical increase of collagen from the central region to the periphery. However, in keratoconus corneas maximal thinning occurs at the apex of the cone. Outside the cone region the increase in collagen occurs asymmetrically and is less gradual than in the normal cornea. The distribution of aligned collagen is especially altered in keratoconus corneas and appears to correlate closely with cone shape.

Conclusion: The results indicate a redistribution of collagen in keratoconus corneas, which supports the theory that corneal thinning in keratoconus occurs as result of lamella sliding away from the cone region. The existence

of this mechanism would also help to explain the altered orientation of collagen fibrils in this region.

Time Resolved X-ray Diffraction Studies of Active Bony Fish Muscle

Felicity Eakins¹, Carlo Knupp^{1,2}, Christian Pinali² and John M. Squire¹

1. Biological Structure and Function Section, Biomedical Sciences Division, Imperial College London, UK and

2. School of Optometry and Vision Sciences, Cardiff University, Cardiff, UK.

X-ray diffraction is a particularly useful tool for studying the mechanisms of muscle contraction. Not only does it provide a wealth of structural data but it can also be used on live intact muscle preparations allowing data to be obtained whilst the muscle undergoes contraction. Bony fish muscle is an extremely good preparation to use for this work because it is very well ordered compared to other vertebrate muscles such as frog, showing long range order and a simple 3-dimensional crossbridge lattice.

Previous work carried out on bony fish muscle has looked at the changes which occur in the X-ray pattern during contraction in conjunction with the tension time course produced by the muscle [Harford & Squire, 1990]. Up until now the effects of any sarcomere length change which might occur during muscle contraction have been neglected. There is evidence for a small, but very fast, change in lattice spacing during contraction and it has been previously argued that, therefore, the sarcomere length change may be small [Harford & Squire, 1992]. However, this needs to be confirmed and if, in fact, the tension time-course is affected by maintaining sarcomere length, then the sarcomere length will need to be controlled.

This poster describes the laser and detector system which has been developed to control the sarcomere length of plaice fin muscles whilst collecting X-ray patterns. It also presents some of the preliminary time-resolved low-angle X-ray diffraction data obtained using this feedback system in experiments on beamline 16.1 at the CLRC Daresbury Synchrotron Radiation Source.

References

- Harford, J.J. & Squire, J.M. (1992). Evidence for structurally different attached states of myosin crossbridges on actin during contraction of fish muscle. *Biophys. J.* 63, 387-396.
- Harford, J.J. & Squire, J.M. (1990). Static and time resolved X-ray diffraction studies of fish muscle. In Squire, J.M. (Ed), *Molecular Mechanisms in Muscular Contraction*. Macmillan Press, 287-320.

New Ionic Polymer Materials for Films. Physico-Chemical Behavior of Carboxyl Containing Acrylic Copolymers: Conformation, Dynamics and Structure Development in Mixed Solvents.

Johan Fundin, Anthony J. Ryan

Department of Chemistry, The University of Sheffield,
Dainton Building, Brook Hill, Sheffield S3 7HF, UK

Introduction

The formation of films from latex materials is well understood and has been explained to take place in several steps [1, 2], whereas film formation from ionic polymer solutions has been less frequently studied. In particular, the film formation process from aqueous solutions of charged polymers needs to be revealed, and the effect of co-solvents on the rheology and final film properties of charged polymers. These phenomena have an impact on performance in hair fixative polymer formulations, water-soluble polymers for non-wovens, solution polymers for glass fiber sizing etc., but also likely starch solutions that film form during application. During the film formation process, water acts as a suspending and stabilizing medium for the macromolecules that allows for thermal motion of the system that allows intermolecular interactions and close packing. Upon drying, water and co-solvent evaporate, leading to concentration of the solute and eventually film formation. The present work is focused on the initial step of structure development, i.e. intermolecular interactions in dilute and concentrated polymer solutions in mixed solvents.

Results and Discussion

Dynamic light scattering (DLS) and small-angle X-ray scattering were employed to study the properties of random copolymers of methacrylic acid (MAA) and butyl-methacrylate (BMA) (M_w approx. 38,000) at various degrees of acidity (MAA content) and at various solvent compositions of isopropanol (IPA) and water. DLS measurements revealed the presence of mainly two dynamic structure factors, one fast diffusive and one slow non-diffusive. The fast mode is attributed to the translational motion of the copolymer chain while the slow mode relates to interpolyion solution correlations that are strongly dependent on the long-range electrostatic forces between anionic MAA units. SAXS results showed that the copolymer chain conformation is elongated. Ionized MAA is soluble in 100% H_2O but insoluble in 100% IPA, while BMA is soluble in 100% IPA but not in 100% H_2O . Thus, these random copolymers are soluble only in mixtures of IPA and H_2O , and only at certain compositions of the two solvents. This delicate feature gives rise to some sophisticated micro- and macroscopic solution properties. The existence of inter-particle aggregation can be controlled by varying the IPA-to-water ratio, an initial step

for the understanding of structure development during film formation.

The interaction potentials between copolymer chains and solvent - in dilute solution - are reported in terms of the hydrodynamic virial coefficient k_D . In line with the enhanced intermolecular association when the IPA/ H_2O ratio is decreased, there is a simultaneous reduction in k_D . Scattering experiments give two results that indicate an elongated macromolecular conformation: *i*) The shape of the pair-distance distribution functions (PDDF) [3]; *ii*) The high values of the particle-shape and internal-density parameter ($= \langle R_G \rangle_Z / \langle R_H \rangle_Z$). The PDDFs at certain IPA/ H_2O compositions are similar to those of cylindrical molecules and give information about a cross-sectional radius R_{CS} and length L (Figure 1).

Figure 2 shows the concentration dependence of the apparent radius of gyration $\langle R_G \rangle_Z$, at different solvent compositions of IPA and H_2O . It is obvious that conformational changes take place as the mass fraction of H_2O is increased, and eventually macroscopic phase-separation occurs. Combination of intra- and intermolecular interactions in selective solvents leads to diverse possible structures of associates, see for instance ref. [4, 5].

Conclusions

When the solvent mass ratio IPA/ H_2O is decreased, the overall solvent quality decreases. There is no pronounced dependence of the mutual diffusion coefficient D_m on copolymer concentration. When present, the dependence is slightly inverse, especially at low IPA/ H_2O ratios. DLS shows mainly two relaxation modes, one fast diffusive mode and one slow non-diffusive describing long-range electrostatic interaction. The slow non-diffusive structure factor vanishes in the presence of salt, supporting the interpretation of electrostatic correlation. When the solvent mass ratio IPA/ H_2O is decreased, the shape factor increases, suggesting a decreased 'surface' stability of the sphere-equivalent macromolecules.

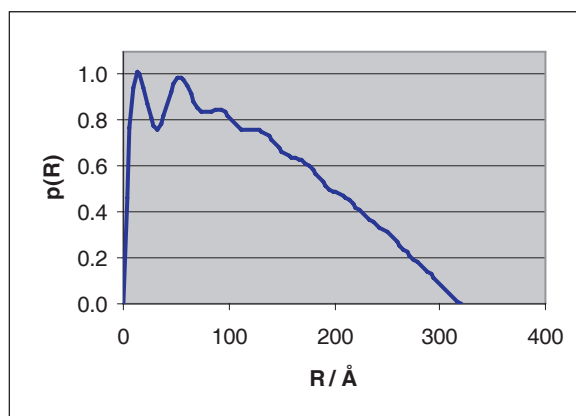


Figure 1. Pair-distance distribution function (PDDF) for 3 wt% MAA-BMA (20/80) in IPA/ H_2O 80/20.

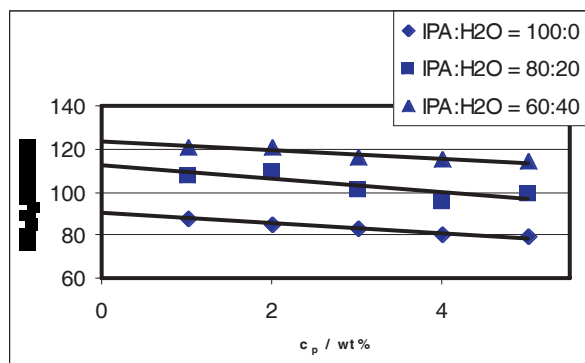


Figure 2. The concentration dependence of $\langle R_G \rangle_z$, app for various IPA/H₂O compositions.

References

- [1] Voyutskii, S. S. Autohesion and Adhesion of High Polymers; Wiley-Interscience: New York, 1963.
- [2] Vanderhoff, J. W; Bradford, E. B; Carrington, W. K. J. Polym. Sci., Polym. Symp. 1973, No. 41, 155.
- [3] Svergun, D. I. J. Appl. Cryst. 1992, 25, 495.
- [4] Itakura, M, Inomata, K, Nose, T. Polymer 2001, 42, 9261.
- [5] Hill, L. W; Wicks, Z. W. Progress in Organic Coatings 1980, 8, 161.

An Investigation into the Crystallisation of PET using AFM and X-Ray Scattering Techniques

C.R.Hurley, E.L.Heeley, G.J.Leggett

Department of Chemistry, University of Sheffield, Sheffield, S3 7HF

Polymer properties are generally customised by changing the monomer structure, however by modifying the manufacturing process more subtle variations or improvements in properties can be achieved. The aim of this investigation is to determine the effect of molecular orientation on the properties of Polyethylene Terephthalate using x-ray scattering and atomic force microscopy.

DSC and x-ray scattering techniques on commercially produced cast PET show that higher annealing temperatures induced a faster crystallisation, with the crystallites having a lower dimensionality of growth. Friction force microscopy has established a non-linear relationship between load and the friction force suggesting Johnson, Kendall and Roberts contact mechanics.

The effect of molecular orientation will be investigated using the Keele drawing camera looking at the extent and rate of the draw. Drawing the polymer aligns the polymer chains and orients the crystallites, while increasing the

overall crystallinity. The extent of these effects will be studied in situ with time resolved x-ray scattering and the polymers produced will be analysed using AFM. The extent of shear will be indicated by the effect this has on the friction force across the surface.

By gaining a thorough understanding of the structure-property relationships of various polymers, there is a possibility in the future for most links in the processing chain to be modelled by mathematical methods. The eventual aim is to use these models to predict the structure and properties of the final product, allowing engineering design experiments to be performed before expensive real materials and machinery are used and produced.

SANS at the ISIS second target station

R.K.Heenan & S.M.King

ISIS Facility, CCLRL, Rutherford-Appleton Laboratory, UK

Construction of a 10Hz "cold neutron" target station for ISIS is under way. An enhanced flux of long wavelength neutrons from an optimised lower power target will enable world class pulsed source instruments to be built. The first SANS instrument will have two 1m square detectors in a 3m diameter, 12m long, vacuum tank. Neutrons of 1.5 to 12 angstrom wavelength will be used by time of flight. This will enable an unsurpassed simultaneous Q range, having good overlap with wide angle diffraction, suitable for a wide range of science.

SANS at the ISIS second target station

R.K.Heenan & S.M.King

ISIS Facility, CCLRL, Rutherford-Appleton Laboratory, UK

Construction of a 10Hz "cold neutron" target station for ISIS is under way. An enhanced flux of long wavelength neutrons from an optimised lower power target will enable world class pulsed source instruments to be built. The first SANS instrument will have two 1m square detectors in a 3m diameter, 12m long, vacuum tank. Neutrons of 1.5 to 12 angstrom wavelength will be used by time of flight. This will enable an unsurpassed simultaneous Q range, having good overlap with wide angle diffraction, suitable for a wide range of science.

Continuous Flow SAXS To Resolve Curved Guinier Plots Of Aggregating Or Self-Associating Proteins

Thomas C Irving, Ahmed Mirza, Elizabeth Mathew and Nick Menhart

Illinois Institute of Technology, 3101 S Dearborn, Chicago, Illinois 60616

We have combined Small Angle X-ray scattering and Gel Filtration Chromatography within a unified experimental set up to obtain molecular size information. Besides providing simultaneous corroborative data from two distinct experimental techniques bearing on the same question, passing the samples over a gel filtration column immediately prior to illumination by X-rays provides both a more homogeneous sample as well as providing a continuous set of data as the concentration is extrapolated to zero. This greatly facilitates analysis of data from even mildly aggregating proteins.

Laser Cleaning of Parchment: X-ray Diffraction Analysis

Craig J. Kennedy¹, Marie Vest², Martin Cooper³, Tim J. Wess¹

1. School of Optometry and Vision Sciences, Redwood Building, King Edward VII Avenue, Cardiff, UK, CF10 3NB

2. School of Conservation, Esplanaden 34, DK-1263, Copenhagen, Denmark

3. National Museums Liverpool, Laser Technology, Conservation Centre, Liverpool, UK, L1 6HZ

Laser cleaning of parchment is a novel technique that has the potential to provide contactless, chemical-free cleaning of historically important documents. However, the effect of laser cleaning on the collagenous structure of parchment is still poorly understood, as is the effect of the wavelength or the energy density (fluence level) used to clean parchment. In this study, small angle X-ray scattering (SAXS) of parchment samples after laser cleaning reveal the effect of cleaning to the structural characteristics of parchment. The effect of cleaning at infrared (1064nm), green (532nm) and ultraviolet (266nm) wavelengths at a range of fluence levels is investigated. Laser cleaning at IR or green wavelengths appears not to alter the collagen diffraction pattern from SAXS, but parchments cleaned at the ultraviolet wavelength display low-

coherence structural damage. SAXS is used to investigate the removal of dirt from parchment by laser cleaning, and shows that laser cleaning preferentially removes larger dirt particles.

Microfocus Small Angle X-Ray Scattering Study of Avian Eggshell Structure

Donna Lammie^{1,2}, Sally E Solomon¹, Maureen M Bain¹, Tim J Wess²

1. Poultry Research Unit, Department of Veterinary Preclinical Studies, University of Glasgow, Glasgow, Scotland

2. Structural Biophysics Group, Department of Optometry and Vision Sciences, Cardiff University, Cardiff, Wales

The eggshell is a highly ordered bioceramic composite, but currently little is known about the structure at the nanometer scale. Microfocus small angle X-ray scattering (mSAXS) allows us to probe the fine structural alterations, which may arise from subtle changes in the eggshell matrix. This paper describes the use of mSAXS to resolve different aspects of the shell growth process and to investigate textural changes at different layers within the eggshell. Microfocus analysis was carried out on beamline ID18F at the European Synchrotron Radiation Facility (ESRF) in Grenoble, France, using 300-micron thick sections of eggshell embedded within resin. A compound reflective lens was used to generate a microbeam of 1.5 microns by 15 microns. This powerful technology has not been used before to examine eggshell structure; therefore, our results are novel in the field of bioceramics.

Our previous results using X-ray diffraction and SAXS have given indications of the size and shape of the crystals. A comparison of these two methods have shown that variations exist in both sets of data, which could be attributed to the nanoinclusions and distortions in the eggshell that may be due to the organic matrix proteins. mSAXS has allowed us to produce two-dimensional maps that revealed the structural changes on a micron length scale due to the focussed beam size. Using the microfocus beam, eggshell sections were scanned over 500- by 300-micron size areas, and two-dimensional maps of crystallite characteristics were generated. The results clearly show changes in size and shape of mineral composition at different layers of the eggshell. This technique has allowed us to generate conclusions about the textural changes between different quality eggshells. Variables such as bird housing, nutrition and environmental stresses can alter the form and texture of the eggshell through alterations in crystal morphology. The eggshell matrix is thought to influence nucleation and control crystal growth and shape.

This investigation considers the influence of the eggshell matrix on calcite crystal formation, namely whether this will produce localised variations in coherence. Furthermore, organic/inorganic interfaces within the eggshell are studied; both of these characteristics are ideal for mSAXS examination. The two-dimensional maps provide evidence that microtextural changes, which are manifest at the macroscopic level, can influence the overall appearance of the eggshell. Our overall conclusions from examining the results produced by mSAXS suggest that there are subtle textural variations, which may be due to the presence of the organic matrix embedded within the calcium carbonate crystals.

Study of crystal reorganisation during unfolding transitions and molecular length dependance of the pressure-temperature phase diagram in ultra-long alkane crystals

T.D. Lord, S. Hanna, J.K. Hobbs, A.E. Terry

E.S.R.F. BP220, F-38043, Grenoble Cedex, France

Ultra-long, strictly monodisperse alkanes with chain length between 100 and 400 carbons, synthesised by Dr. G. Brooke et al [1], crystallize into extremely regular lamellae with a thickness that is an integer fraction of the extended chain length, and have been investigated as model systems for polymer crystallisation, crystal perfection and melting.

High resolution time resolved wide angle X-ray scattering on ID11, ESRF, Grenoble has been used to determine high precision changes in lattice parameters as crystal perfection, related to crystal thickness, occurs. It has also been identified that as the lamellae thickens due to the chains unfolding from one integer folded state to another, a contraction in the lattice occurs.

The impact of un-folding on lattice parameters was further studied using in situ temperature modulation pseudo differential scanning calorimetry experiments to complement TMDSC studies of the samples, to determine directly the reversible and irreversible parts of the transition between different crystal thicknesses.

The alkanes also provide an opportunity to carry out fundamental studies of the temperature-pressure phase diagram but on a truly pure system. The same approach of following contractions in the crystal lattice was used to obtain a high precision map of the effects of temperature and pressure on the lattice parameters of extended chain crystals, providing a link between the phase behaviour of high polymers, such as polyethylene and its oligomers,

and of small molecular systems, such as the n-paraffins.

High precision lattice parameters obtained were compared to those obtained at ambient pressure, to study the effect of constraining chain motion on crystal thickening.

References

- [1] G.M. Brooke, S. Burnett, S. Mohammed, D. Proctor, M.C. Whiting, J. Chem. Soc. %96Perkin Trans. 1 1996, 13, 1635.
- [2] A. Terry, J.K. Hobbs, T.L. Phillips, Macromolecules, 2003, 36, 3240.

Investigations of the crack tip deformation zone in Polyethylene pipe materials using Scanning Small Angle X-Ray Scattering (sSAXS)

Guenther Maier¹, Gerald Pinter² and Peter Fratzl^{1,3}

1. Materials Center Leoben & Erich Schmid Institute of Material Science, Jahnstrasse 12, 8700 Leoben, Austria

2. Institute of Materials Science and Testing of Plastics, University of Leoben, Franz-Josef-Str. 18, and Polymer Competence Center Leoben GmbH, Parkstr. 11, 8700 Leoben, Austria

3. Max-Planck-Institute of Colloids and Interfaces, Department of Biomaterials, 14424 Potsdam, Germany

Polyethylene (PE) is the mostly used synthetic polymer. By varying the molecular and morphological architecture and by adding filling particles, the mechanical properties of the material can be optimized for many applications. In pipe applications, PE has been successfully used for about 40 years. The mechanical properties of pipe materials and especially the long term behavior are important for manufacturers and users of pipes. For that, the change in morphology during deformation and fracture can give hints for the production of new materials and lead to a better understanding of the dominant failure mechanism in this class of materials. We used scanning small-angle x-ray scattering (scanning-SAXS) methods to study deformation near a crack tip during quasi brittle crack growth. SAXS is particularly useful to investigate the lamellar properties of polymers and, therefore, changes in the morphology occurring during a fracture test. In most polymers at high deformation levels, two processes occur at the same stage: deformation of the lamellar structure, often together with an induced orientation, and the formation of cavities. The measured SAXS pattern (IM) is a summation of the contribution from lamellae scatter (IL) and cavity scatter (IC). The contributions are often superimposed and must be separated for further investigations. With the assumptions that the size of cavities is large compared to the long period of the polymer and that the

scattering contribution from cavities decreases according to Porods law, IC can be described as IC_{bq}-4. We show that this assumption is compatible with the data obtained near the crack tip and use it to separate IC and IM. In this way, maps of the deformation in the region of the crack tip can be deduced from the scanning-SAXS analysis despite rather large volume fractions of deformation-induced cavities.

Skin to Historical Parchment: X-ray Scattering studies on collagen

C. Maxwell, C. Kennedy, J. Hiller, T. Wess

Cardiff University, Department of Optometry and Vision Sciences, Redwood buildings, King Edward VII Avenue, Cathays Park, Cardiff, Wales

Parchment contains important historical information, both within the text and in its structural composition. Made of animal skin, they are delicate materials that should be protected from environmental pressures such as UV irradiation, air pollution and bacterial degradation.

The main focus of this interdisciplinary project is to use the synergy between structural biophysics and proteomics to give an understanding of the effects on collagen during the process of parchment manufacture and its predisposition to degradative pathways.

The alignment and packing of collagen gives mechanical strength and its interactions with the macromolecules, hyaluronic acid, dermatan sulphide and lipids, contributes to a stabilising association.

The use of a synchrotron radiation source for small/wide angle x-ray scattering has given important information on the nanostructural texture of collagen. Our results show that the liming of wet skin causes a 1.9nm shortening of the axial packing repeat distance, and a 0.09nm widening of the intermolecular lateral packing in the fibrils. The drying of skin reduces the intermolecular lateral packing by 0.173nm, but drying limed skin has a reduction of 0.306nm. Biochemical techniques are being used to characterise lipid and proteoglycans affected due to the processing from skin to parchment to explain these effects on collagen.

Structure and Blood Flow in Normal and diseased Equine Metacarpophalangeal Joint

P.Muthuvelu, C.P.Winlove, D.A.Bradley

School of Physics, University of Exeter, Stocker Road, EX4 4QL, Exeter, UK

Osteoarthritis, the degeneration of the articular cartilage and the underlying bone of synovial joints is a very common disease, causing considerable distress and disability both in man. It is relatively uncommon in animals, but occurs frequently in horses, where it causes similar suffering.

Despite its wide-spread effects, and many years of research, the factors influencing the development and progression of arthritis are still poorly understood, and this is a barrier to the normal development of therapeutic strategies.

The present research was designed to investigate some of the fundamental processes that are thought to be involved in the development of arthritis. The disease clearly involves changes in the structure of both fibrous and inorganic phases of bone and cartilage. The structure and organisation of both components has been characterised largely by means of x-ray diffraction methods. The first aim of this work was to take advantage of recent methodological advances largely associated with the availability of intense synchrotron radiation, to investigate structure with unprecedented spatial resolution. We sought to characterise the structure of the interfacial region between bone and cartilage and the structural changes in the focal lesions of the equine metacarpo-phalangeal joint, which shares many of the structural features of human lesions.

The second theme of the research was to explore the role of disturbances in blood flow in the development of the disease. The normal function of the cells of cartilage is dependent on the ability of the microcirculation to maintain the supply of nutrients and to remove metabolites, and a number of theories link the failure of this system to the development of disease. Testing these hypotheses, however, presents a technical challenge, because many standard methods of measuring microcirculatory flow are unsuitable for use in bone. We therefore sought to refine a recently reported method using the detection of metal microspheres using X-ray fluorescence. We were particularly anxious to develop an x-ray based technique since this enables us, for the first time to locally relate blood flow to tissue structure.

Modelling Analysis of Myosin-based Meridional Reflections from Skeletal Muscles in Relaxed and Contracting States

**Kanji Oshima, Yasunori Takezawa,
Yasunobu Sugimoto, Thomas C. Irving*
and Katsuzo Wakabayashi**

Division of Biophysical Engineering, Graduate School of Engineering Science, Osaka University, Toyonaka, Osaka 560-8531, Japan and

*BioCat, Illinois Institute of Technology, Chicago, IL 60616, USA

Intensity analysis of the myosin-based meridional reflections in the X-ray diffraction patterns of live frog skeletal muscles was performed to propose a more detailed structural model for the myosin crown periodicity and the axial disposition of two-headed crossbridges along the thick filament in a sarcomere.

In the X-ray patterns with high angular resolution from relaxed and contracting muscles, myosin-based meridional reflections are sampled axially by the closely-spaced diffraction peaks arising from interference between the two symmetrical halves of thick filament centered on the M-line in a sarcomere as well as radially by the lateral filament array. The axial sampling period on the so-called forbidden reflections (M1, M2, M4....) corresponds to the separation between two regions with a 42.9-nm basic period in which the crown levels are systematically perturbed (the perturbed regions). Detailed analysis of the fine splitting periods of the second and fifth order meridional reflections showed that the average period was ca. 820 ± 40 nm in the relaxed state, while it was ca. 1010 ± 40 nm in the contracting state. This finding indicates that the perturbed regions of crossbridge crown levels occupy the central zone of crossbridge arrays in the relaxed state and shift towards the Z-band along the thick filament in the contracting state.

For modeling the crossbridges structure along the thick filament in the relaxed and contracting states, we used the observed intensities of the second to eleventh order meridional reflections. The intensities were corrected for the effect of lattice disordering. In the model, the crown regions with a regular repeat of 14.3 nm were assumed to be located on both sides of the perturbed region. The intensities of the meridional reflections from the assumed models were calculated by using eleven independent parameters; the shift of the crown level from the 14.3-nm repeat in the triplets, the width of projected density of each myosin head onto the thick filament axis and the distance between two myosin heads of a crossbridge and the number of the crossbridges in each region. The most probable values of these parameters were determined by searching the best fit of the calculated reflection intensi-

ties to those observed.

In the relaxed state, the perturbed regions are ca. 560-nm long with 13 triplet levels of the 42.9-nm repeat. The lengths of the inner (towards the M-line) and outer (towards the Z-band) regular regions on either side of the perturbed regions are ca. 57 nm and ca. 86 nm, respectively. In the contracting state, the perturbed regions become shorter than in the relaxed state and the lengths are ca. 480 nm with 11 triplet levels of the 43.5-nm repeat. The inner regular regions are ca. 160-nm long and the outer regular regions are ca. 73-nm long. The orientation of two-headed myosin crossbridges along the thick

Comparison of Breast Cancer Diagnosis Using Small angle X-ray Scattering from Synchrotron Radiation and a Conventional X-ray Source

Adam Round, Kieth Rogers, Chris Hall

Cranfield University, CCLRC Daresbury Laboratories

It has been indicated previously that breast tissue diagnosis could be performed using small angle X-ray scattering with synchrotron radiation. The use of conventional X-ray sources would allow widespread implementation of this technique as a laboratory based system. As a way to investigate this possibility both synchrotron radiation and a conventional X-ray source were used to collect data from core biopsy breast tissue. The biopsies were collected from tumor samples, as well as control tissue from cosmetic reduction procedures. As expected the laboratory based system produced lower angular resolution data sets and required longer exposure times than with synchrotron radiation. However consistent and reliable differences in amorphous scatter could be observed between normal and tumor samples using both systems. Thus indicating that it may be possible to develop a laboratory based diagnosis technique.

Shaft peptides from the beta-structured adenovirus fibre protein self-assemble into amyloid fibrils in the absence of a trimerization motif

Katerina Papanikolopoulou^(a), Guy Schoehn^(a,b,h), Vincent Forge^(c), V. Trevor Forsyth^(d,e), Christian Riekell^(f), Jean-Francois Hernandez^(a,g), Rob W. H. Ruigrok^(b,h) and Anna Mitraki^(a)

a. Institut de Biologie Structurale (UMR 5075, CEA-CNRS-UJF) 41 rue Jules Horowitz, 38027 Grenoble, France,

b. European Molecular Biology Laboratory, 6 rue Jules Horowitz, 38042 Grenoble, France

c. Laboratoire de Biophysique Moléculaire et Cellulaire; Unite Mixte de Recherche 5090; Département Réponse et Dynamique Cellulaires; CEA-Grenoble; 17, rue des Martyrs; 38054 Grenoble cedex 9; France

d. Institut Laue-Langevin, 6 rue Jules Horowitz, 38042 Grenoble, France

e. Lennard-Jones Laboratories, School of Chemistry and Physics, Keele University, Staffordshire ST5 5BG, United Kingdom

f. European Synchrotron Radiation Facility, 6 rue Jules Horowitz, 38042 Grenoble, France

g. Present address: Laboratoire des Amino Acides, Peptides et Proteines - CNRS UMR 5810, Faculté de Pharmacie, 15 avenue Charles Flahault, 34093 Montpellier, France

h. Laboratoire de Virologie Moléculaire et Structurale, EA 2939, Université Joseph Fourier, Grenoble 1, Grenoble, France

Viral fibrous proteins have recently been shown to contain novel beta-folding motifs composed of repetitive structural elements. We have been studying folding and assembly of such beta-structures using the fibre protein from adenovirus as a model system. Adenovirus fibres are trimeric proteins consisting of three parts: an N-terminal tail, a fibrous shaft in a triple beta-spiral conformation, and a C-terminal globular head domain. We have previously reported studies on a 41 amino acid peptide derived from the shaft sequences; this peptide failed to assemble into its native triple beta-spiral conformation and formed amyloid-type fibrils. In this work we have synthesized five shorter peptides (25, 12, 8, 6 and 4 amino acids) derived from the original 41 amino acid peptide and studied their potential for self-assembly using electron microscopy, Congo red binding, FTIR spectroscopy, and X-ray fibre diffraction. We find that formation of amyloid fibrils is a general propensity of shaft sequences when

isolated from their native context. The formation of amyloid by these sequences may occur as a result of out-of-register interactions in the absence of the globular head. In the context of the native fibre, the head domain may act as a natural registration signal that directs correct folding and assembly. We discuss the possible structure and arrangement of these sequences within the amyloid fibril, as compared to the one adopted within the native structure. These results are relevant to understanding amyloid formation by repetitive sequences from disease-associated proteins. The adenovirus shaft sequences can provide a model system to study folding, assembly and registration of beta-type structures both in native and in amyloid contexts.

Collagen interfibrillar spacing in the developing chick cornea and the link with keratan sulphate

Andrew J. Quantock, Melody Liles, Briedgeen Kerr, Clare Hughes, Bruce Caterson

Cardiff School of Optometry and Vision Sciences, and Cardiff School of Biosciences, Cardiff University and Cardiff Institute of Tissue Engineering and Repair

Proteoglycans in the avian corneal stroma are seen as potential modulators of corneal structure in the latter stages of development as the tissue becomes transparent. Previous chemical quantification of glycosaminoglycans from corneal isolates has indicated no change in the amount, molecular size, or degree of sulphation between developmental days 10 and 14 (Hart, *J Biol Chem* 1976;251:6513-21). After this time keratan sulphate becomes more highly sulphated, with the proteoglycan lumican likely bearing most of these chains (Cornuet, et al. *IOVS* 1994;35:870-7; Dunlevy, et al. *Exp Eye Res* 2000;70:349-62). The current study was designed to ascertain whether or not changes in the levels of sulphated KS in the corneal stroma correlate with alterations in collagen fibril spacing.

To do this we first carried out a SAXS analysis on Daresbury Station 2.1 of 78 isolated corneas from chicken embryos obtained daily from developmental day 12 to day 18 (n10 to 12 at each timepoint). This provided us with a measure of the average centre-to-centre collagen fibril Bragg spacing. Next, quantification by ELISA of papain digests of the same corneas was performed using the monoclonal antibody 5/D/4 that recognises highly sulphated epitopes on the KS chain.

Antigenic KS in the developing chick cornea (given as ug/mg wet weight of tissue (+/-SD)) measured 2.7+/-1.5 (day 12), 3.1+/-0.7 (day 13), 2.0+/-0.8 (day 14), 2.6+/-1.5 (day 15), 11.6+/-4.4 (day 16), 16.1+/-8.4 (day 17), and

24.1±7.9 (day 18). At the same time the fibril spacing in these same corneas dropped from 65nm to 53nm, and mainly this occurred after day 15. For the data set of 78 individual corneas interfibrillar Bragg spacing and antigenic KS levels showed an inverse correlation ($p < 0.001$; $R^2 = 0.501$).

As the chick cornea develops and becomes transparent in the week before hatching the compaction of stromal collagen fibrils is accompanied by an increase in tissue levels of sulphated KS.

Structural aspects of force generation by myosin heads probed by X-ray interference in single frog muscle fibres

M. Reconditi, M. Linari, E. Brunello, Y.-B. Sun*, T. Narayanan‡, P. Panine‡, G. Piazzesi, M. Irving* and V. Lombardi

Laboratorio di Fisiologia DBAG, University of Florence, I-50134 Firenze, Italy

and Istituto Nazionale di Fisica della Materia, OGG, Grenoble, France

*School of Biomedical Sciences, King's College London, SE1 1UL, UK

‡ESRF, BP 220, 38043 Grenoble, France

Force generation in muscle is thought to be due to transition between states with different degree of tilting of the light chain domain of the myosin head (Rayment et al., *Science* **261**, 58, 1993). We tested this idea by using X-ray diffraction interference to measure the changes in axial position of the heads associated to changes in isometric force with temperature, a factor that is known to change the force per myosin head (Piazzesi et al., *J. Physiol.*, **549**, 93, 2003 and references therein). During the isometric contraction of single muscle fibres of *Rana temporaria*, X-ray interference between the two arrays of myosin heads in each myosin filament splits the M3 reflection from the 14.5 nm axial repeat of the heads into two main peaks (Linari et al., *PNAS* **97**, 7226, 2000). In the experiments reported here patterns were collected at ID2 (ESRF) on the image intensified FReLoN CCD detector placed at either 10 m (to collect intensity and fine structure of the low order meridional reflections) or 3 m (to collect intensity of the higher order meridional reflections and of the actin layer lines). Increasing the temperature from 0°C to 17°C increased the isometric tetanic force (T_0) by ~40% ($43 \pm 2\%$), decreased the relative intensity between the high angle peak and the low angle peak (R) of the M3 reflection from 0.93 ± 0.02 (mean \pm SE, 5 fibres) to 0.77 ± 0.02 and increased the spacing of

the M3 and M6 reflections linearly with the isometric force by the same amount as that estimated with step length changes ($0.26\%/T_0$, Reconditi et al., *Nature* **428**, 578, 2004). The intensity of the 1st actin layer line, measured in the same range of temperatures, increased by $57 \pm 18\%$ (5 fibres). The extension of the actin filament measured by the spacing changes of the 5.1/5.9 nm actin-based layer lines increases linearly with the force, with a slope 2.5 times that obtained from length step experiments ($0.74 \pm 18\%/T_0$ instead of $0.2-0.3\%/T_0$, Huxley et al., *Biophys. J.* **67**, 2411, 1994; Wakabayashi et al. *Biophys. J.* **67**, 2422, 1994) indicating that the actin filament is viscoelastic. Changes in the fine structure of M3 reflection that accompany temperature dependent changes in the isometric force show that a step forward in the working stroke can be entropically driven. A simulation of the changes in R, with the tilting lever arm model of the myosin head and a mechano-structural model of the sarcomere, indicates that the axial movement of the heads accounts for the increased instantaneous stress-strain relation of the myofilaments.

Supported by MIUR (Italy), MRC (UK), ESRF, EMBL

pH Responsive Polymer Systems for use in Molecular Motors, Pumps and Valves

Paul Topham

University Of Sheffield

The ability of individual polymer molecules to respond to changes in temperature and chemical environment with drastic changes in size and conformation has been appreciated for many years. The volume transition of responsive gels represents a direct, macroscopic manifestation of the conformational response of the individual molecules making up the gel. Responsive gels have been enthusiastically greeted as candidates for a new generation of intelligent materials with sensor, processor and actuator functions.

In our program, we concentrate on weak polyacids and polybases, which respond to changes in pH. At the macroscopic level, these systems, when coupled with a chemical reaction that cause spontaneous pH oscillations, allow us to make a free-running chemical motor. We explicitly link the macroscopic behaviour to the microscale behaviour by studying the response of triblock copolymers to pH oscillations. The active chains are the mid-blocks and are effectively crosslinked by the domains of the hydrophobic end block. The expansion and contraction of the grafted polyelectrolyte chains causes the distance between hydrophobic domains to change, this separation can be monitored by SAXS and the molecular and macroscopic effects correlated.

SAXS study of lobster aortal microfibrils

Veronique Siegler and Tim J. Wess

Cardiff University, School of Optometry and Vision Sciences, Redwood Building, King Edward VII Avenue, CF10 3NB Cardiff, U.K.

We have obtained for the first time X-ray diffraction images of lobster aortal microfibrils. Lobsters have highly developed circulatory systems, but little is known about the exact tissue structure and biomechanical properties of their aorta. Microfibrils are essential components of the extracellular matrix, and are thought to impart force-bearing and elastic biomechanical properties to dynamic connective tissues. The ultrastructure of microfibrils is rather complex, due to their non-crystalline, variable, heterogeneous nature. Multidisciplinary studies of mammalian tissues have revealed that microfibrils form linear structures with a characteristic beaded appearance of an average periodicity of 56nm in the relaxed state. Our preliminary SAXS investigations under stretching conditions gave us some ultrastructural information that can be compared with that of mammalian microfibrils. The tentative fundamental axial periodicities we have obtained in relaxed and tensed states are smaller than those for mammalian. The understanding of the organisation of microfibrils across various species is a fundamental step towards biomimetics. Interestingly, previous workers (Shadwick, 1992) have shown that elastin, which is a major component of mammalian tissue, is not found in lobster aorta. However, lobster microfibrils do exhibit a modulus of elasticity similar to that of elastin, implying a unique elastic role for the lobster aortal microfibrils. Our SAXS study addresses important questions about elasticity mechanisms, for example whether or not extension of the aortal tissue is due to the deformation of microfibrils themselves.

Reference

Shadwick, R E (1992). Circulatory structure and mechanisms. In *Biomechanics, Structures and Systems: A Practical Approach* (ed. A.A. Biewener), pp. 233-261. New York: IRL Press.

I22 - an NCD beamline for Diamond

N.J. Terrill, A. Grant*, A. Marshall, A. Smith*, K. Sawhney

Diamond Light Source, Daresbury Laboratory*

The requirements to meet the scientific and technological challenges of the next decade are for a high resolution, high brightness beamline. These can only be provided by an undulator insertion device on a 3rd generation synchrotron radiation light source. I22, served by a U25 in vacu-

um undulator will deliver high photon flux (1×10^{14} ph/s/0.1%b.w.) into a focused 300 x 75 m spot (1 x 1 m with microfocussing) in the energy range 4-20keV. The End Station with associated linear and area detectors for static and time resolved measurements will be capable of recording the scattered radiation from samples contained in purpose designed specialised environmental cells. The end station's modular arrangement will allow a choice between small angle scattering for large fibrous structures or microfocus illumination each with a wide angle scattering option for materials studies. The latest developments in design for the beamline will be described.

Medical Application of Diffraction Imaging

Steven J. Wilkinson, Keith D. Rogers, Chris J. Hall

Cranfield University, Daresbury Research Laboratory

Life sciences exploitation of X-rays has followed two distinct disciplines to date, medical imaging and X-ray diffraction. Each field has developed independently of one other. Analysis of X-ray diffraction data enables effects of structures at molecular and supramolecular scales to be determined. Until now the more conventional X-ray absorption has relied upon the removal of scattering effects that occur whenever X-rays traverse matter in order to produce high quality images be it conventional absorption or sophisticated 3-dimensional imaging such as computer assisted tomography.

Diagnostic methods rely on the detection of abnormalities either by appearance or chemical/histopathological differences that can be recognised by a clinician. Diagnoses can be highly subjective and any new method that adds to diagnostic armoury, preferably one that has a more direct way of measuring biochemical and structural changes, would be valuable. X-ray diffraction will gather information regarding the molecular structure of the tissue. The big advantage of using X-ray diffraction is that tissue specific components (e.g. collagen, lipids etc.) can be isolated and used to form images.

An initial application of this technique that is being explored is that of breast cancer diagnosis. Breast cancer has been chosen as an initial application as it is a particularly accessible connective tissue. Scattered X-rays are discarded as a matter of course as they would degrade standard mammography scans which accounts for 60% of the incident X-rays. These scattered X-rays contain a wealth of information about the molecular structure which may well provide earlier diagnosis. There is evidence that cancers affect the molecular structure of the connective tissue there is an opportunity for early identification of cancers using a non-invasive method. Rather than simply a number from a site biopsy, this method will

provide a visual method of identification which will work well with current problematic cases from young women where breast density (i.e. greater collagen content).

The current stage of research has software in place ready to create images from series of wide beam diffraction patterns from phantoms and test tissues. Here methods of image construction are discussed which provide a relatively automated way of producing diffraction images.

In conjunction with histological methods and analysis of narrow beam diffraction patterns, core cut samples will be characterised to determine whether clinically useful information can be derived. Once 2D has been fully explored then 3D molecular imaging will also be used.

X-ray diffraction experiments on heart

N. Yagi

SPring-8/JASRI

Heart is a physiologically and medically important organ. However, there have been only a very limited number of x-ray diffraction studies on cardiac muscles, especially on intact ones. At SPring-8, small-angle diffraction experiments are carried out on both isolated papillary muscle and whole heart. In both cases, the specimen is kept under a physiological condition and beating continuously. Although the amount of information available from the diffraction pattern, which is dominated by equatorial reflections, is not abundant, the feasibility to study molecular aspects of cardiac function under different physiological and pathological conditions makes these experiments attractive to the medical society.

Use of size exclusion chromatography for Improved SAXS measurements

Nick Menhart, Ahmed Mirza, Elizabeth Matthew and Tom Irving

Dept. BCPS, Illinois Institute of Technology, Chicago IL 60616 USA

We have combined small angle X-ray scattering and size exclusion chromatography within a unified experimental set up to obtain molecular size information. Besides providing simultaneous corroborative data bearing on the same question from two distinct experimental techniques, passing the samples over a gel filtration column immediately prior to illumination by X-rays provides both a more homogeneous sample and a continuous set of data as the concentration is extrapolated to zero. This greatly facilitates analysis of data from oligomerizing or aggregating proteins and increases the reliability of the results.

In-situ WAXS studies of structural changes in wood foils and in individual cells during microtensile tests

**J. Keckes¹, I. Burgert^{1,2,3}, M. Müller⁴,
K. Kölln⁴, S. E. Stanzl-Tschegg³,
P. Fratzl²**

1. Erich Schmid Institute for Materials Science, Austrian Academy of Sciences and Institute of Metal Physics, University of Leoben, Austria
2. Max-Planck-Institute of Colloids and Interfaces, Department of Biomaterials, Potsdam, Germany
3. Institute of Meteorology and Physics, University of Agricultural Sciences, Vienna, Austria
4. Institute for Experimental and Applied Physics, University Kiel, Germany

The mechanical behaviour of wood is closely related to the cell wall architecture and to the magnitude of microfibril angle (MFA). Though there have been a significant effort to characterize both the structural properties of wood cell wall and the mechanical performance of the tissue, systematic in-situ investigations of wood microstructure under external forces are rare. In this contribution, structural changes in wood foils and in individual wood cells upon mechanical loading are studied.

Three different compression wood types were chosen, namely *Ginkgo biloba* L., *Juniperus virginiana* L. and *Picea abies* [L.] Karst, for wide-angle x-ray scattering (WAXS) combined with tensile tests. The experimental setup allowed to monitor simultaneously the structural development in foils (or in individual cells in the case of single cell experiments) using a 2D CCD detector and relate this information to the actual magnitude of stress and strain.

The results indicate that the MFA magnitude decisively influences the mechanical performance of the tissue. The stress-strain dependence in foils from various tissues as well as the MFA dependence on the strain can be in some respect derived from the initial MFA magnitude at the beginning of the tensile experiment. Generally, the magnitude of MFA decreases linear with the increasing strain though, in individual cells, the decrease is inhomogeneous. The WAXS and mechanical data moreover indicate that the hierarchical architecture with specific MFA predefine also the maximal stress and strain magnitudes applicable. A qualitatively novel information was obtained from tensile experiments with interrupted straining or with loading and unloading cycles. The results indicate a stiffness recovery phenomena beyond the yield point even for strain values very close to fracture. This behavior was interpreted by a molecular stick-slip mechanism in the cell wall between the cellulose microfibrils

which allow a reorganization of the amorphous cell wall constituents during the tensile experiment [1].

Reference

- [1] J. Keckes, I. Burgert, K. Frühmann, M. Müller, K. Kölln, M. Hamilton, M. Burghammer, S.V. Roth, S. Stanzl-Tschegg & P. Fratzl (2003). Cell-wall recovery after irreversible deformation of wood, *Nature Materials* **2**, 811-814.

Age-related changes in collagen fibril diameters in the mouse tail tendon

KL Goh¹, JL Haston², J Hiller¹, DF Holmes³, KE Kadler³, TJ Wess¹

1. Cardiff Institute of Tissue Engineering & Repair, School of Optometry & Vision Sciences, Redwood Building, Cardiff University, Cardiff, CF10 3NB, UK
2. School of Biological & Environmental Sciences, Stirling University, Stirling, FK9 4LA, UK
3. School of Biological Science, University of Manchester, Michael Smith Building, Oxford Road, Manchester, M13 9PT, UK

The extra-cellular matrix (ECM) in tendons contains collagen-rich fibrils which provide reinforcement for the tissue. Changes in the size and composition of these fibrils, e.g. during the process of ageing, will affect the overall mechanical properties of the tissue. We have characterized collagen fibril diameters in tail tendons from young to old mice to complement an on-going ageing study on the composition of the ECM. Collagen fibril diameters and the frequency distributions of these diameters were determined for tail tendons from young to old mice using transmission electron microscopy (TEM). We have also derived the fibril packing fraction from TEM images. For each age group small angle x-ray scattering (SAXS) pattern of a tendon from the same tail was acquired; the intensity along the equatorial region of the SAXS pattern was compared with calculated values obtained from a mathematical model of the form factor using fibril diameter data from TEM. This approach provides a way for assessing how representative is the population of fibrils selected for diameter analysis. Additionally, the goodness-of-fit between the two sets of results also provide a check for the packing density derived from TEM. Our findings show that fibril diameters are distributed over a range of values. The spread of values is skewed in young mice and broadens, with increasingly larger diameters observed, as mice mature. Consequently, the mean fibril diameter in the tail tendons increases from 6 week to 4 months. From 4 to 30 months, no appreciable increase was observed. The packing fraction of fibrils in the tendon also exhibits similar trend with age. The information derived from this study, in combination with those from a

separate study on ECM composition, may then help provide insights into the mechanisms governing the changes in the mechanical properties of the tendon.

PROP - Bridging the Gorge between Unix and Windows

James C. L. Burnley and Ron Ghosh

Institut Laue Langevin, BP 156 centre de tri, 38042
GRENOBLE cedex 9, France

The calculations performed in programs originating on Unix are usually easy to port to PC-Windows. The Windows user however is little used to the command line style of Unix, and is faced with constructing batch files to present a correct environment for the ported program. He then has to face the problem of printing the results on a Windows printer as well as dealing with PostScript graphics files.

PROP is a graphical program written in Tcl/Tk which aims to reduce this trauma by providing an environment (often set up in the Unix login scripts) for installing, running programs, and viewing and printing results. To simplify installation it has been packaged together with the Tk interpreter, and also basic graphical libraries and tools for Tim Pearson's PGplot graphics for both MinGW and Visual Studio compilers. These latter include a Windows graphics server from Tsuguhiko Tamaribuchi which again resolves many problems of printing on Windows. The source code of programs using PGplot libraries remains identical on Unix and Windows.

PROP has a program directory defined; programs therein appear in a list box, and can be started by selection. Console programs are given a temporary console window; GUI applications are launched separately. Results are accumulated in PROP's working directory, and again these can be listed, and selection allows results to be viewed in an editor and printed. A re-usable PGplot graphics window is used for all graphics, and there are options to print from this.

A practical example of use is in federating together the set of SANS data treatment programs at the ILL. The MinGW compiled programs for Windows now share code with Unix, Linux and Macintosh OS-X programs.

More information on the program and graphical tools may be found at http://www.ill.fr/data_treat.

***Fibre Diffraction Review*: Instructions to Authors**

Submitted original papers, technical reports, Reviews, comments/letters and meeting reports for inclusion in *Fibre Diffraction Review* are welcome.

Technical Reports

These include presentations of the latest developments in CCP13 and other fibre diffraction/ non-crystalline diffraction software and their scientific justification and also, for example, reports on developments at synchrotron beamlines used for fibre diffraction and non-crystalline diffraction studies.

Reviews

These include summary presentations of the 'state of the art' in the structural analysis of particular fibrous or non-crystalline systems.

Original Papers

These present previously unpublished results from fibre diffraction or small-angle scattering experiments using either X-ray, neutron or electron diffraction.

Expanded Poster-Prize Abstracts

At each of the CCP13/ NCD Annual Workshops cash prizes are presented to the best poster presentations. The judges are always senior scientists in the field and are often from overseas. Winners of the Poster Prizes are invited to expand their abstracts into short papers for inclusion in *Fibre Diffraction Review*.

Refereeing

All papers, of whatever category above, will be refereed by at least two people (from the CCP13 Committee or their nominated referees) and may be either (a) accepted as they stand, (b) returned for rapid revision, or (c) rejected. As well as their scientific content, papers will be judged on their clarity of presentation and the quality of their figures.

Meeting Reports

Fibre Diffraction Review includes reports on relevant meetings and conferences which include an element of fibre diffraction or small-angle scattering and which will be of general interest to our readers. Such reports will often be solicited by the Editor from known meeting participants. Other potential contributors to this part of the Journal should contact the Editor prior to writing their report.

Comments/Letters

Feedback from readers about CCP13, about the NCD community and about the Journal itself are welcome. These could be in the form of comments or letters to the

Editor. Suitable contributions will be published in the Journal.

Advertisements

Industrial/commercial adverts of interest to our readers are welcome. Potential advertisers should contact the Editor for details of current rates.

Submission

Contributions should be sent to the Editor before the annual deadline (December 31st) for each issue. Contributions submitted after this date may be held over for the following issue.

Colour illustrations are welcome and are included without charge. Contributions should be submitted in electronic format to the Editor (j.squire@imperial.ac.uk).

Text should be in Word 6 format and illustrations should be submitted as separate files at high resolution in TIFF or JPG format.

References should be in the format specified for *J. Molecular Biology*, and should be complete with title. Please find more details from our website.

Reprints

It is not economic for us to produce reprints of articles. However, in future, papers will be made available on the CCP13 website in downloadable pdf format.

Those wishing to purchase extra copies of the whole Journal should contact the Editor to find out costs.

Editor's Address

Professor John M. Squire,
Head, Biological Structure and Function Section,
Biomedical Sciences Division,
Imperial College of Science, Technology & Medicine,
London SW7 2AZ, UK.

Editor '*Fibre Diffraction Review*' (ISSN 1463-8401).

Useful World Wide Web addresses (URL)

Fibre Diffraction Review
CCP13

<http://www.fibrediffractionreview.org>

<http://www.ccp13.ac.uk>

<http://www.ccp13.org>

<http://www.bio.aps.anl.gov/biocat/mirror/www.ccp13.ac.uk/>

<http://www.ill.fr/ccp13>

NCD

<http://www.srs.dl.ac.uk/NCD>

SRS

<http://www.srs.ac.uk/SRS>

FiberNet

<http://fibernet.us/>